Nanodomain Structure of Native Cellilose Microfibril(Dissertation_全文)

AUTHOR(S):

Imai, Tomoya

Nanodomain Structure of Native Cellulose Microfibril

Tomoya Imai

2000

Nanodomain Structure of Native Cellulose Microfibril

Tomoya Imai

2000

Contents

General Introduction - - -

General Introduction

Overview of the native cellulose structure

Cellulose, one of the native polysaccharides, is a major component of wood (plant) cell walls and functions as a frame. It also plays an important role in ecosystem as a major carbon sink of CO_2 and carbon source for primary producers like bacteria and fungi. Cellulosic materials of biological origins – textile, paper, *etc.* – have long been utilized, thanks to their superior properties: higher elastic modulus, hydrophilicity, electric insulation, *etc.* These properties are related to the structure, which should be characterized during the biosynthesis and affect the manner of biodegradation.

Cellulose has a simple molecular architecture of β-(1,4)-linked D-glucose. Various organisms including plants – algae, bacteria, tunicates and so on – produce cellulose as an extra-cellular matrix in the form of a long thread, termed a 'microfibril', in which molecular chains with a straight conformation are crystallized by a complex network of intra- and inter-molecular interactions of hydrogen bonding together with van der Waals forces. Thus, the isolated microfibril is sometimes called a "microcrystal". It is considered that the perfection of the crystal varies from region to region in a microfibril: it contains a substantial amount of amorphous region. The microfibril exhibits biological diversity depending on the origin: for example, the microfibril size, crystallinity, degree of polymerization, and crystal structure (as shown later). The diversity in the crystal structure, in particular, together with the small size of microfibrils (30nm at most), principally had kept the researchers away from the real structure until these days.

Historical Background of the Cellulose Structure

Cellulose crystal comprises four polymorphs, and the native cellulose, which is in the form of microfibril, generally adopts one of them, cellulose I. To clarify the crystal structure by diffraction, fiber patterns are usually analyzed because cellulose I exists in the form of a tiny microfibril and it is difficult to prepare a large single crystal even now. Historically, the most important model is that proposed by Meyer & Misch in 1937 from the study of ramie cellulose: a two-chain $P2_1$ monoclinic unit cell of a=0.79nm, b=0.83nm, c=1.03nm (fiber axis) and γ=96° [*], where the two molecules were located on the two-fold screw axis in the $P2_1$ unit cell. This indicates that the crystallographic repeating unit of cellulose I crystal is a cellobiose that possesses 2-fold helical symmetry about the molecular axis. As to the chain polarity in this model, the two molecules are packed in the unit cell in the opposite direction to each other, or in

---

[*] In their original report [Meyer & Misch 1937], the axes were defined differently. Based on a right-handed system, here, the origin of the unit cell is positioned at the left-up corner in the *ab* plane with an obtuse monoclinic angle γ, and the *c*-axis is the fiber axis.

"antiparallel". (The opposite to this is "parallel", where the molecules are in the same direction.) This Meyer-Misch model was quite close to the real structure except for the chain polarity.

A second landmark was achieved by Honjo & Watanabe in 1958, who showed "super-lattice reflections" in an electron diffraction fiber diagram of the cellulose from a green marine alga *Valonia* which was chosen as a specimen because its high crystallinity provided a lot of sharp diffraction spots. Since the Meyer-Misch model could not explain these reflections, they newly proposed the eight-chain monoclinic unit cell where both sides of the *ab* plane were twice those in the Meyer-Misch model. This experimental fact pointed out a very important aspect of the native cellulose structure, although it is known now that the eight-chain unit cell proposed here was a wrong interpretation of the super-lattice reflections. Subsequent studies also focused on the super-lattice reflections in a fiber pattern of algal cellulose, but none was able to provide the absolute structure consistent with the diffraction data, and various possibilities were considered (summarized in Table I). On the other hand, the cellulose from ramie did not gave super-lattice reflections in the X-ray fiber diagram [French 1978, Woodcock & Sarko 1980], which allowed for all reflections to be indexed based on the two-chain $P2_1$ monoclinic unit cell and revealed that ramie cellulose has a different structure from algal cellulose. This point also implied an important characteristic of native cellulose structure. With respect to the chain polarity, however, two experiments elegantly evidenced a parallel structure for cellulose I: unidirectional degradation of cellulose I microcrystal (microfibril) by a cellulase, cellobiohydrolase II (CBH II) [Chanzy & Henrissat 1985] and silver labeling at only one end (reducing end) of a microfibril [Hieta *et al.* 1984, Kuga & Brown 1988].

Table I. The structural models for cellulose I that have been proposed

Authors	Year	Chain polarity [1)]	Unit cell	Number of chains	Method [2)]	Sample
Meyer & Misch	1938	AP	$P2_1$ monoclinic	2	X-ray	ramie
Honjo & Watanabe	1958	-	$P1$ monoclinic	8	ED	*Valonia*
Fisher & Mann	1960	-	$P1$ monoclinic	8	ED	*Valonia*, BC
Ellis & Warwicker	1962	P	$P1$ monoclinic	4	ED	*Valonia*
Gardner & Blackwell	1974	P_d	$P2_1$ monoclinic	2	X-ray	*Valonia*
Sarko & Muggli	1974	P_u	$P1$ triclinic	2	PE, X-ray	*Valonia*
French	1978	AP	$P2_1$ monoclinic	2	X-ray	ramie
Woodcock & Sarko	1980	P_u	$P2_1$ monoclinic	2	X-ray	ramie
Sugiyama *et al.*	1991b	P_u	$P1$ triclinic & $P2_1$ monoclinic	1 & 2	ED	*Microdictyon*

1) AP: antiparallel, P: parallel, $_d$: down chain, $_u$: up chain, -: not determined. (The definition of up and down chains is described in the text.)

2) ED: electron diffraction, PE: packing energy calculation, X-ray: X-ray diffraction

The technique that achieved a breakthrough was solid-state CP/MAS ^{13}C-NMR (Cross Polarization/Magic Angle Spinning ^{13}C-Nuclear Magnetic Resonance) spectroscopy. The multiplicity in narrow signals from each carbon in native cellulose or cellulose I was interpreted as a composite of two distinct crystals of I_α and I_β, whose fractions were different depending on the biological source [Atalla & VanderHart 1984, VanderHart & Atalla 1984]; for example, algal or bacterial cellulose is I_α-rich while cotton or regenerated cellulose is dominated by I_β phase. Pure I_β cellulose has been reported in tunicates [Belton *et al.* 1989, Larsson *et al.* 1995], while pure I_α cellulose has yet to be found in any specimens. A further study with ^{13}C-NMR demonstrated that the I_α phase can be converted to I_β irreversively by hydrothermal treatment [Horii *et al.* 1987], which implies that cellulose I_α is in an energetically metastable state compared with cellulose I_β. This conversion treatment, so called "annealing", is possible also in diluted alkaline solution [Yamamoto *et al.* 1989], organic solvents like glycerol, and helium gas [Debzi *et al.* 1991] at high temperature (260-280°C). It occurs in a solid state without changing the crystallinity and the appearance of microfibril [Sugiyama *et al.* 1990]. How the conversion takes place is not well understood, however.

The IR (Infra-Red) spectra also allow for distinguishing I_α- from I_β-rich cellulose specimens [Sugiyama *et al.* 1991a]. An early study by IR spectroscopy pointed out that there are two types of spectra in cellulose I, depending on the specimens [Marrinan & Mann 1956, Mann & Marrinan 1956]: type A is from bacteria and algae, and type B is from plants and regenerated cellulose I. They could not attribute these spectral differences to structural aspects at the time, but now it is clear that type A and B spectra were from I_α- and I_β-rich cellulose, respectively.

As shown above, spectroscopic studies have provided insight into the two-phase system in cellulose I crystal. Then what are these phases in crystallography? Sugiyama *et al.* [1990] showed that the super-lattice reflections in an electron diffraction diagram from *Valonia* cellulose disappeared following annealing treatment, *i.e.* cellulose I_β has a two-chain $P2_1$ monoclinic unit cell and it was suggested that cellulose I_α has triclinicity. Further investigation by *electron microdiffraction*, which allowed for pure I_α diffraction patterns to be obtained from a 20-100nm region, concluded that cellulose I_α and I_β are a one-chain $P1$ triclinic unit cell (a=0.674nm, b=0.593nm, c=1.036nm, α=117°, β=113°, γ=81°) and a two-chain monoclinic unit cell (a=0.801nm, b=0.817nm, c=1.036nm, γ=97.3°), respectively [Sugiyama *et al.* 1991b]. Therefore, the diffraction fiber diagram from algal cellulose is a superposition of the triclinic and the monoclinic fiber pattern: the super-lattice reflections observed in the fiber diagram were due to the one-chain triclinic unit cell. The most apparent difference in structure between these two phases is the shift of the cellobiose unit along the c-axis: there is zigzag staggering with an interval of $c/4$ in the monoclinic unit cell and unidirectional stepping of the unit by $c/4$ in the triclinic unit cell, when the cellulose crystal is viewed along the hydrogen-bonding sheet (*i.e.*, $(110)_t$ ** lattice in the triclinic and $(200)_m$ in the monoclinic). On the other hand, the equatorial arrangements of the molecules are basically the same in the triclinic and monoclinic structure: they share a nearly identical equatorial lattice. These aspects are illustrated in Figure I.

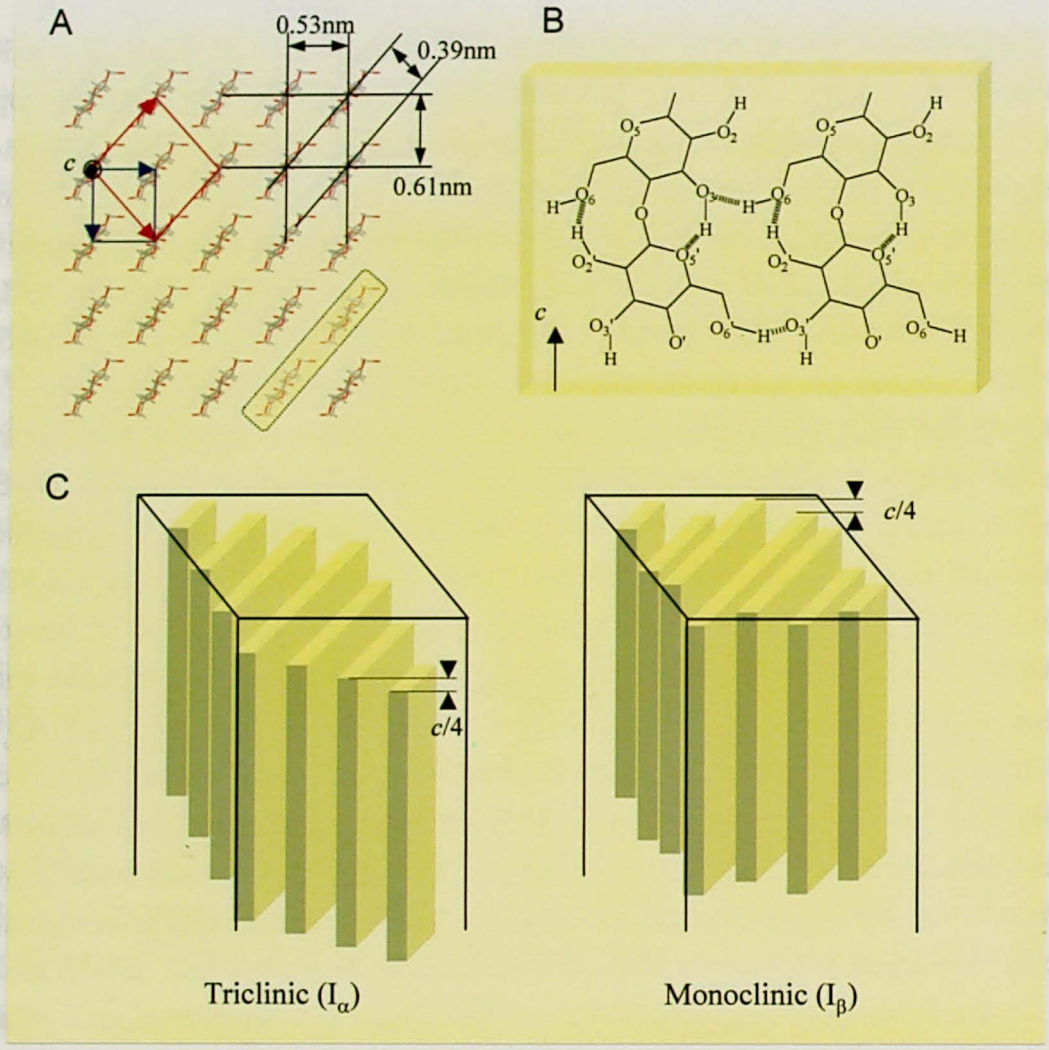

Figure I. Current structural model for native cellulose crystal. **A**: Equatorial view of cellulose I crystal. The I_α (blue) and I_β (red) crystals share a nearly identical molecular arrangement in equator: three major lattice planes are seen in both structures, whose d-spacings are about 0.61, 0.53 and 0.39nm [¶]. The shaded box indicates a sheet formed by H-bonding. **B**: H-bondings in the sheet indicated in A [Gardner & Blackwell 1974, Sarko & Muggli 1974]. All the molecules are at the same level within the sheet. There are two intermolecular and one intermolecular H-bondings. **C**: Schematic diagrams describing the differences in the translation along the chain between I_α and I_β. In I_α, the translation of the H-bonding sheet is unidirectional, whereas it is alternate in I_β.

[**] Throughout this thesis, the indexing of crystallographic lattice planes in cellulose I refers to the unit cell proposed by Sugiyama *et al.* [1991b]. The monoclinic indexing is represented by $(hkl)_m$, whereas the triclinic indexing is shown by $(hkl)_t$.

[¶] For convenience, these planes are sometimes called 0.61-nm lattice, 0.53-nm lattice and 0.39-nm lattice planes: they are indexed $(1\bar{1}0)_m$, $(110)_m$ and $(200)_m$ by the monoclinic, and $(100)_t$, $(010)_t$ and $(110)_t$ by the triclinic system.

As shown above, the heterogeneity and structural diversity of the crystal structure in native cellulose have been recognized, which had not been considered in earlier studies. Thus, studies based on these aspects are necessary for clarifying the general microfibril structure of native cellulose.

Two possible parallel structures in cellulose I and β-chitin

Chitin is a very similar polysaccharide to cellulose in terms of structure; both have a linear molecular framework of β-1,4-linkaged pyranose rings (*i.e.*, 2-*N*-acetyl-D-glucosamine in the former case and D-glucose in the latter) and are crystallized into several polymorphs. One of the polymorphs in the chitin crystal, β-chitin, occurs in the form of crystalline microfibril as well as cellulose I, and adopts a one-chain $P2_1$ monoclinic unit cell with the molecule exactly located on the two-fold screw axis (a=0.485nm, b=0.926nm, c=1.038nm (fiber axis) and γ=97.5°) [Gardner & Blackwell 1975]. This implies that chitobiose possessing two-fold helical symmetry about the molecular axis is the repeating unit and all the chains automatically adopt the same sense in the β-chitin microfibril; the "automatically" means that the whole crystal (microfibril) constructed by piling the one-chain unit cell inevitably provides a parallel structure.

In cellulose I (both I_α and I_β) and β-chitin, the molecules are positioned on the parallelogram-shaped lattice in equator (a primitive oblique), so there are two ways in which the polar molecule(s) locate in parallel, depending on the directionality of the molecules along the crystallographic c-axis (Figure II). Gardner & Blackwell defined the "up" chain whose z-coordinate of O_5 in a glucose moiety is bigger than that of C_5, in their studies on structure refinement of cellulose I and β-chitin [1974 & 1975, respectively]. In other words, the chain whose reducing end points in the same direction as the c-axis was referred to as "up" and the reverse was "down". They concluded that parallel-down situations were more appropriate in both cellulose I and β-chitin by crystallographic analysis.

Once the chain directionality in the unit cell is given, it becomes possible to determine which side is the reducing end in a microfibril including parallel chains. Recently in fact, it was experimentally demonstrated that cellulose I has a parallel-up structure, by obtaining successive electron microdiffraction diagrams in a set of projections from a single microcrystal whose reducing end is specifically tagged by silver labels [Koyama *et al.* 1997b]. This evidenced that cellulose is polymerized at the non-reducing end of the growing chain in a gram-negative bacterium, *Acetobacter aceti*. In principle, the same technique also will be available soon for β-chitin microcrystal if a selective labeling technique in β-chitin is established.

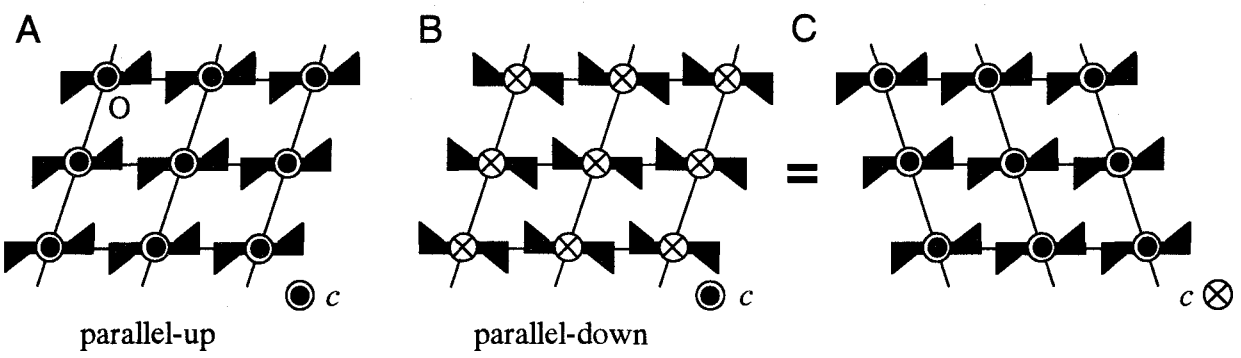

Figure II. Cartoons representing the two parallel structures in the case of cellulose I and β-chitin; the type of equatorial lattice illustrated here is a primitive oblique, which describes structures of cellulose I and β-chitin not precisely but essentially. The *c*-axis (fiber axis) goes upward in A and B. Polar chains are packed in parallel in two ways: all the chains go in the same direction as the *c*-axis (parallel-up, A) and the reverse (parallel-down, B). The difference between these structures is apparent also in the comparison of A and C. The parallel-down structure is equivalent to the mirrored lattice packed with up-chains (C), where the *c*-axis goes downward. If there is no polarity in the chain, the distinction between these two structures vanishes.

Purpose of this thesis

Based on the structural diversity, the small size and complex structure of the single microfibril, the author has attempted to clarify the microfibril structure of cellulose by several specific methods.

Electron microdiffraction and image decomposition of High Resolution Electron microscopy (HREM) images are direct and powerful tools with which the nano-structure in a 'micro' fibril are assessed, providing information about the molecular arrangement in a tiny fiber. As an indirect approach, the author examined the cellulase degradation pattern using insoluble solid microfibrils; cellulases possibly detect some differences in microfibril structure during the degradation and the resultant microfibrils should provide information about structure along with cellulase interaction. Thus the author tried to employ a cellulase as a "sensor" for the nano-structure of cellulose substrate. In view of the structural diversity, the author investigated cellulose from a gray alga, *Glaucocystis*, which showed unique features never reported so far. Finally, the author tried to establish a new method for the specific labeling of the molecule's end in a polysaccharide microfibril. Molecular directionality in a microfibril is one of the significant aspects when considering the formation and degradation of microfibril structure. β-Chitin is the target in this experiment.

In summary, this thesis aims at the organized understanding of native cellulose structure, along with biosynthesis and biodegradation. In addition, a new technique to label the end of β-chitin microcrystal is searched, which will provide general insight into the microfibril structure of polysaccharides, including cellulose.

1. Localization of I_α Domain in *Cladophora* Cellulose (I)

-Electron Microdiffraction Study-

1.1 Introduction

As reviewed in General Introduction, native cellulose is a composite of the two crystallographic allomorphs, I_α and I_β, and exists in the form of microfibril. Sugiyama *et al.* [1991b] reported that a transition from monoclinic to triclinic region, with mixed region found in between, occurred along the microfibril of a green marine alga, *Microdictyon tenuius*: two domains of I_α and I_β coexisted alternately along the one microfibril. The localization of the two crystalline domains in the microfibril is of importance to understand the mechanism of crystallization as well as the biosynthesis of cellulose microfibrils. However, it is not straightforward to draw a general model for cellulose microfibrils, partly because of the structural diversity depending on the origins, and partly because of a lack of a direct method for analysis.

Atalla's group investigated the structure of nascent bacterial cellulose ribbons incubated in the presence of hemicellulosic materials [Atalla *et al.* 1993, Hackney *et al.* 1994]. Addition of such molecules resulted in the formation of I_β-rich fibrillated sub-fibrils that were different from I_α-rich ribbons in normal culture conditions. A microfibril model was then proposed where the I_β core sub-fibrils were packed in the superlattice of the I_α domain to form a ribbon-shaped microfibril [Hackney *et al.* 1994]. The model seems to explain well the selective crystallization into I_α and I_β of higher plant celluloses in terms of hemicellulosic deposition. However, electron diffraction obtained from *Microdictyon* [Sugiyama *et al.* 1991b] did not support the existence of such a superlattice. More recently in 1996, Yamamoto *et al.* proposed the hypothesis that I_α allomorph is crystallized under the stress induced by natural twisting behavior of bacterial cellulose ribbons. In this model, the central part of the ribbon, *i.e.* the vicinity of the twisting axis of the corresponding ribbon, is considered to be rich in I_β and the I_α fraction to increase in proportion to the distance from the center. If this is the case, I_α and I_β domains should be localized laterally rather than longitudinally.

These results on the ultrastructure of bacterial cellulose microfibrils stimulated the author to further investigate the microfibrils of a series of green marine algae. *Cladophora*, *Valonia* and *Boergesenia* were selected because the cellulose microfibrils of these species have been widely used for structural studies as standard highly crystalline materials. The microfibrils were hydrolized to form microcrystals, which were probed by precise microdiffraction to clarify how triclinic (I_α) and monoclinic (I_β) domains intermingled within a given microcrystal.

1.2 Materials and Methods

Materials

Three marine green algae, namely *Cladophora* sp., *Valonia ventricosa* and *Boergesenia forbesii*, were used as typical I_α-rich cellulose samples. *Boergesenia* was cultivated in the artificial marine water, Marine Art (Senju Seiyaku Co., Japan) with ES medium [Provasoli *et al.* 1957], while the other two were harvested from the sea bed in Chikura, Chiba, Japan (*C.* sp) and in the Lower Keys, Florida, USA (*V. ventricosa*), respectively. In comparison, microfibrillated tunicate cellulose from the tunic of *Halocynthia roretzi* (supplied by Daicel Chem., Co.) was used as it is considered to be consisting of I_β phase [Belton *et al.* 1989, Larrson *et al.* 1995] mostly.

Sample preparation – Purification and preparation of microcrystals

The sample was purified either by boiling in 0.05N NaOH for 8h followed by immersion in 0.05N HCl for 12h at room temperature, or by immersion in 1% KOH for 12h at room temperature before a treatment in 0.3% $NaClO_2$ buffered at pH 4.9 with acetate buffer for 3h at 70°C . The purification process was carefully monitored by FT-IR (described later) from the attenuation of 1600 cm^{-1} absorbance of non-cellulosic contaminants. The purified sample was then hydrolyzed either by boiling in 2.5N HCl for 12h, or by gentle stirring in 40% (w/v) H_2SO_4 for 3 days at 70°C, followed by dialysis after several washes in distilled water by centrifugation. Neither structural nor spectroscopic difference was detected in the resultant microcrystal specimens.

For the preparation of I_β-dominant microcrystals, a portion of the purified algal microcrystals was subjected to an hydrothermal treatment [Yamamoto *et al.* 1989]. For this, the specimen was autoclaved in a high pressure bomb at 260°C for 30 min in the presence of aqueous 0.1N NaOH.

Infrared spectroscopy

The suspension of microcystals was deposited on a glass slide and allowed to dry. Thin membrane was floated off onto water and mounted over the sample holder perforated by a 3mm hole. Fourier transform infrared spectra (FT-IR) were measured with a JASCO FT-IR 7000 spectrometer, which was operated in the absorbance mode with $4cm^{-1}$ resolution and 16 times integration in the range of $4600\text{-}400cm^{-1}$. Estimation of the I_α fraction was carried out using the integrated intensities of the two absorbance peaks at $750cm^{-1}$ and $710cm^{-1}$ that are respectively characteristic of I_α and I_β allomorphs [Sugiyama *et al.* 1991a].

Transmission electron microscopy

A drop of the microcrystal suspension was deposited on carbon coated copper grids and allowed to dry. The sample was observed with a JEOL JEM-2000EX II microscope

operated at an accelerating voltage of 100kV. The image was taken under diffraction contrast in the bright-field mode without prior contrast enhancement, using a low dose exposure – Minimum Dose System (MDS, JEOL). For diffraction analysis, the microdiffraction technique was primarily used [Sugiyama *et al.* 1991b]. To obtain an approx. 100nm diameter electron probe, a 20μm aperture was inserted in the condenser lens field and the first condenser was fully excited. The sample was observed under extremely low dose illumination with the help of a Gatan image intensifier (Model 622-0600). When an area of interest was found, the probe was focused to its smallest size (approx. 100nm diameter) and at the same time the dose was reduced to the minimum required for identification on the TV monitor. As soon as the sample was localized, the beam was blanked to prevent any unnecessary irradiation prior to image recording. Conventional selected-area electron diffraction diagrams were also taken from the area of about 2μm diameter in the specimen. All the images and diffractograms were recorded on Mitsubishi electron microscope films (MEM), which were developed with Copinal (Fuji Film Co., Japan) at 20°C for 6min. In addition, an analytical electron microscope JEOL JEM-2010 equipped with imaging plates (Fuji Film Co., Japan) [Mori *et al.* 1988] was used for the diffraction analysis in nanometeric scale region.

1.3 Results and Discussion

FT-IR measurement

All the FT-IR spectra obtained from the purified samples were well resolved and almost free of non-cellulosic contaminants. Enlarged spectra in the region from 800 to 500cm^{-1} are shown in Figure 1-1. Assuming that the absorptions at the above two peaks are proportional to the mass of I_α and I_β allomorphs, the I_α fraction value by IR (f_α^{IR}) was written as,

$$f_\alpha^{IR} = A_{750} / (A_{750} + kA_{710})$$

where A_x is the integrated intensity at the corresponding wave number and k is the ratio of adsorption coefficients (ε) between two peaks ($k = \varepsilon_{750} / \varepsilon_{710}$). In this thesis, k was estimated to be 0.16 by assuming the I_α fraction value of 0.64 for *Valonia* [Yamamoto & Horii 1993]. As summarized in Table 1-1, *Cladophora* cellulose was found to be the richest in I_α, followed by *Valonia* and *Boergesenia* cellulose. The f_α^{IR} in annealed *Cladophora* was estimated to be 0.24, which is larger than the previously reported values of annealed *Valonia* by ^{13}C NMR [Yamamoto & Horii 1993].

Taking the abundance of I_α allomorph and the large crystal size (20-30nm) into account, *Cladophora* cellulose was extensively investigated with further electron microscopy, while the others were used complementarily.

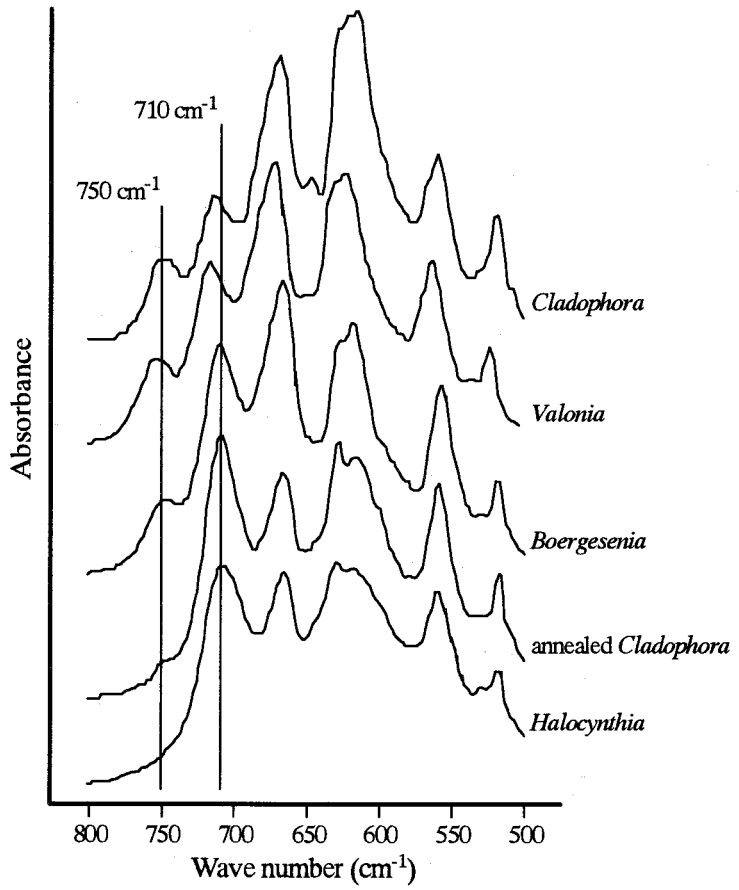

Figure 1-1.
FT-IR spectra of the specimens in the region of 800 to 500cm^{-1}. The absorbances at 750cm^{-1} and 710cm^{-1} are characteristic of I_α and I_β, respectively.

Table 1-1. I_α fractions in specimens of various origins

Sample	I_α fraction	± SE[*1]
Cladophora	0.76	± 0.01
Valonia	0.64 [*2]	± 0.01
Borgesenia	0.55	± 0.01
annealed *Cladophora*	0.24	± 0.03
Halocynthia	0 [*3] – 0.10 [*4]	-

[*1] standard error (n>8), [*2] *V. macrophysa* [Yamamoto & Horii 1993],
[*3] Belton *et al.* [1989], [*4] Larrson *et al.* [1995]

Electron diffraction

Figure 1-2 shows typical selected-area fiber-diffraction diagrams obtained from a delaminated cell wall of both initial and annealed *Cladophora*. Apparently the diffraction patterns are easily distinguishable especially by the intensities on the third layer line and meridians as reported for *Valonia*. Initially (Figure 1-2A), the triclinic character was well

demonstrated due to asymmetrical diffraction spots occuring in the upper-left hand and upper-right hand quadrants as indicated by arrowheads. Upon annealing, the pattern became simpler as shown in Figure 1-2B, where the initial triclinic character changed to a monoclinic one. This was accompanied by an increase of the $(002)_m$ meridional intensity. Such structural features were identical to those obtained with the previous *Valonia* [Sugiyama *et al.* 1990] and *Microdictiyon* [Sugiyama *et al.* 1991b] celluloses.

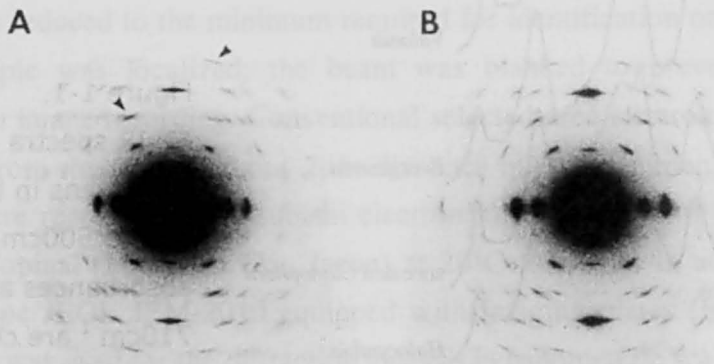

Figure 1-2. Selected area electron diffraction fiber diagrams obtained from original (A) and annealed (B) *Cladophora*. Note that the arrowheads indicate typical triclinic asymmetrical reflections on the 3rd and 5th layer lines.

More than 200 microdiffraction diagrams from initial *Cladophora* microcrystals were analyzed. A typical example is presented in Figure 1-3 where the diagram on the left exhibits perfect triclinic symmetry while that on the right corresponds to a monoclinic b^*c^* pattern. The analysis of all the diagrams confirmed the general concept that the microfibril possesses two domains, namely one-chain triclinic and two-chain monoclinic crystals. The unit cell parameters obtained from *Cladophora* cellulose were a=0.670nm, b=0.595nm, c=1.036nm (chain axis), α=118°, β=114°, γ=79.7° for the one chain cell (calculated over 25 independent reflections), and a=0.798nm, b=0.809nm, c=1.036nm, γ=96.8° for the two chain cell (16 reflections). These parameters were quite similar to the previous data [Sugiyama *et al.* 1991b] obtained from *Microdictyon* cellulose a=0.674nm, b=0.593nm, c=1.036nm (chain axis), α=117°, β=113°, γ=81° for the one chain cell (calculated over 27 independent reflections), but slightly different from a=0.801nm, b=0.817nm, c=1.036nm, γ=97.3° for the two chain cell (38 reflections). As in the case of *Microdictyon*, d-spacing data from annealed cellulose were incorporated for refining the I_β cell parameters, the variation in parameters may reflect structural difference and/or imperfection between initial and annealed I_β cellulose crystals.

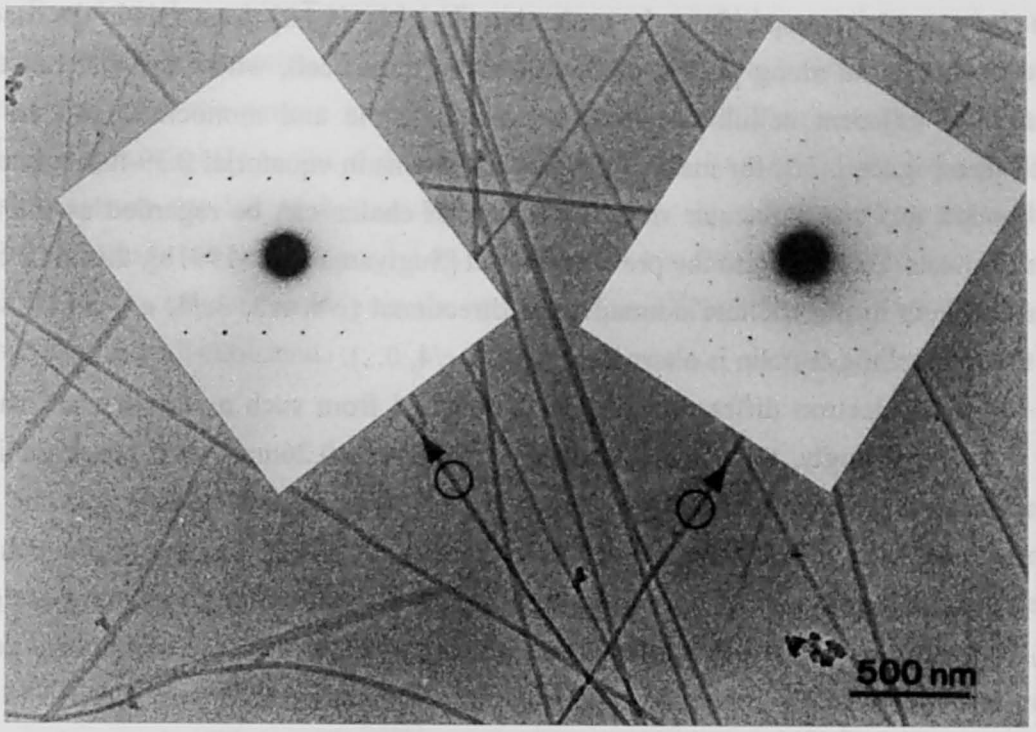

Figure 1-3. A typical specimen preparation of *Cladophora* cellulose microfibrils together with microdiffraction patterns from ca. 100nm diameter region. The diagram on the left shows one from the triclinic crystals, while that on the right shows one from the monoclinic crystals.

Single-phased diagrams, such as the one showing pure triclinicity as on the left side in Figure 1-3, were less frequently observed than in the case of *Microdictyon* cellulose. In most cases, diagrams contained diffraction spots from two structures: the ratio of the two structures was found to vary although the author could not measure their relative amounts. This observation implies that in *Cladophora* cellulose, either the two phases are more intimately associated with each other than in *Microdictyon* cellulose, or that the electron probe diameter in this experiment (*ca.* 100nm) may have been too large [Sugiyama *et al.* 1991b]. To rule out the latter technical problem, the author tested the same sample with an analytical electron microscope (JEM-2010) equipped with imaging plates. Microdiffraction diagrams from circular areas 20nm in diameter were successfully recorded on a microfibril (not shown here) and gave results similar to those above. Therefore, the author concluded that the two crystalline domains were more intimately associated than in the case for *Microdictyon* [Sugiyama *et al.* 1991b].

Among the diagrams that contain both triclinic and monoclinic spots, the projection parallel to the equatorial 0.39-nm lattice planes and perpendicular to the fiber axis has a

unique character. It corresponds to the projection along the $[1\,\bar{1}\,0]_t$ zone axis in the case of the triclinic unit cell and along $[010]_m$ of the monoclinic unit cell, where the difference in the translation of adjacent cellulose chains between triclinic and monoclinic can be clearly detected (see Figure 1-5B, for instance). Since the chains in equatorial 0.39-nm lattice planes are H-bonded to form molecular sheets, the shift of chains can be regarded as the shift of molecular sheets. According to the previous model [Sugiyama *et al.* 1991b], this shift between molecular sheets in the triclinic domain is unidirectional ($c/4$, $c/2$, $3c/4$, c, $5c/4$...), whereas that in the monoclinic domain is alternating ($c/4$, 0, $c/4$, 0...).

Typical electron diffraction diagrams obtained from such a situation are shown in Figure 1-4. Surprisingly, three meridional reflections (*ca.* 0.26nm) were observed in most experiments with *Cladophora* cellulose (1-4A & 1-4B). These are merged into one streaky peak in selected-area diffractions (for example, see Figure 1-2A). The one in the center was assigned to $(004)_m$ reflection from monoclinic region, while the other two were assigned to $(\bar{1}\,\bar{1}\,4)_t$ from triclinic. This phenomenon was not observed in the case of tunicate cellulose that consists mostly of I_β monoclinic cellulose (1-4F), and therefore is specific to I_α-rich cellulose. As shown in the enlarged meridional spots (1-4B to 1-4E), the number of spots varies from area to area, although there are at least two spots in most cases.

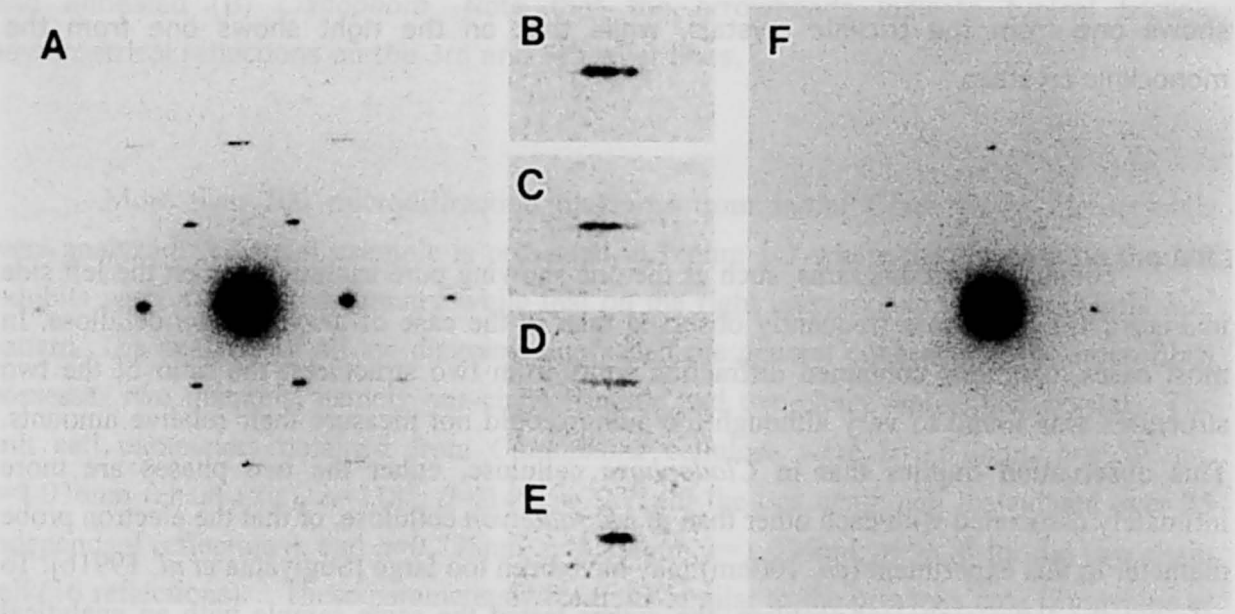

Figure 1-4. Microdiffraction diagrams obtained from the projection perpendicular to the fiber axis and parallel to the 0.39-nm lattice planes. Zone axes are defined as $[1\,\bar{1}\,0]_t$ for the triclinic diagrams and $[010]_t$ for monoclininc diagrams. The fiber axis is vertical. Diagram A was obtained from initial *Cladophora*, and that in F was obtained from *Halocynthia*. B to E show the enlarged meridional reflections from initial *Cladophora*, *Valonia*, *Valonia*, and *Boergesenia*, respectively.

Based on the published model [Sugiyama *et al.* 1991b] as well as on the unit cell parameters obtained from this experiment, the triclinic reciprocal net in the corresponding projection that gave the pattern in Figure 1-4 was schematically represented in Figure 1-5. The $(\bar{1}\,\bar{1}\,4)_t$ spot, slightly to the right of the meridian, clearly indicates that the triclinic *ab* plane slopes from top-left to bottom-right. Accordingly, the corresponding plane is from top-right to bottom-left when the $(\bar{1}\,\bar{1}\,4)_t$ spot appears on the left-side. On the other hand, monoclinic $(004)_m$ appears exactly on the meridional axis. Thus the nature of the three spots in the meridian is well explained.

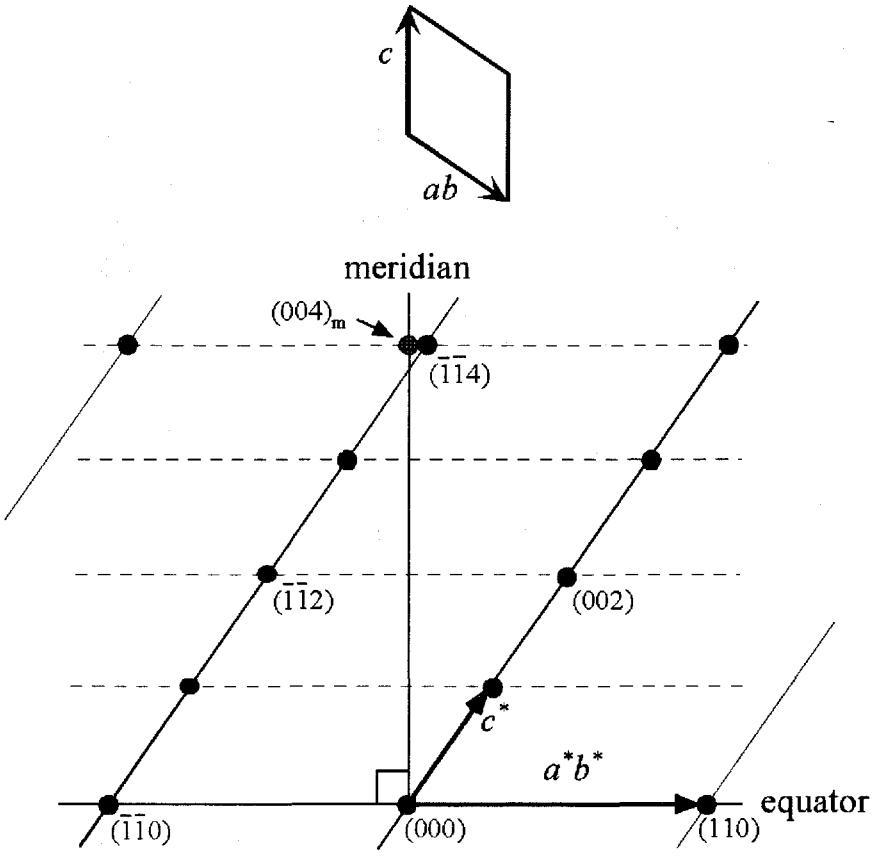

Figure 1-5. A schematic representation of the real and reciprocal lattice in the same projection as in Figure 1-4. Note that the triclinic $(\bar{1}\,\bar{1}\,4)_t$ is not exactly on the meridian.

The molecular packing that gives the diffraction diagram in Figure 1-4A can be schematically drawn as in Figure 1-6B. In this projection, the structural differences between triclinic and monoclinic units are quite clear in that the asymmetric unit, *i.e.* cellobiose, in the triclinic system, shows unidirectional shifts of *c*/4 between adjacent molecules, whereas in the monoclinic system, it shows alternatively up and down c/4 translations. Assuming that the

direction of the triclinic *ab* slope is altered (*i.e.* downward to upward) in the middle of the microfibril, two triclinic crystals can be drawn, one being obtained from the other by a 180° rotation around *c*-axis, followed by a *c*/2 translation along *c*-axis. Interestingly, one can notice that the chain packing between these two triclinic domains has, in fact, monoclinic characteristics. Furthermore, the author did not find any defect as seen in the projection parallel to the chain direction (Figure 1-6A), which is consistent with the previously reported cross sectional images on algal cellulose microfibrils [Revol 1982, Sugiyama *et al.* 1985b].

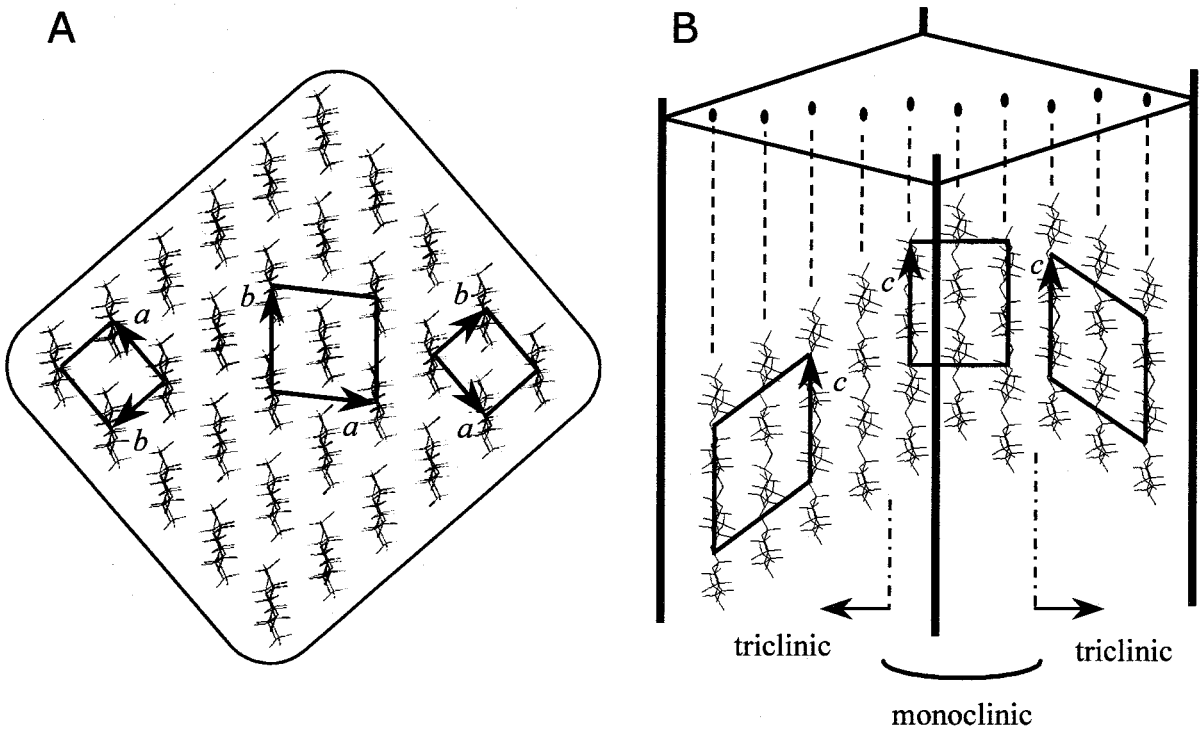

Figure 1-6. Packing of 0.39-nm molecular sheet in a microfibril having two triclinic domains separated by a monoclinic domain. **A**: view along the chain direction. **B**: view along $[1\bar{1}0]_t$ (triclinic) and $[010]_m$ (monoclinic) directions.

Figure 1-7 is a schematic representation of the relationship between the shift of chains and the corresponding diffraction patterns. Diagrams A to C show triclinic/monoclinic composites, while D is a fully monoclinic crystal. In *Cladophora* and *Valonia* cellulose microfibrils, situation A was the most frequently observed, followed by B. When the translational shift is frequently altered as in B, a microfibril consists of multiple domains of both triclinic and monoclinic crystals. In such a case, the streaking of the meridional diffraction spot occurs perpendicularly to the translational defects, the interfaces between

triclinic and monoclinic domains. This phenomenon was sometimes observed in the case of *Cladophora* and *Valonia*. As for *Boergesenia* cellulose, the diagram of two spots, shown in C, was most frequent. Though the above explanation do not include all the situation and may be oversimplified, it is helpful to understand how the directionality and frequency of the translational shifts results in the formation of nano-domain structures consisting of I_α and I_β.

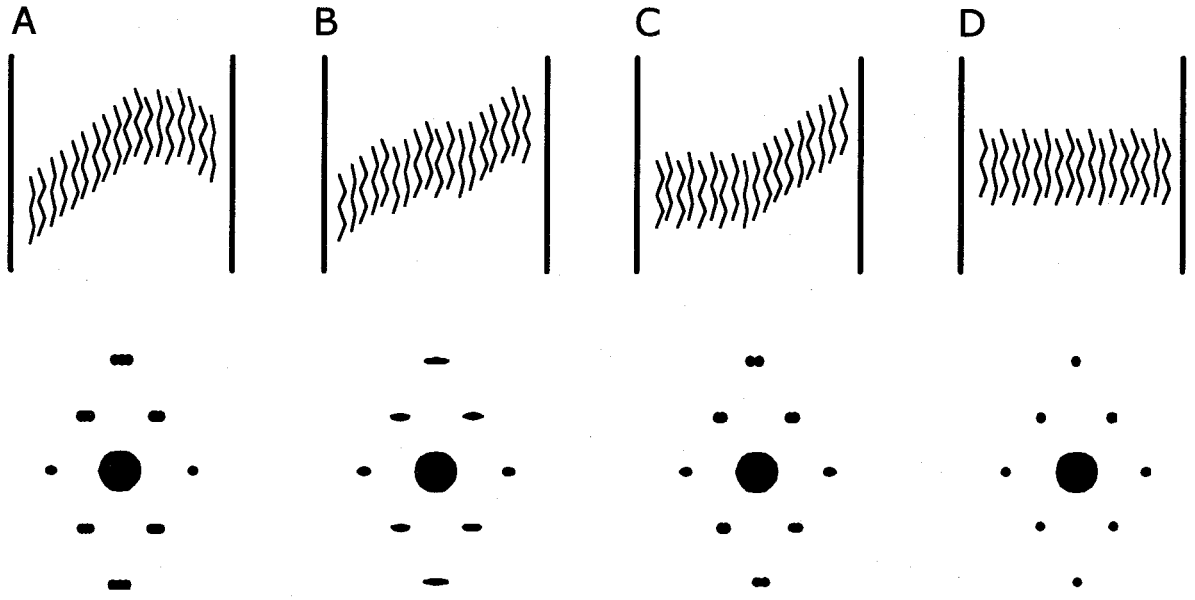

Figure 1-7. A probable molecular sheet packing explaining the difference in the diffraction diagrams in Figure 1-5. Each line indicates cellotetraose. **A**: two triclinic domains with a monoclinic domain in between. **B**: multiple domains of triclinic and monoclininc domains. **C**: triclinic and monoclinic domains. **D**: perfect monoclinic domain.

In summary, the two allomorphs in algal celluloses consist of crystalline domains long along the molecular direction. These domains can coexist alternatively both along the microfibril length and across laterally. When they coexist laterally, the interface between the two domains would be the H-bonded molecular sheets of cellulose. The detailed manner in which these two domains intermingle seemed also to vary depending on the algal cellulose origins.

Ultrastructural aspects of acetylation of *Valonia* and *Halocynthia* celluloses were investigated by electron microscopy, and a considerable reduction in the diameter of the crystalline domain was observed [Sassi 1995] due to a continuous stripping of the surface chains as they became acetylated. Interestingly, during the initial stage of acetylation, the

cross sectional shape of *Valonia* crystals became smaller polygonal as if some part of its lateral face had been specifically and sharply wedged off, while that of *Halocynthia* crystals was evenly rounded. This process was further investigated by ^{13}C NMR and FT-IR [Sassi & Chanzy 1995] respectively by deconvoluting the C1 resonance and the absorbances at 3240cm^{-1} and 3270cm^{-1} into the fractional amount of I_α, and both measurements showed that the I_α crystals were more susceptible to acetylation. These results allow envisaging that in *Valonia,* there are multiple intermingled domains separated by crystallographic boundaries as assumed in the model proposed here. Furthermore, the area closer to the surface would be primarily occupied by the I_α allomorph as also suggested by high resolution atomic force microscopy imaging on *Valonia* microcrystals [Baker *et al.* 1997].

As the enzymatic degradation of cellulose allomorphs is another important method to deduce structural information, the crystalline and morphological structures of *Cladophora* and *Halocynthia* celluloses during hydrolysis by *Trichoderma* cellulase were investigated [Hayashi *et al.* 1997]. Again, at the initial stage of hydrolysis, the I_α crystalline component was more rapidly and selectively degraded than I_β crystals. The ultrastructural appearance of residual cellulose crystallites after hydrolysis was also found different: *Cladophora* microcrystals became shortened and fibrillated, whereas *Halocynthia* microcrystals were primarily fibrillated. The results favor that in *Cladophora*, cellulose I_α and I_β domains would localize alternatively along the microfibril axis.

The model proposed here, where two structures coexist in each microfibril, alternating either longitudinally or laterally, having interfaces between adjacent H-bonded molecular sheets, is still speculative. However, it should be most suitable in order to explain all the details in diffraction data of algal cellulose investigated here as well as the above mentioned acetylation and enzymatic degradation experiments.

In vitro [Kudlicka *et al.* 1995] and abiotic [Lee *et al.* 1994] synthesis of cellulose has generated extremely thin microfibrils (about 1.1 to 1.3nm), suggesting that cellulose sheet formation was the first stage of microfibril formation. Recent molecular dynamic simulations [Cousins & Brown 1995] reported that the molecular sheet bonded by van der Waals forces was the first to form. The second step of crystallization was the piling up of the sheets to form a squarish or rectangular cross section. If this is the case, one would have difficulty to build up the diversity in the translation of cellobiose unit along the *c*-axis. The microfibril model described here will help explain biosynthesis, crystallization, surface structure as well as chemical and enzymatic accessibilities of algal cellulose.

1.4 Abstracts

Ultrastructural localization of cellulose IR and I_α allomorphs in one microfibril from algal sources was investigated using electron microdiffraction. Both cellulose IR and I_α were characterized as one-chain triclinic and two-chain monoclinic unit cells, respectively, in agreement with previous studies. These two structures coexisted in each microfibril, alternating either longitudinally or laterally. The transition zone between the two phases was found to be the interface between adjacent H-bonded molecular sheets (*i.e.,* 0.39-nm lattice planes).

2. Localization of I_α Domain in *Cladophora* Cellulose (II)

-Phase Analysis of High Resolution Electron Microscopic Image-

2.1 Introduction

Transmission electron microscopy is a very powerful tool to study the structure of crystalline materials at the nanometric scale. In particular, high resolution electron microscopy (HREM) can be used to analyze regions which are too small to be clearly resolved by dark field (DF) imaging. However, it is very difficult to record molecular images of polymers as they undergo massive radiation damage when probed by an electron beam. The instrumental resolution is not really an issue here as recent electron microscopes can achieve typical resolutions of 0.2nm or better. Two factors will mainly influence the success rate during the observation of radiation sensitive materials, *i.e.*, sample stability and imaging conditions. Several techniques have been recently developed in order to improve both factors. On the one hand, the mechanical/thermal drift and sample degradation can be decreased by performing the observation at liquid helium temperature, with a specimen mounted on photo-etched flat microscope grids and 'sandwiched' between two ultra-thin carbon films [Fujiyoshi 1998]. On the other hand, the so-called 'low dose' methods have been implemented on the recent generation of microscopes. They allow setting up the focus conditions on an area nearby the region of interest in order to prevent any unnecessary irradiation prior to actual image recording. Nevertheless, several problems remain:

1) It is not possible to finely improve the crystal orientation with respect to the electron beam, so it is difficult to record images where more than one family of molecular planes are visible.
2) As the images must be recorded at magnifications typically below 50,000×, it is difficult to set up the objective lens defocus with enough precision to ensure optimal HREM imaging conditions (*i.e.* at Scherzer defocus).
3) The operator has to make a compromise between magnification and dose. While at lower magnifications, the granularity of the photographic film will limit resolution, at higher magnifications, the film will have to be underexposed in order to limit the radiation dose, resulting in a picture with a low signal-to-noise ratio (S/N). Another effect of underexposure is that the transfer function of the microscope cannot be properly recorded on the photographic plate.

Crystalline polysaccharides are certainly among the most sensitive polymers as far as exposure to highly accelerated electrons is concerned. The doses for which the crystallinity is decreased by half typically range from 4 to 6 electrons per $Å^2$. However, it has been possible to record lattice as well as column images of polysaccharides. Examples can be found in the case of cellulose fibers [Sugiyama *et al.* 1984, 1985a & 1985b, Helbert *et al.* 1998], chitin

fibers [Gaill *et al.* 1992, Saito *et al.* 1995], chitin single crystals [Helbert & Sugiyama 1998], as well as amylose plate-like crystals [Putaux *et al.* 1995]. In these studies, point resolutions up to 0.39nm could be achieved, at both very low and room temperatures.

Even when the imaging conditions have been optimized, a visual inspection of the pictures remains difficult because of the low S/N. Therefore, more sophisticated methods based on the computer processing of numerical images are necessary to enhance the periodic signal of the crystalline areas. For instance, Bragg filtering and real-space averaging are frequently used, although special care must be taken to prevent (or at least monitor) the artifacts that might be introduced during the calculation. However, detecting the distribution and geometry of the diffracting domains in a low S/N image is to be improved.

A new method has been recently introduced by Hÿtch [Hÿtch & Gandais 1995, Hÿtch 1997] and successfully applied to HREM images of various radiation-stable materials recorded at high magnification: cadmium sulphide nanocrystals embedded in an amorphous matrix [Hÿtch & Gandais 1995], antiphase domains in Cu_3Au [Hÿtch & Potez 1997], domain walls in ferroelectric materials [Hÿtch *et al.* 1998] and carbon nanotubes deposited on carbon films [Hÿtch 1997]. They have detected crystalline domains and characterized their size by using the amplitude and phase information of the periodic signal recorded in the images.

Native crystalline cellulose is known to be a composite of two allomorphs, namely I_α and I_β [Atalla & VaderHart 1984, Sugiyama *et al.* 1991b]. Their distribution pattern in a microcrystal depends on the origin of cellulose. Both allomorphs alternate longitudinally in *Microdictyon* [Sugiyama *et al.* 1991b] while the alternation is both longitudinal and lateral in *Cladophora* and other green marine algae [Imai & Sugiyama 1998]. Electron diffraction has contributed to solving the distribution of I_α and I_β. Thus, one can expect that a direct visualization of the cellulose lattice planes using HREM will help corroborate these results. In this chapter, the author used the method of amplitude and phase imaging to assess the quality of crystalline domains in HREM pictures of *Cladophora* cellulose microfibrils. To the author's knowledge, it is the first time that this method has been applied to highly noisy HREM pictures of radiation-sensitive materials.

2.2 Materials and Methods

Sample preparation

Cladophora, a green marine alga, was harvested at sea bed in Chikura, Chiba, Japan. After purification, some samples were annealed to I_β-rich cellulose by a hydrothermal treatment [Yamamoto *et al.* 1989]. The procedure for the purification and the hydrothermal treatment are described in 1.2 in this thesis. A characterization of these samples by FT-IR provided I_α fractions of 0.76 and 0.24 for initial and annealed *Cladophora*, respectively [Chapter 1, Imai & Sugiyama 1998]. Specimens for DF imaging were prepared as follows: under a stereomicroscope a pair of tweezers was used to delaminate the cell wall and obtain a uniaxially oriented lamella that was deposited on a carbon-coated copper grid. For HREM, these specimens were disintegrated into cellulose microcrystals by acid hydrolysis with H_2SO_4 (the detailed procedure is described in 1.2). A drop of the microcrystals suspension was allowed to dry on a gold-coated holey carbon microgrid [Fukami & Adachi 1965] previously coated with an ultra thin carbon film. An additional ultra thin carbon film was evaporated onto the grid in order to increase the mechanical stability and electrical conductivity of the samples to be observed at very low temperature [Fujiyoshi 1993, Jakubowski *et al.* 1989].

Electron microscopy

DF micrographs were obtained using a JEOL JEM-2000EXII microscope operated at an accelerating voltage of 100kV and a magnification of 5,000×, with help of the Gatan image intensifier. A 100μm objective aperture was inserted in the back focal plane to select any of the following reflections: $(110)_t$, $(010)_t + (100)_t$, and $(\bar{1}\bar{1}4)_t$. In particular, in order to record the $(110)_t$ DF image, the specimen was tilted by 40° around the fiber axis to bring the corresponding lattice planes into Bragg condition. No tilting was used for the other reflections. The images were recorded on the Mitsubishi MEM films and developed with Copinal.

For lattice imaging, two transmission electron microscopes were used: a Philips CM200 'Cryo' microscope operated at 200kV at room temperature and equipped with a single-tilt side-entry specimen holder, as well as a JEOL JEM-4000SFX microscope operated at 400kV, the specimen being placed in a top-entry holder inserted in a chamber cooled down to 4.2K by liquid helium [Fujiyoshi *et al.* 1991].

Both microscopes were equipped with their own limited dose systems (Low Dose System for Philips, and Minimum Dose System for JEOL). Fibers were first selected at low magnifications (< 1,000×) and focus was set at a higher magnification in an area nearby the region of interest. The beam was then blanked until actual image recording, at magnifications of 27,500× and 38,000× on the Philips microscope and 30,000× on the JEOL one. With the Philips microscope, Agfa Scientia films were used and developed with Agfa G128 developer

for 5min at 20°C. With the JEOL microscope, Mitsubishi MEM films were used and developed in Kodak D19 for 5min at 20°C.

Image processing

The original negatives were first sorted out using laser diffractometry on an optical bench in order to rapidly select the pictures exhibiting diffracting areas. Special care was taken to calibrate the optical diffraction spots and sort the regions of interest depending on the type of reflection that was observed. The selected areas were then enlarged and digitized using an 8 bits black & white Kodak Megaplus digital CCD camera. Sampling densities of 0.14, 0.18 and 0.19nm/pixel were achieved for corresponding magnifications on the original negatives of 38,000×, 30,000× and 27,500× respectively. The numerical images were transferred either on a desktop computer equipped with a Pentium processor or a Silicon Graphics workstation and processed using the Semper 6.4 program [Saxton *et al.* 1979].

A digital image is a network of pixels which can be defined by their position $\boldsymbol{r}$ and intensity $I(\boldsymbol{r})$ (also called gray level). In the Fourier transform of the image, pixels have the position $\boldsymbol{f}$ (spatial frequency) and complex intensity $\tilde{I}(\boldsymbol{f})$. If an image contains a periodical signal, its Fourier transform reveals a symmetrical pattern of strong frequency components $\boldsymbol{g}$ – the Bragg reflections. Practically, these components are more easily detected in the power spectrum (PS) of the image, *i.e.* the real function $|I(\boldsymbol{r})^* \tilde{I}(\boldsymbol{f})|$, but the calculation are performed on the Fourier transform $\tilde{I}(\boldsymbol{f})$. By masking the frequencies around a couple of reflections $\pm\boldsymbol{g}$ and performing an inverse Fourier transform, a Bragg filtered image is obtained in which the lattice lines associated to $\pm\boldsymbol{g}$ are enhanced:

$$B_g(\boldsymbol{r}) = 2A_g(\boldsymbol{r}) \cos\left[2\pi \boldsymbol{g}\bullet\boldsymbol{r} + P_g\right] \qquad (1)$$

A_g is the amplitude of the signal and P_g the phase, the positional information with respect to an origin (Figure 2-1). If the signal is uniform, both amplitude and phase are constant.

Let us consider a periodical signal that is finite in the image, as would be the case for a crystalline fiber deposited on an amorphous carbon film. In the Fourier space, the information about the position of the boundaries is distributed in the vicinity of the major reflections. If the mask used for filtering is too narrow, this information may be lost and in the Bragg filtered image, the signal may extend out of the geometrical limits of the fiber. This artifact will thus increase the apparent width of the fiber.

An important factor to take into account is the noise which is very high in the pictures of polymers. For polysaccharides, S/N is no better than 5% in most cases [Stewart 1988]. Let's assume that, in first approximation, the image of the fiber can be described as the sum of periodic signals and random noise. The information about noise will be scattered

everywhere in the Fourier space. The circular mask used to select the strong reflections will also include a certain amount of information related to the noise. If the signal is very low, as in the case of cellulose, the influence of this noise component will not be negligible and in the Bragg filtered image, the lattice fringes will fluctuate in intensity and spacing. Lattice 'dislocations' may sometimes be observed, their position depending on the diameter of the filtering mask and the proportion of noise included. These dislocations are artifactual and do not correspond to actual structural defects.

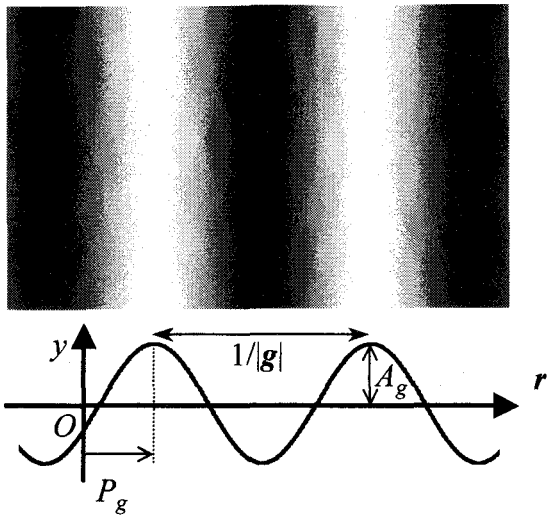

Figure 2-1. Definitions of the amplitude (A_g) and phase (P_g) for a periodic signal as described by equation (1).

Although Bragg filtering is easy to carry out, in the case of low S/N images, it can induce artifacts which mostly depend on the diameter of the mask that is applied. For this reason, it was interesting to use another approach which was not so strongly dependent on the filtering conditions.

If the signal fluctuates, expression (1) becomes:

$$B_g(\boldsymbol{r}) = 2A_g(\boldsymbol{r}) \cos [2\pi \boldsymbol{g}\bullet\boldsymbol{r} + P_g(\boldsymbol{r})] \qquad (2)$$

In the method described by Hÿtch and Gandais [1995], the function $P_g(\boldsymbol{r})$ is retrieved and analyzed in detail. It has to be emphasized that this phase is not that of the electron wavefunction emerging from the crystal but the information related to the position of the lattice fringes with respect to a fixed origin. In that sense, Hÿtch and Gandais preferred using the term 'geometric phase' [1995].

Practically, a circular mask is applied around a single reflection $\boldsymbol{g}$ in the complex full-plane Fourier transform. Then the Fourier image is recentered around the selected reflection and back Fourier transformed. A complex image is obtained from which the corresponding $A_g(\boldsymbol{r})$ and $P_g(\boldsymbol{r})$ are calculated. For the phase image, the procedure is equivalent to subtracting the term $2\pi\boldsymbol{g}\bullet\boldsymbol{r}$ from the phase term of the Bragg filtered image expressed in (2). The final phase image is obtained after rescaling the intensities between $-\pi$ (black) and π (white). As an image processing software like Semper can handle complete images in its calculation, by using the proper set of commands, it becomes possible to visualize the amplitude and phase information and their variation in the whole image. The strong point of this method is that the phase information is rather insensitive to noise. The reason has been explained in details by Hÿtch and Gandais [1995].

An interesting problem arises when one considers a small variation of the lattice spacing which corresponds to a variation $\Delta\boldsymbol{g}$ in the reciprocal space. In that case, when expression (2) is written for $\boldsymbol{g}+\Delta\boldsymbol{g}$, it becomes:

$$B_g(\boldsymbol{r}) = 2A_g(\boldsymbol{r}) \cos\left[2\pi\boldsymbol{g}\bullet\boldsymbol{r} + 2\pi\Delta\boldsymbol{g}\bullet\boldsymbol{r} + P_g(\boldsymbol{r})\right]. \qquad (3)$$

A uniform ramp corresponding to residual term $2\pi\Delta\boldsymbol{g}\bullet\boldsymbol{r}$ is thus added to the phase. If the filtering mask is kept centered around $\boldsymbol{g}$, the residual can be detected in the phase image as a ramp of gray levels.

2.3 Results and discussion

Bourret *et al.* [1972] used DF imaging to investigate *Valonia* cellulose microcrystals. They incorporated all three equatorial reflections to form DF images, whereas in this chapter, the author used individual reflections: $(110)_t$ as well as $(100)_t$ and $(010)_t$ which could not be separated because no small enough objective aperture was available (Figure 2-2A). In the latter case, the $(010)_t$ is generally the most intense reflection as the microfibrils have a preferential orientation on the supporting carbon film. The corresponding DF images can thus be regarded as primarily due to the diffraction of the $(010)_t$ lattice planes.

Figure 2-2 shows typical DF images (B-D) together with selected-area electron diffraction diagrams (A) recorded from the same sample preparation. The crystalline areas satisfying the Bragg condition are bright. In the image corresponding to the meridional $(\bar{1}\bar{1}4)_t$ reflection (Figure 2-2D), the contrast is uniform along the microfibrils. This means that the fibers are quite flat on the supporting carbon film so that the meridional planes remain in Bragg condition along a large length. Conversely, in Figures 2-2B and 2-2C, the diffracting areas are of limited lengths. As the selected equatorial reflection corresponds to longitudinal

planes, the variations in contrast are not due to any discontinuity of crystallinity but most probably to some twisting effect.

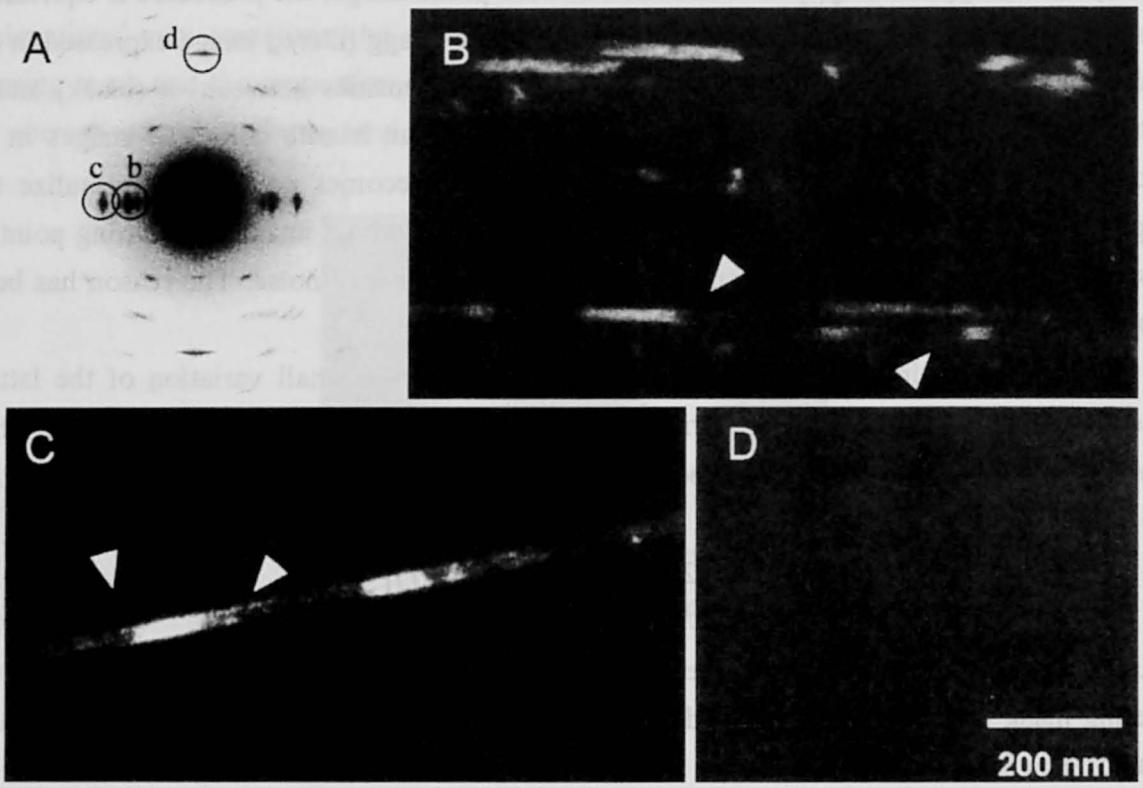

Figure 2-2. Typical dark-field images of cellulose microfibrils, formed by selecting equatorial $(100)_t$+$(010)_t$ (B), $(110)_t$ (C), and meridional $(\bar{1}\,\bar{1}\,4)_t$ (D) reflections in the cellulose I diffraction diagram (A). The bright region in each DF image relies on each reflection circled in A (b-d).

While DF imaging was useful to get an overview of the diffracting areas, the direct visualization of the lattice planes in the corresponding area by HREM was expected to provide additional information. The image decomposition procedure previously described was carried out to retrieve the amplitude and phase of the lattice fringes from obtained images. In the amplitude image, the brighter the intensity, the higher the amplitude of the fringes. The amplitude image cannot be used to differentiate two domains with different lattice spacings or shifted with respect to one another as both of them appear bright. In the phase image, domains exhibiting lattice fringes are identified by a more or less constant gray level, whereas amorphous regions can be recognized by a fluctuating intensity with sharp transitions from white to black. These transitions are a consequence of the renormalization of the phase

between $-\pi$ and π. If the phase gets higher than π, it will be renormalized above $-\pi$. In an image, a geometrical shift between two domains with identical lattice spacings $1/|\boldsymbol{g}|$ generates a phase shift. If the shift is half of the lattice spacing, the phase is shifted by π. Each domain thus appears with a different average gray level. If two domains have different lattice spacings or if they are rotated with respect to one another, two reflections will be observed in the diffractogram. If these reflections are very close and if one is chosen as a reference to center the filtering mask, the formalism of expression (3) can be applied. In the resulting phase image, the domain corresponding to the reference reflection will exhibit a constant gray level and the other domain will appear as a ramp of grays. In addition, the direction of the ramp and that of $\boldsymbol{\Delta g}$ are the same. If an average position in-between both reflections is chosen, then both domains will exhibit ramps of grays.

The resolution of the method is directly related to the mask size [see Hÿtch and Gandais 1995]. The smaller the mask, the higher the resolution, although the appearance of the resultant image may be more ambiguous. The mask size the author set was $|\boldsymbol{g}|/16$, the priority being given to the readability of the phase image at the expense of resolution.

The lattice spacing in experimental HREM images of polysaccharides will not remain constant across the whole field of view, due to crystal imperfections, radiation damage, misalignments or optical distortions. Thus, the exact position of the selected reflection $\boldsymbol{g}$ is just arbitrary and average in a domain. Nevertheless, the analysis of the phase $P_g(\boldsymbol{r})$ is expected to indicate variations of the spacing and relative position of lattice fringe in a microcrystal.

Figure 2-3 shows the $(010)_t$ lattice image of *Cladophora* cellulose (A) and the corresponding image decomposition (B-D). A high amplitude and a rather stable phase were retrieved along a long region of the microcrystal (Figure 2-3C and 2-3D). Such a homogeneous region sometimes extended over 500nm in length or more. This indicates that the signal is uniform as also shown in the Bragg-filtered image of Figure 2-3B. This means that the $(010)_t$ lattice planes, which correspond to the molecular sheets formed by van der Waals force, are well ordered. The author drew a similar conclusion from I_β-dominant hydrothermally treated specimens which provided well-ordered $(010)_t$ fringes.

The lattice fringes in the initial image of Figure 2-4A are hardly visible, as confirmed by the low amplitude in Figure 2-4B. Interestingly, the PS contains both $(110)_t$ and $(\bar{1}\bar{1}2)_t$ reflections, the latter being stronger. After Bragg filtering, the lattice lines are not visible over the whole microcrystal, but are distributed in separate regions (Figure 2-4B). Each domain appears to have a distinct average phase value (Figure 2-4D). Moreover, gradients in gray levels are observed for the domain 1, while the effect is weaker in the domain 2. As previously explained, this indicates that a splitting of the $(\bar{1}\bar{1}2)_t$ reflection has to be considered and that the split can be related to close but slightly different lattice spacings. Indeed, a careful examination of PSs from different lattice images showed that such an effect

existed for initial *Cladophora* cellulose (Figure 2-6B). However, this observation has to be considered with care as other factors such as a misalignment or twist of the microcrystal, as well as radiation damage, cannot be totally ruled out.

The amplitude and phase information in $(\bar{1}\bar{1}2)_t$ lattice images of annealed I_β-rich *Cladophora* cellulose (Figure 2-5) provided a different impression from those of initial I_α-rich *Cladophora* cellulose: the signal is continuous along the fiber image. In addition, the reflections observed in the PS are spot-like (Figure 2-6C). This suggests that I_β cellulose has a homogeneous molecular stacking, *i.e.* a more uniform structure.

The image decomposition provided several results as follows:

1) The phase shift of the $(\bar{1}\bar{1}2)_t$ lattice planes was observed in *Cladophora* cellulose microcrystal.
2) The phase shift the corresponding $(102)_m$ lattice lines disappeared in annealed *Cladophora* cellulose.
3) The $(010)_t$ lattice planes showed a homogeneous distribution of phase in both specimens.

Thus, imperfections of molecular packing of I_α-rich cellulose are visible in the $[1\bar{1}0]_t$ projection, where the $(110)_t$ and $(\bar{1}\bar{1}2)_t$ are projected. This conclusion is substantiated by the splitting effect observed for the $(\bar{1}\bar{1}2)_t$ reflection. It has to be noted that an identical phenomenon was observed in microdiffraction diagrams [Chapter 1, Imai & Sugiyama 1998], indicating that an imperfection of molecular ordering in the $[1\bar{1}0]_t$ projection certainly occurred in I_α-rich cellulose. Therefore, the working model proposed in Chapter 1 (Figure 1-6 & 1-7) should be supported: the lateral transition between I_α and I_β is located between adjacent H-bonding molecular sheets, *i.e.* the $(110)_t$ lattice planes. The distribution pattern of such domains varies depending on the cellulose sources, as shown in Figure 1-7.

The mini-sheet hypothesis has been recently proposed for the biocrystallization system of native cellulose. Molecules are stacked by van der Waals force to form the $(1\bar{1}0)_m$ or $(010)_t$ lattice planes at the first stage and consequently piled into a crystal with rectangular cross-section by H-bonding [Cousins & Brown 1995]. If this is the case, the molecular sheets bonded by van der Waals forces, the $(1\bar{1}0)_m$ or $(010)_t$ lattice planes should be regularly piled up into a microcrystal. This is consistent with the results of the phase imaging presented in this chapter. In the projection showing $(\bar{1}\bar{1}2)_t$ lattice planes, a gap was observed between separate domains (Figure 2-4). This might indicate that heterogeneous regions are nested during the second step of crystallization through H-bonding and explain the origin of the complex distribution of I_α and I_β in a microcrystal.

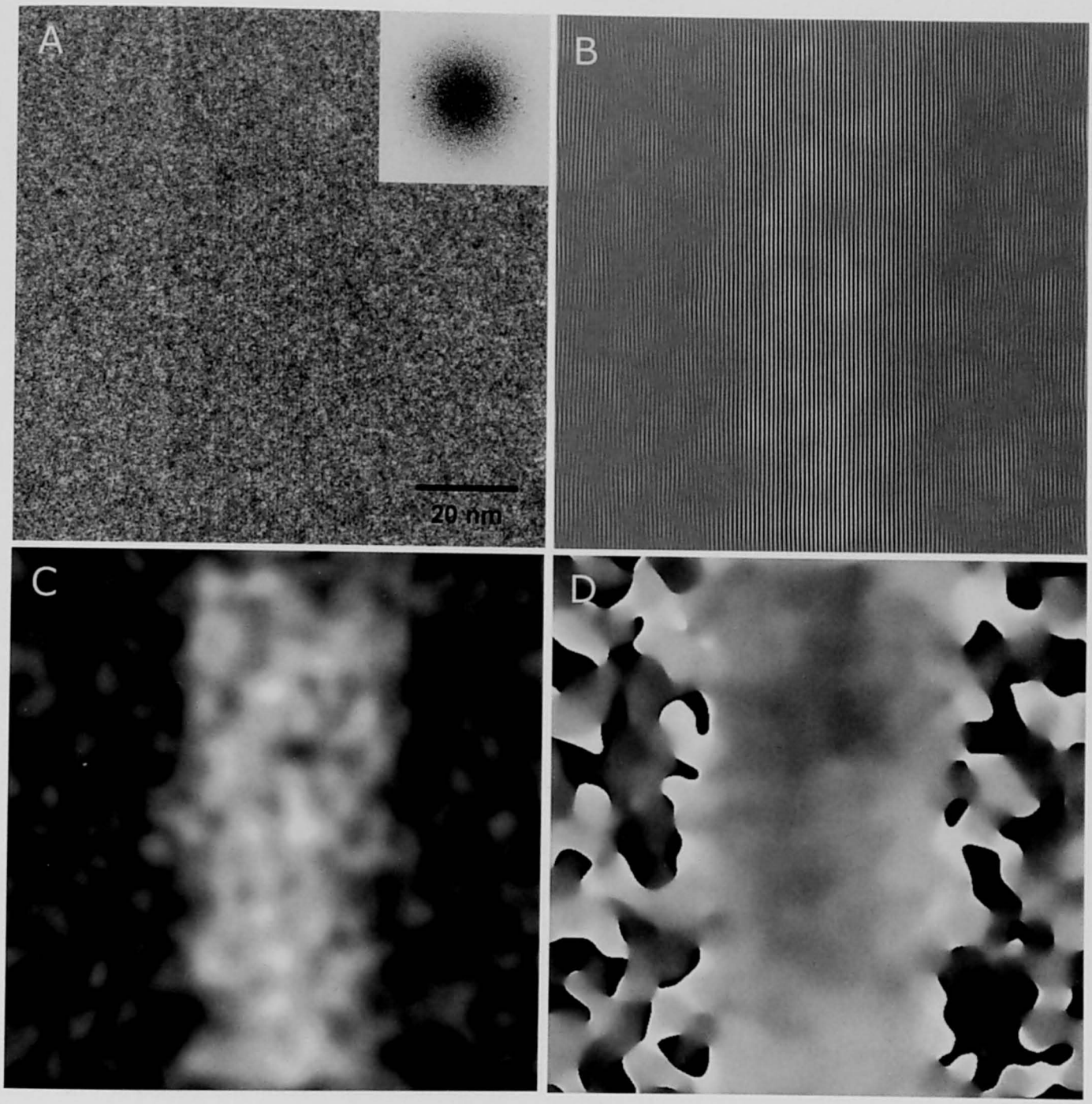

Figure 2-3. A longitudinal lattice image of $(010)_t$ planes obtained from I_α-rich *Cladophora* cellulose (A), and the corresponding Bragg-filtered (B), amplitude (C), and phase (D) images. Inset in A is the corresponding PS.

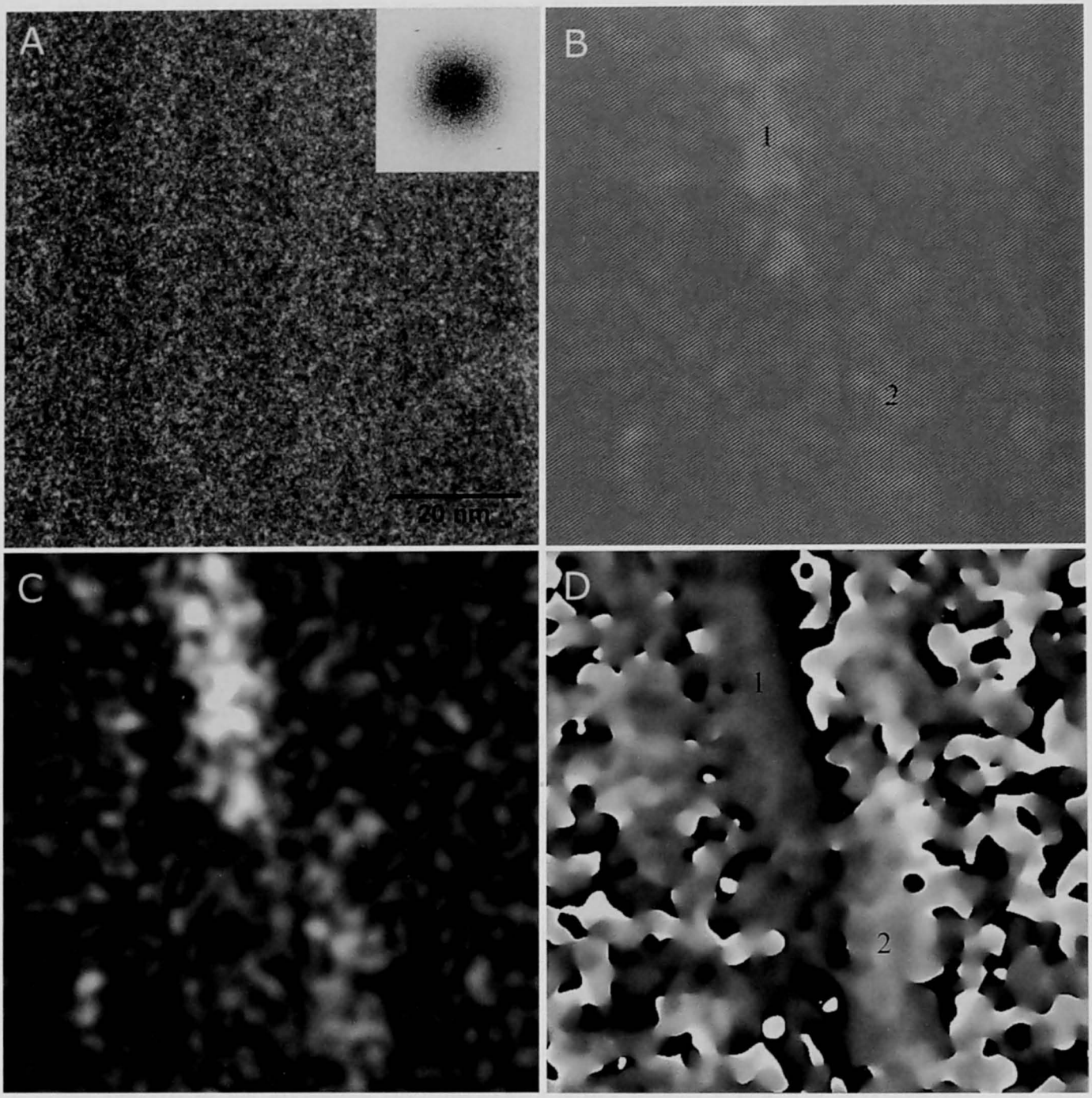

Figure 2-4. A longitudinal lattice image of $(\bar{1}\,\bar{1}\,2)_t$ planes obtained from I_α-rich *Cladophora* cellulose (A), and the corresponding Bragg-filtered (B), amplitude (C), and phase (D) images. Inset in A is the corresponding PS. In C and D, there seems to be two domains (numbered by 1 and 2), between which the phase is differentiated by about π.

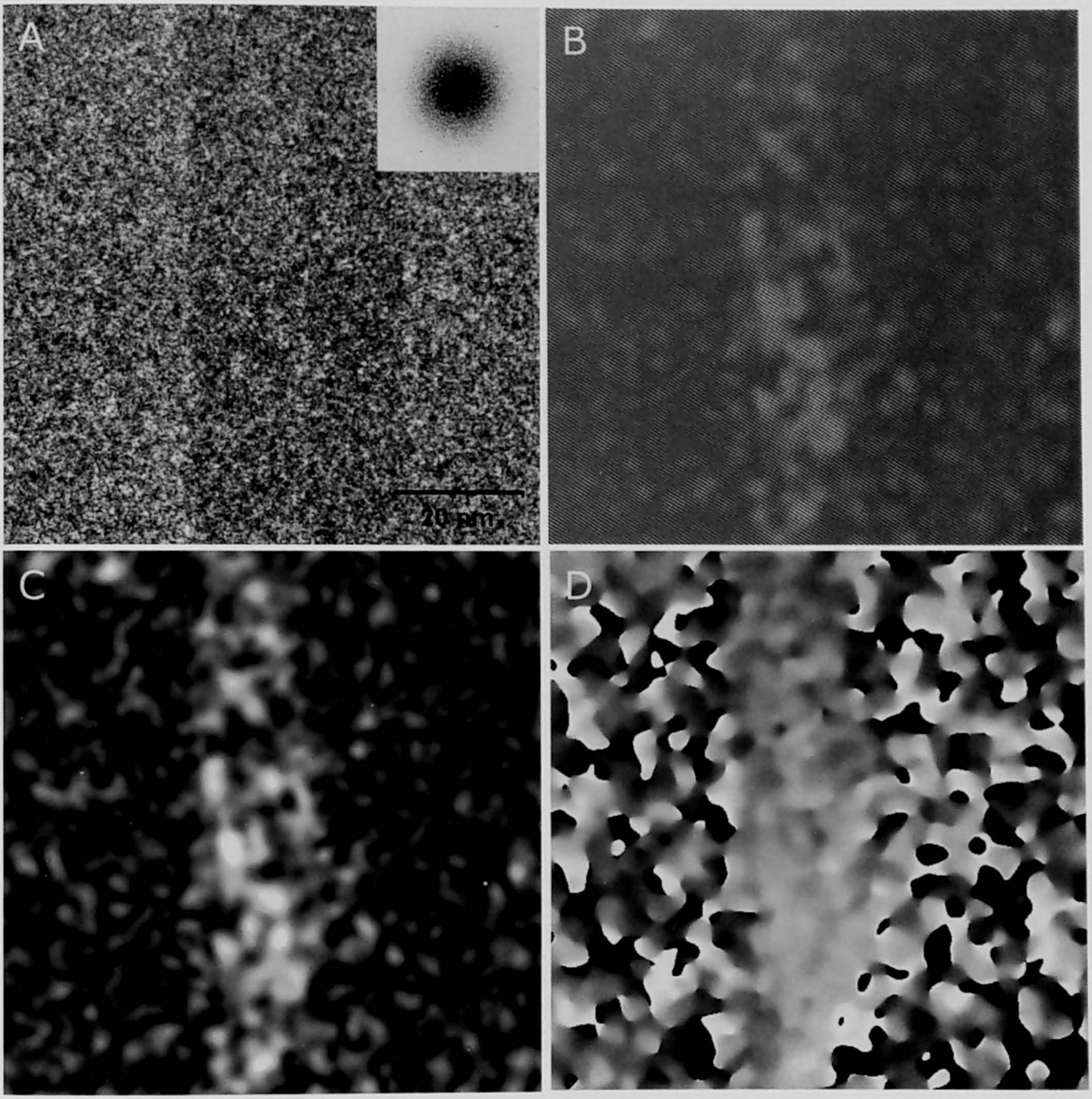

Figure 2-5. A longitudinal lattice image of $(102)_m$ (in the same projection as in Figure 2-5) planes obtained from annealed I_β-rich *Cladophora* cellulose (A), and the corresponding Bragg-filtered (B), amplitude (C), and phase (D) images. Inset in A is the corresponding PS.

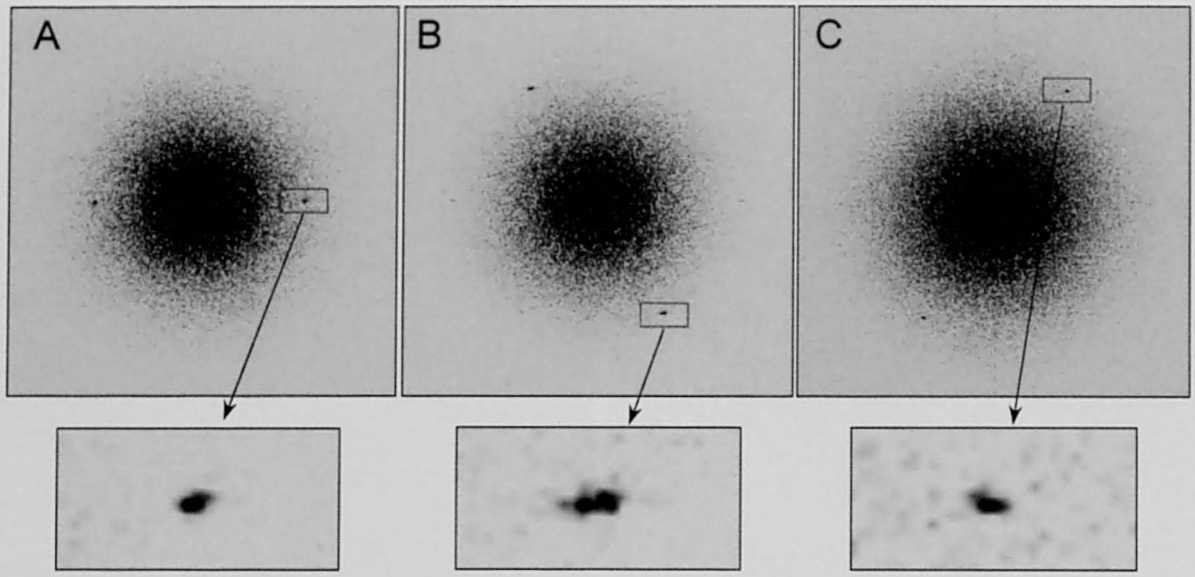

Figure 2-6. Power spectra of lattice images. **A**: $(010)_t$ spots from I_α-rich *Cladophora* cellulose. **B**: $(\bar{1}\,\bar{1}\,2)_t$ spots from I_α-rich *Cladophora* cellulose. **C**: $(102)_m$ spots from I_β-rich annealed *Cladophora* cellulose.

2.4 Abstracts

The geometric phase analysis has been applied to high resolution images from algal cellulose microcrystals. The pictures were decomposed into sub-images containing only the amplitude and phase information. Compared with annealed monoclinic I_β-rich microfibrils, initial triclinic I_α-rich cellulose was found to be more heterogeneous when viewed along its (110) triclinic lattice planes (H-bonding sheets). As a microfibril twist and radiation damage could not be totally ruled out as having an effect on the lattice image, this result has to be considered with care when used in order to survey the distribution of different phases in a cellulose microfibril. However, the phase analysis of noisy low dose high resolution images appeared as a promising new method to investigate polymer crystals and the distribution of domains of different structure or containing lattice distortions.

3. Preferential Hydrolysis of Cellulose Microfibril by a Processive Type Cellulase, Cel7A

3.1 Introduction

The cellobiohydrolases, Cel7A and Cel6A (previously CBHI and CBHII, respectively) [Henrissat *et al.* 1998] are major cellulases produced by fungi *Trichoderma* sp. and responsible for crystalline cellulose degradation. Traditionally, they have been long thought to liberate cellobiose moieties from the non-reducing ends of cellulose chains [Teeri 1997]. However, the recent biochemical analyses using soluble oligosaccharide model compounds labeled at one end by ^{3}H [Veršanská & Biely 1992, Claeyssens *et al.* 1989] or ^{18}O [Barr *et al.* 1996] demonstrated that Cel7A attacked at the reducing ends while Cel6A acted from the non-reducing ends of the corresponding oligosaccharides. Both enzymes are now thought to be processive enzymes [Rouvinen *et al.* 1990, Divne *et al.* 1994, Davies & Henrissat 1995], catalyzing cleavage of several consecutive bonds without dissociating from the substrate. Their 3-D structures in complex with various substrate analogues and ligands also demonstrated confirmatively the above mentioned directional binding of the substrate [Rouvinen *et al.* 1990, Divne *et al.* 1998].

Regarding the insoluble crystalline substrate, *i.e.* native cellulose microfibril, the directionality of degradation has been less studied. Only electron microscopic investigation of Cel6A degradation on highly crystalline *Valonia* cellulose microcrystals [Chanzy & Henrissat 1985] proved unidirectional mode of action, showing the formation of a pointed tip at the non-reducing end of a microcrystal. The result was confirmed when the reducing end staining technique [Kuga & Brown 1988] was applied to analyze the pointed microcrystals, where the silver labeling was only found opposite to the pointed end [Koyama *et al.* 1997b].

Degradation by Cel7A on the same *Valonia* microcrystals yielded narrower and subfibrillated crystalline elements [Chanzy *et al.* 1983], but no clear sign was found to indicate its directional mode of action. Recently, however, the experimental condition to yield polar microcrystals has been found [Imai *et al.* 1998], from which one can deduce the directionality of Cel7A action on crystalline substrate. On the basis of the "parallel-up" packing of cellulose crystals, Koyama *et al.* [1997b] have established the method to determine the directionality of cellulose chains in a given microfibril by simple crystallographic consideration. Applying this technique to the pointed microcrystals after hydrolysis, the mode of action of Cel7A on *crystalline* substrate was analyzed with special attention to the molecular and crystallographic directionality.

3.2 Materials and Methods

Preparation of microcrystalline suspension of *Valonia*

The vesicles of *Valonia ventricosa* were purified by conventional acid-alkali treatments [see 1.2]. Purified cell walls were cut into small pieces and mechanically disintegrated by homogenization for 10min at 10,000rpm. They were then hydrolyzed for 5h in boiling 3.5N HCl under reflux and continuous strong stirring. The resultant microcrystalline suspension was neutralized by several centrifugal washes with distilled water until achieving neutrality and stored at 4°C in distilled water containing 0.01% NaN_3.

Enzymatic degradation by CBH Cel7A

The cellobiohydrolase Cel7A (CBHI) was purified from Meicelase, a *Trichoderma viride* cellulase mixture (Meiji-Seika, Tokyo, Japan) according to the procedure by Samejima *et al.* [1998]. The hydrolysis was carried out as follows: 8ml of a 0.5 mg/ml of cellulose suspension was incubated at 40°C in 0.1M sodium acetate buffer (pH 4.2), containing 1.44mg of Cel7A 144μg of β-D-glucosidase from Almonds (EC 3.2.1.21, Sigma) was also added to the reaction in order to avoid the inhibition of Cel7A by the cellobiose produced during hydrolysis. The reaction solution was centrifuged and stopped by washing with 0.2% NaOH. The resulting degraded microcrystals were washed thoroughly by several centrifugations with distilled water and stored at 4°C.

Silver labeling of reducing ends

Cel7A degraded *Valonia* cellulose microcrystals were stained by the protocol of Kuga & Brown [1988]. The suspension of cellulose microcrystals (1ml) was mixed with 5ml of 1% thiosemicarbazide (TSC) in aqueous 5% acetic acid. After static incubation at 65°C for 90min, the suspension was washed by centrifugation. The sample was resuspended in 1 ml of water and mixed with 5 ml of 2% sodium borate with 1% silver protein (SP) (Merck). This mixture was kept in the dark at room temperature for 1h and washed by centrifugation. The final enhancement of the electron density of the TSC-SP treated reducing ends was done by mixing 1ml of sample with 5ml of silver ammonia solution in a nitric acid-cleaned glass vial for 6-9min at 95°C until the sample turned brownish. The silver ammonia solution was prepared by adding ammonia solution to a 13.3% silver nitrate solution until the initial brownish color became clear.

Transmission Electron Microscopy

All the micrographs and diffraction diagrams were taken with a JEM-2000EX II operated at 100kV and recorded on Mitsubishi MEM films. Diffraction contrast imaging in the bright field mode was used to visualize the sample without further contrast enhancement. The images were taken at 1,000-6,000x under low dose exposure with the use of the MDS.

The diffraction diagrams were obtained by microdiffraction mode. The detailed procedures are described in 1.2. In the experiments with tilting, it was rotated to align the fiber axis to the tilt axis by using the rotation-tilt holder (SRH holder, JEOL) when a microcrystal was found. Diffraction patterns were then recorded from the nearest portion of the microcrystal with the precise tilt angles about microcrystal length; the angles were differently set at a series of -40°, 0° and 40°, or of –17°, 0° and 17°, depending on the purposes as described in the text, Figure 3-2 and 3-6.

3.3 Results and Discussion

Molecular directionality in degradation pattern of microcrystals

Initial *Valonia* microcrystals display uniform and well-defined microfibrillar shape. The lateral dimensions are *ca.* 20 x 20 nm^2 [Revol 1982, Sugiyama *et al.* 1985b] and the lengths are in the range of several hundreds nanometers to a few micrometers. The appearance of the ends of microcrystals is oblique in most cases. This terminal angle is generally higher than 40° with the longer axis of microcrystals.

Most of the initially smooth and well-defined *Valonia* microcrystals displayed fibrillation as reported previously [Chanzy *et al.* 1983]. However the hydrolysis reaction was rather heterogeneous so that some microcrystals remained superficially intact. Typical appearance of microcrystals after 7 days of incubation with Cel7A was shown in Figure 3-1A. Those crystals were as wide as 10-20nm, but shorter in length than initial crystals. Remarkably the crystals displayed polar morphology and this phenomenon was most emphasized when the crystals were subjected to mild treatment (without stirring) for longer duration.

The tip of such microcrystals was narrower at one end, and frequently kinked as indicated by arrowheads in Figure 3-1A, probably induced by mechanical forces during treatment such as centrifugal washing. This is exemplified in an enlarged micrograph in Figure 3-1B, showing small kinked fragments in the upper part of a microcrystal. This observation substantiated that the mode of action of Cel7A was unidirectional.

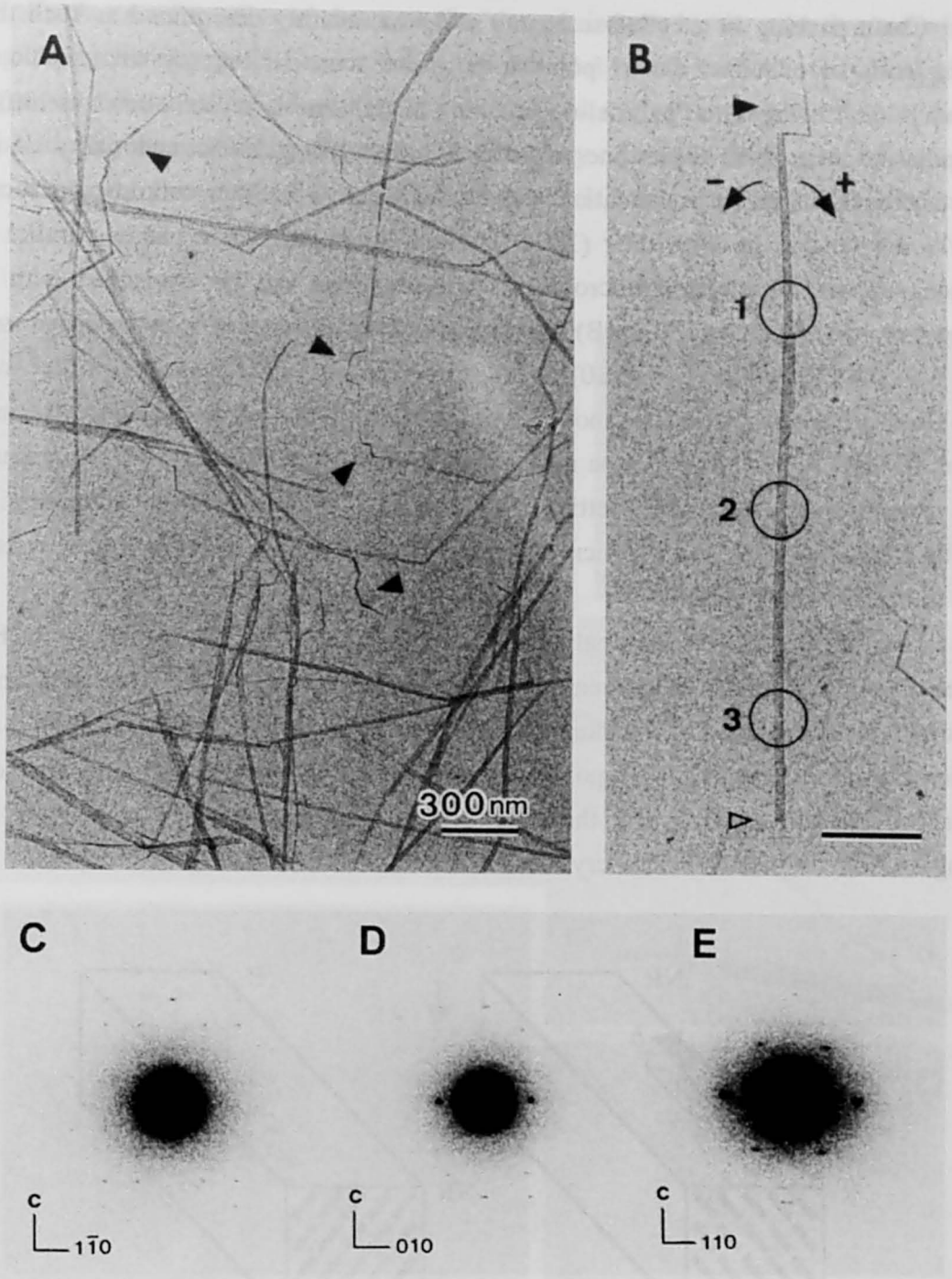

Figure 3-1. A bright-field diffraction contrast electron micrograph of *Valonia* cellulose microcrystals after enzymatic degradation for 7 days. Note that the only one ends of microcrystals are narrowed and such parts are in most cases kinked by mechanical agitation as indicated by arrowheads (A). Enlarged micrograph of an isolated microcrystal, showing narrowed end on top (B). Each circle indicates the position for diffraction diagram. The diagrams (C) to (E) are taken from positions 1 to 3 in (B) with the corresponding tilt angles of -40°, 0° and 40°. Solid and open arrowheads in (B) indicate the reducing and non-reducing ends of the crystal respectively. Scale bar 300nm.

Chain packing in a cellulose I_α unit cell was recently determined as such that the reducing ends of cellulose chains pointed the same sense to the crystallographic *c*-axis [Koyama *et al.* 1997b]. This "parallel-up" packing in cellulose I_α crystal allows identifing the chain polarity in a given crystalline microfibril by analyzing the directionality of *c*-axis. Theoretical background was schematically shown in Figure 3-2. Since cellulose microcrystals from *Valonia* tend to lie with their $(100)_t$ 0.61-nm equatorial lattice planes parallel to the specimen support for electron microscopy, two situations can be envisaged with *c*-axis pointing toward (A) or away from (B) the observer. Clear difference in between two settings A and B is the directionality of $(110)_t$, 0.39-nm equatorial lattice planes. In order to bring these planes in Bragg condition, in another word, to orient these planes parallel to the incident electron beams, one has to rotate the microcrystals by -40° and 40° respectively about their longer axes in the corresponding settings in A and B. This feature allows determining the *c*-axis by obtaining three sets of microdiffraction diagrams from a given microcrystal with precise tilting at -40°, 0° and 40°

The tilt-microdiffraction analyses for a polar microcrystal as in Figure 3-1B were performed, and 15 over 15 experiments gave the identical result as in Figure 3-1C to 3-1E. These diagrams correspond to the situation of Figure 3-2B, which implies that the *c*-axis of the microcrystal in Figure 3-1B points upward. Accordingly the reducing end of this microcrystal points upward, and thus the kinked narrowed part is concluded to the reducing-end-side of cellulose microcrystal.

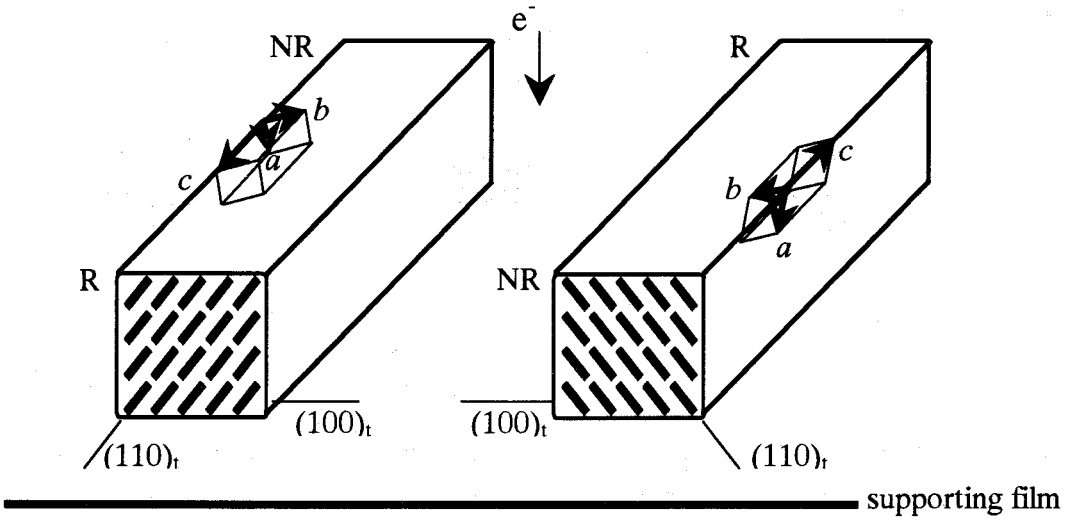

Figure 3-2. Theoretical background to determine the molecular polarity of a cellulose microcrystal. Two types of microcrystals having opposite *c*-axis directionality lie on the film support with their 0.61 nm (100) lattice planes paralleled to it. Microcrystal having *c*-axis toward the observer (A) gives 0.39 nm (110) diffraction spots after anticlockwise rotation by 40° about the longer axis, while that in B gives the same diagram after clockwise rotation by 40°.

Further confirmation of above results was carried out by the selective reducing end staining technique [Kuga & Brown 1988]. Figures 3-3A and 3-3B show typical electron micrographs of the resulting microcrystals with one end eroded to a pointed tip and the same end labeled with silver staining. Though it was not very often, the sharp wedged degradation pattern across the microcrystal width as in Figure 3-3C was observed. The image shows

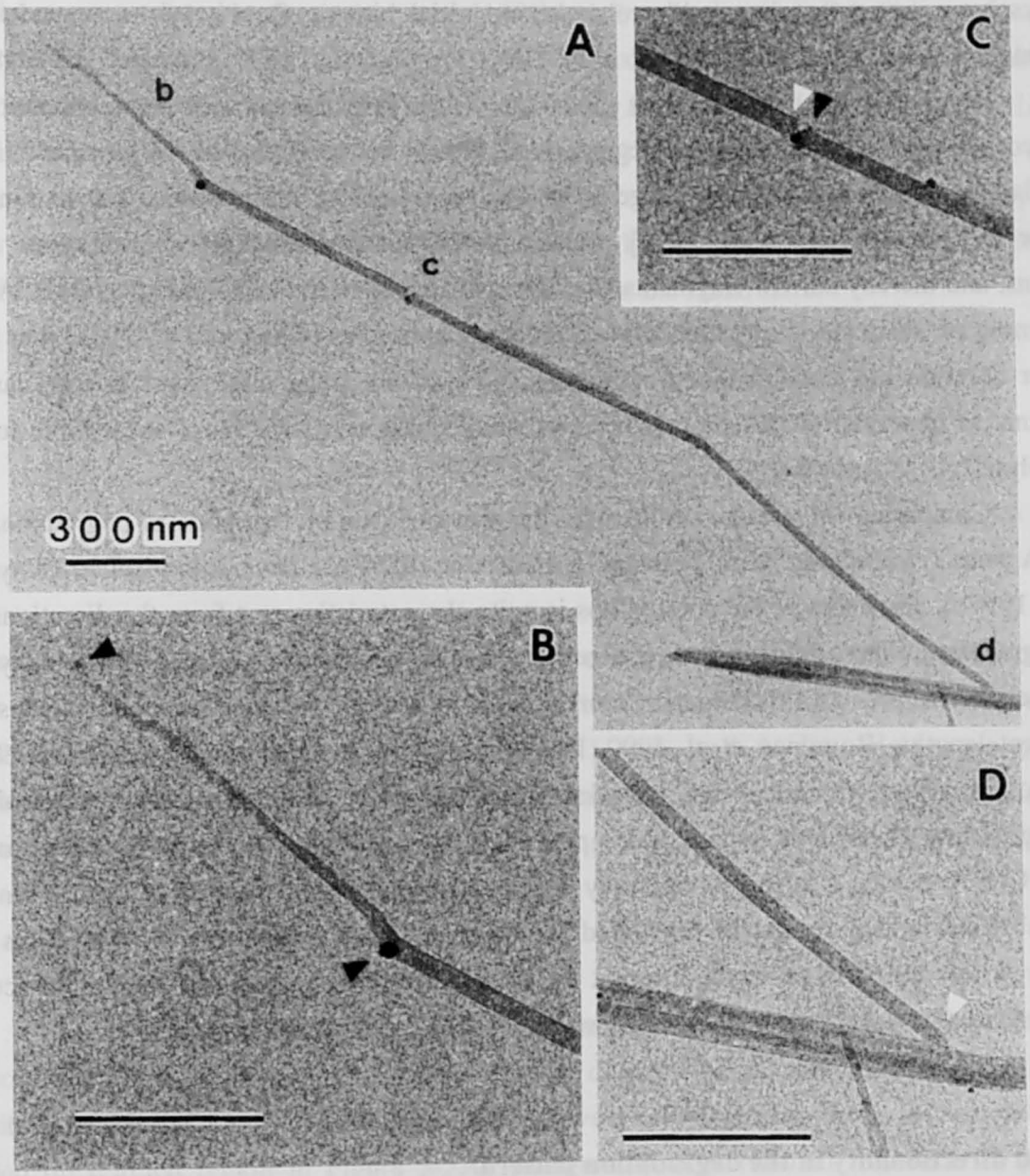

Figure 3-3. Electron micrographs of a reducing-end silver-stained *Valonia* cellulose microcrystal after enzymatic degradation for 7 days (A). Three areas marked as b to d are enlarged in B to D. **B**: narrowed end with labeling (solid arrowheads), **C**: internal wedged-shaped cut with one side labeled (solid arrowhead) and the other side unlabeled (open arrowhead), **D**: unlabeled end (open arrowhead) indicating non-reducing end side. Scale bar 300nm.

unambiguously that the reducing end staining technique is extremely specific to the reducing end of the chain, and implies that there must have been endo-type degradation during this experiment. Concerning the latter implication, it is still necessary to verify the experimental conditions such as purity of Cel7A enzyme used here, and also to scrutinize if such structure had been created during initial acid hydrolysis to prepare microcrystals or not. However it is of great interest as it is potent to answer the debate whether Cel7A is a true exo-processive enzyme that definitely needs chain-ends to initiate degradation [Srisodsuk *et al.* 1998] or a processive enzyme that is capable to make an initial bite on the crystal as an endo-type enzyme [Samejima *et al.* 1998, Amano *et al.* 1996, Armond *et al.* 1997, Boisset *et al.* 1998].

Regarding the heterogeneous appearance of the hydrolysates, one may explain it also as a consequence of unidirectional degradation from the reducing end of a crystal, creating a fibrillated microcrystal. Since the large active-site tunnel of Cel7A should allow strict binding to the substrate [Divne *et al.* 1994], weak agitation may be enough to disintegrate such regions, and thereby narrow fragments would be isolated from the initial microcrystals. At the beginning of treatment, many fibrillated fragments can be seen [Chanzy *et al.* 1983], but after longer duration the reaction leaves non-destroyed portions, polar microcrystals with narrow remains, as observed in this chapter because smaller fragments are more susceptible to the hydrolysis.

Comparing the present results with the previous data on the mode of degradation by Cel6A from *Trichoderma reesei* [Chanzy & Henrissat 1985] and *Humicola insolens* [Koyama *et al.* 1997b], sharpness of the pointed tips is quite characteristic apart from the directionality of degradation. The origin of such difference must arise from the structure of the enzymes themselves. In fact, both Cel7A and Cel6A are known to have tunnel-shaped active sites but different lengths [Rouvinen *et al.* 1990, Divne *et al.* 1994]. As discussed by Teeri [1997], Cel6A with a shorter tunnel, might occasionally fall off the substrate and reinitiate hydrolysis at neighboring chain ends, which yields pointed tip at one end of the crystal. On the other hand, Cel7A, having a longer tunnel, may hold a chain more tightly and keep itself bound to the substrate, which results in fibrillated crystals, *i.e.* much longer pointed tip. Thus the observed tip morphology from different enzymes may directly indicate the difference in *processivity* that are regulated by the 3-D structure of these important enzymes.

Lateral directionality in the degradation pattern

Careful observation of the eroded tip revealed that the side of a microcrystal was unidirectionally eroded after Cel7A degradation, while the remained part looked intact in width (Figure 3-1B, 3-5A). The tighter holding of the substrate by Cel7A may print some apparent indications about the microcrystal structure on it after the degradation, and thus the polar erosion by Cel7A was studied primarily in terms of the microfibril structure.

One of the possible explanations for this phenomenon may rely on the allomorphism

in *Valonia* cellulose. Using IR spectroscopy together with d-spacings analysis, it was found that I_α portion in algal cellulose is preferentially degraded at the first stage of the degradation by crude cellulase [Hayashi *et al.* 1997]. The degraded region in a microfibril is supposed to be I_α-rich. Microscopic observation in their report also showed that I_β-rich cellulose microcrystals from tunic were fibrillated into narrow fragments whereas *Valonia* microcrystals were shortened without narrowing in width by degradation. Thus, it was concluded that I_α region exists alternately with I_β region along the microcrystal in algal cellulose, as postulated by Sugiyama *et al.* [1991b] at first. In the case of Cel7A, as shown in Figure 3-5A, the unidirectional erosion in lateral side occurred together with the shortening of microcrystal, suggesting the complex distribution of I_α and I_β as shown in Figure 3-4. In the recent study with AFM [Baker *et al.* 1997], however, the triclinicity of the molecular array was extensively observed on surface of a *Valonia* microcrystal although monoclinicity was never seen. This suggested that the surface region of a *Valonia* microcrystal was occupied by I_α. The remained part might be covered by thin I_α layer in the initial state.

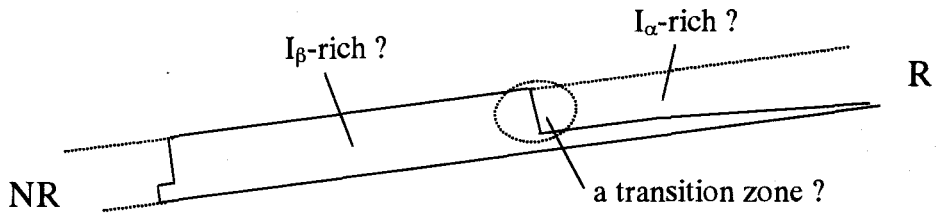

Figure 3-4. The hypothetical representation of the morphology of a *Valonia* microcrystal after Cel7A degradation, based on the localization pattern of I_α/I_β in it. This model basically shows the alternate distribution of I_α-rich and I_β-rich region along the microcrystal. However, a narrow I_β-rich region might be accompanied with the I_α-rich region sometimes, as shown above. (R: reducing end side, NR: non-reducing end side)

The remained part after Cel7A degradation was scrutinized by electron microdiffraction to study the relationship between degradation of microcrystalline cellulose and its crystal structure. The diffraction diagrams were recorded from the basal region of the eroded tip (circled region in Figure 3-5A). Intriguingly, a meridional reflection of $(002)_m$ specific to I_β [Sugiyama *et al.* 1991b] was observed more frequently than the initial microcrystal (Figure 3-5B), meaning that monoclinicity in the degraded microcrystal became more evident than the initial. Consistent with the previous data [Hayashi *et al.* 1997], thus, it was confirmed that I_α is more susceptible to the degradation by Cel7A.

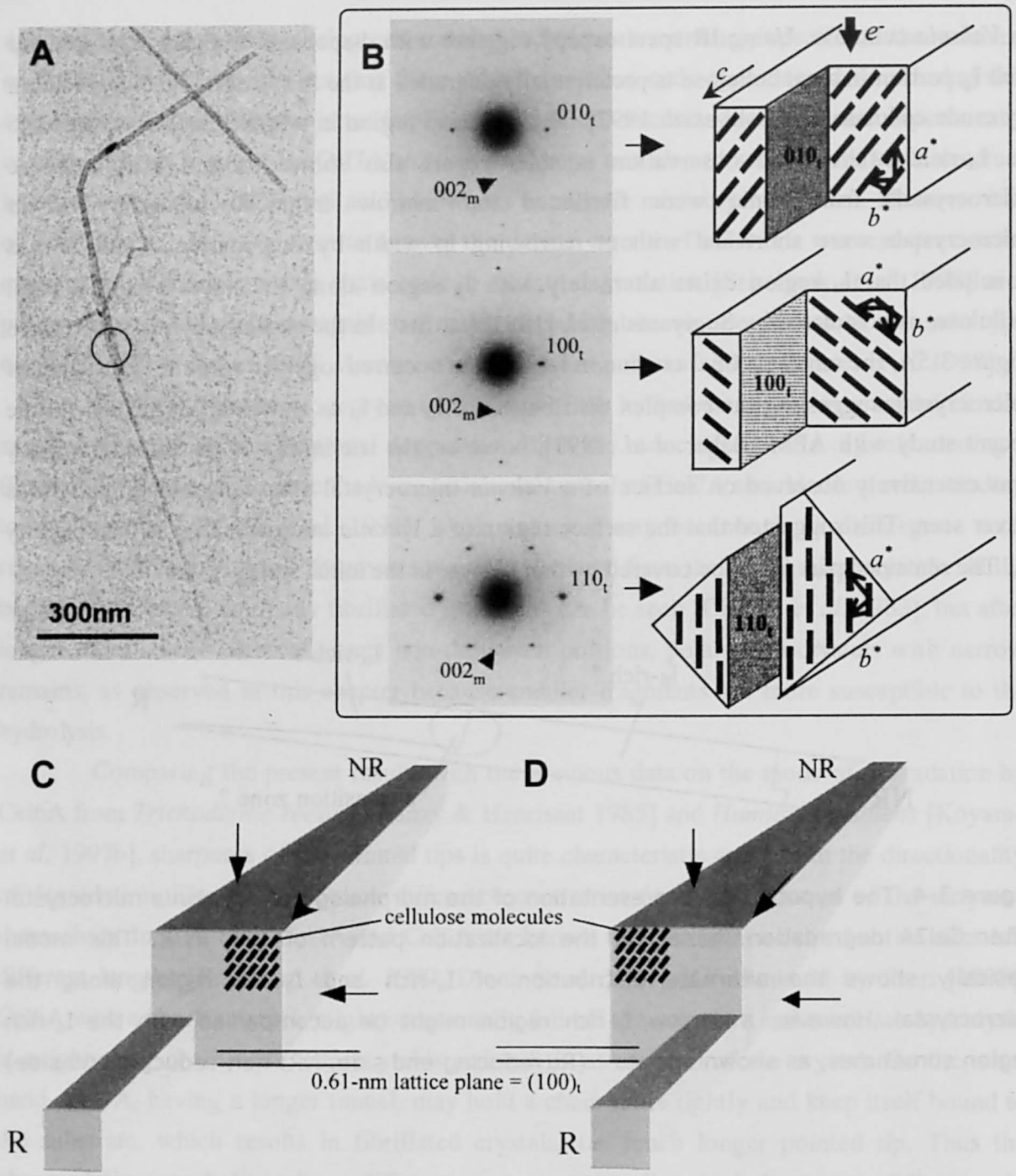

Figure 3-5. Electron microdiffraction diagrams (B) of the degraded microcrystals by Cel7A, which were obtained from the region circled in A. Reflection of $(002)_m$ specific to I_β was frequently observed in the resultant microcrystals. Patterns in three projections were obtained, implying that the unidirectional erosion in the lateral is apparent when viewing in the corresponding projections, as shown in B. The degradation pattern shown in C cannot explain the unidirectional erosion when viewing along the $(110)_t$ equatorial lattice plane (*i.e.* along the arrowhead). On the other hand, the model in D is consistent with the diffraction result: the erosion will look laterally unidirectional in the corresponding projections to B (when viewing along the arrows).

Noticeably, in Figure 3-5B, the remained part of the degraded microcrystal frequently provided $(100)_t$ and $(110)_t$ equatorial reflections, in addition to $(010)_t$ reflection which appeared preferentially in electron diffraction because of the uniplanar orientation of 0.61-nm lattice plane. Obviously, the degradation by Cel7A impaired the preferential planar orientation behavior. This result offers more interesting suggestion by following discussion. Diffraction by electron occurs when the incident beam passes almost parallel to a lattice plane (2θ is quite close to 0° because of short wavelength of electron), and thus it is deduced that the equatorial lattice giving diffraction in Figure 3-5B was the plane along which the side of a microcrystal was eroded as shown in Figure 3-5A. Accordingly, the erosion was likely to occur along the lattice planes of $(100)_t$, $(010)_t$ and $(110)_t$, as shown in the cartoons in Figure 3-5B. In other words, the unidirectional erosion in a microcrystal is apparent when viewing along each lattice plane of $(100)_t$, $(010)_t$ and $(110)_t$. In order to explain this geometry, two possibilities shown in Figure 3-5C and D were compared. In the former, the erosion of the tip dose not look unidirectional when viewing along the 0.39-nm lattice plane (when viewing along the arrowhead in C), which is inconsistent with the diffraction data. On the contrary, the latter model agrees well with the data in Figure 3-5B. The probable model in Figure 3-5D shows that the erosion of cellulose microcrystal by Cel7A progresses from the corner where the pyranose rings of a glucan chain are not buried inward, but exposed outward.

Assuming that cellulose I_α was degraded to produce the erosion pattern in Figure 3-5D, the erosion directionality is attributed to the I_α unit cell orientation by two ways (the top cartoons in Figure 3-6). The erosion goes toward which sides of the b^*(or a^*)-axis of the I_α triclinic unit cell which has no rotational symmetry. The previous IR data [Hayashi *et al.* 1997] showed that the degraded microcrystals by Cel7A still comprise I_α portion to some extent. This fact will allow the crystallographic analysis based on the I_α structure to determine the b^*-axis in a side-eroded microcrystal. On the basis of the preferential orientation of 0.61-nm lattice plane, tilting by –17° will provide the triclinic diffraction pattern in $[311]_t$ projection. This pattern can be inversed distinguishably depending on the directionality of the b^*-axis, by which one of the two models (I or II in Figure 3-6) will be preferred. The difference between these models is plainly described in the bottom cartoons in Figure 3-6. When the molecules are peeled off from the microcrystal, the H-bonding sheet that subsequently appears is translated by $-c/4$ (model I) or $+c/4$ (model II). Thus, the mode of Cel7A action possibly has a preference for the substrate crystallographic directionality, as well as the molecular directionality. Although over 40 sets of the diffraction patterns were obtained from the eroded microcrystals in fact, the reliable data has not been obtained yet, because of the distortion of the uniplanar orientation and less amount of I_α to provide the diffraction. More accumulation of the data may be necessary for elucidation of this problem including negative conclusion.

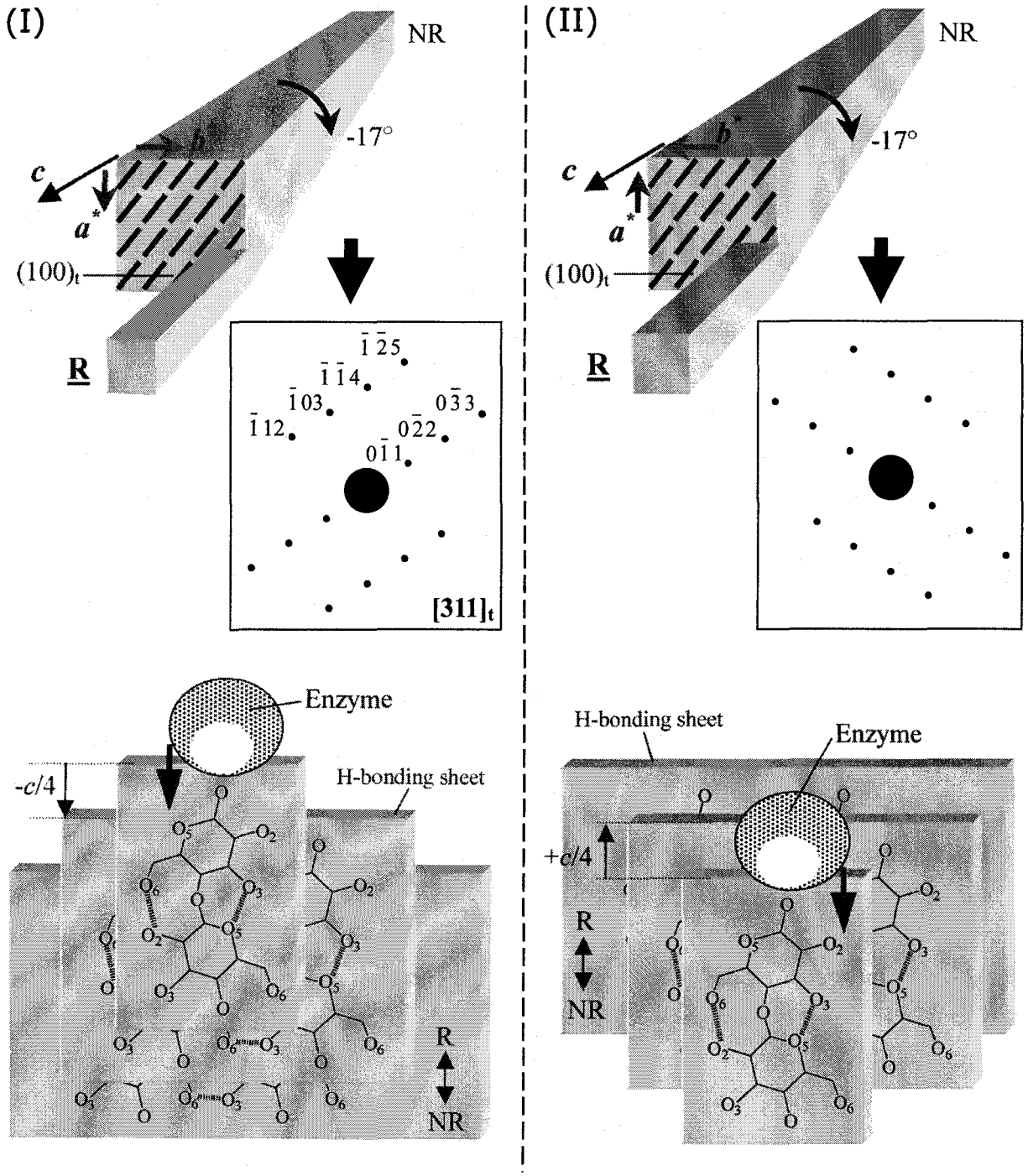

Figure 3-6. Two possibilities of I_α unit cell orientation in the side-eroded microcrystal shown in Figure 3-5D. Assuming the uniplanar orientation of $(100)_t$ in a *Valonia* microcrystal, tilting a microcrystal by -17° around the fiber axis allows to obtain the asymmetric diffraction pattern in the $[311]_t$ projection. Depending on the directionality of b^*-axis, *i.e.* the unit cell orientation, two patterns that are mirrored each other will be distinguished (cartoons in the top). Thus it is possible to determine which model (I) or (II) is correct, by translation of the H-bonding sheet newly appeared after peeling off the molecules from the outside of a microcrysta, $-c/4$ in (I), and $+c/4$ in (II)

Electron microscopy projected the three-dimensionally eroded tip onto 2-D observation. Then if there is a directional preference in the degradation as suggested above, the appearance of the tip suffered from Cel7A also should vary with the projections, and it will be possible to reconstruct the 3-D morphology from them. The data in this chapter – electron microscopy with tilting stage and shadowing – did not support it, which implies the model shown in Figure 3-5C is too simple. More dedicated investigation will be necessary for the elucidation of the degradation pattern.

3.4 Abstracts

On the basis of the 'parallel-up' structure of the cellulose crystal, a crystallographic approach to study the mode of action of cellobiohydrolase Cel7A on *Valonia* cellulose microcrystal has been carried out. After incubation with Cel7A, most of the initially smooth and well-defined *Valonia* microcrystals displayed fibrillation. However, as the hydrolysis reaction was rather heterogeneous, some microcrystals remained superficially intact. Close investigation on such crystals revealed polar morphology: one end was narrowed extremely or pointed. Electron microdiffraction analysis of these crystals evidenced that the narrowing of the microcrystals occurs at their reducing end side. This was also confirmed by the visualization of selective reducing end labeling at the pointed ends of microcrystals. These lines of investigation are the first demonstration that the processivity of Cel7A action against insoluble highly crystalline celluloses is unambiguously toward non-reducing ends from reducing ends. Unidirectional erosion of a microcrystal occurs also in lateral, universally after Cel7A degradation. It is suggested that the erosion progresses from the corner that exposed pyranose ring planes of glucan chains. This one-side erosion of a microcrystal might be attributed to the crystallographic directionality of cellulose I_{α}.

4. Almost Pure I_α Cellulose Found in Cell Wall of a Gray Alga, *Glaucocystis*

4.1 Introduction

The ellipsoidal unicellular fresh water algae *Glaucocystis* (Glaucophyta) and *Oocystis* (Chlorophyta) are two distinct examples of how nature has evolved different ways to achieve similar types of cell wall architecture. Since they were suitable for freeze-fracture experiments when studies into cellulose synthesizing complexes began, the ultrastructural features of their cell walls and membrane structure have been extensively investigated [Robinson & Preston 1971, Brown & Montezinos 1976, Willison & Brown 1978a, Willison & Brown 1978b].

Their cell walls are superficially similar in that they are comprised of several lamellae, each consisting of a parallel arrangement of cellulose microfibrils with a rectangular cross-sectional shape. Microfibrils in each layer lie helically to the longer axis of the cell, and the fibrillar angle alternates by 90° from left to right between adjacent lamellae. These microfibrils are considered to be synthesized by linear-type terminal complexes (TCs) which travel in the plasma membrane. Interestingly, the directionality of TC movement during the formation of the cell wall is different in these two algae. During the formation of lamellae in *Glaucocystis*, all TCs move in one direction [Willison & Brown 1978b], whereas those in *Oocystis* travel in opposite directions [Brown & Montezinos 1976] as was later demonstrated to occur in the other alga *Valonia* [Itoh & Brown 1984]. Such bidirectionality of synthesis in *Valonia* was supported by the existence of two types of microfibrils in a given lamella with their crystallographic *c*-axes in the opposite direction to each other [Revol & Goring 1983, Sugiyama *et al.* 1985b].

The structure of the plasma membrane of *Glaucocystis* is unusual: the membrane is not smooth but is highly convoluted and indented [Echlin 1967]. Robinson & Preston [1971] suggested that this roughness was due to the existence of an additional space, which they named the "shield-shaped structure" between the plasma membrane and the cell wall. This shield was found to not actually cover the complete surface of the cell but to be localized in the shape of a flattened sac underlying the plasma membrane. This unique structure exists only in *Glaucocystis* [Willison & Brown 1978b].

Despite intensive cytological and ultrastructural analyses of their cell walls, little is known about the crystallography of these algae. *Glaucocystis* cellulose was shown to be I_α-rich in a previous FT-IR study [Sugiyama *et al.* 1991a], but no further quantitative analysis has been performed. In this chapter, therefore, the author performed crystallographic analyses with particular reference to the I_α/I_β allomorphism [Atalla & VanderHart 1984, Sugiyama *et al.*

1991a & 1991b, Yamamoto & Horii 1993] and the uniplanar orientation behavior, in which algae display considerable phenotypic variations [Koyama *et al.* 1997a].

4.2 Materials and Methods

Cellulose sources

Glaucocystis nostochinearum (Glaucophyta, Glaucophyceae, Glaucocystales,) was obtained from Molecular Cell Biology Research Institute, the University of Tokyo, Japan. *Oocystis apiculata* (Chlorophyta, Chlorophyceae, Chlorococcales) was a gift from Prof. R. M. Brown, Jr., University of Texas at Austin, TX, USA. Both algae were grown in Modified Kantz medium [Kantz & Bold 1969] at 25°C under day- and night-time for 16 h and 8h respectively. For comparison, *Cladophora* sp. and *Valonia ventricosa* (Chlorophyta, Siphonocladales) were used as I_α-rich type cellulose specimens. Another type of cellulose, I_β-dominant type, was also investigated. They were hydrothermally annealed *Valonia* cellulose [Yamamoto *et al.* 1989] and intact tunicate cellulose from *Halocynthia roretzi* (Chordata, Urochordata, Ascidiacea) [Belton *et al.* 1989, Larsson *et al.* 1995]. The latter three specimens were the same ones that were used in Chapter 1.

Purification and preparation of microcrystalline suspension

The cell walls and tunic from the above specimens were purified by alkali and acid treatment after ethanol extraction. To prepare microcrystalline suspensions, the samples were hydrolyzed either by boiling in 2.5N HCl for 12h or treatment in 40% H_2SO_4 at 70°C for 2 days with continuous stirring. The resulting suspension was neutralized by centrifugal washings with distilled water and then dialyzed against distilled water for at least 12h.

X-ray diffractometry

Samples of 100mg of the freeze-dried purified cell walls were pressed into tablets under 20MPa. X-ray diffractometry was carried out in reflection mode (2θ = 5°-40°) using a Rigaku RAD-1 with CuK_α radiation generated at 35kV and 20mA. The diffraction profile obtained was processed by computer-aided fitting analysis and transformed to basic crystallographic features: d-spacings of equatorial lattice planes and crystal size.

CP/MAS ^{13}C NMR spectroscopy

The tablets prepared for X-ray experiments were mechanically disintegrated into smaller fragments, which after full hydration were packed into a MAS rotor with an O-ring seal. CP/MAS ^{13}C NMR measurements were performed with a JNM-GSX 400 (JEOL Co.,

Japan) spectrometer under a static magnetic field of 9.4T. ^{1}H and ^{13}C radio-frequency field strengths ($\gamma B_1/2\pi$) were 4.2μs for both CP and dipolar decoupling processes. The MAS rate was set to 5.6 – 5.8kHz, and the contact time for the CP process was 1.0ms. The ^{13}C chemical shift relative to tetramethylsilane (Me_4Si) was calibrated by using the CH_3 carbon line at 17.36 ppm of hexamethylbenzene crystals as an external reference. Line shape analysis was carried out for C4 resonance using the least squares fitting algorithm and I_α fraction: f_α was calculated from the following equation [Yamamoto & Horii 1993],

$$f_\alpha = 0.5 + I_{90.3} - I_{88.6}$$

where I_x means the peak area at the corresponding ppm.

Fourier Transform Infra-Red spectroscopy

Thin transparent film was prepared by drying a few drops of each cell suspension for *Glaucocystis* and *Oocystis*. For *Valonia* and *Boergesenia*, the purified thin cell wall layers were directly measured. A JASCO FT-IR 7000 spectrometer was used to measure the absorbance as well as in Chapter 1. The f_α^{IR} was estimated from the equation described in 1.2, Chapter 1 [Imai & Sugiyama 1998]:

$$f_\alpha^{IR} = A_{750} / (A_{750} + kA_{710})$$

where A_x is the integrated absorption at the corresponding wave number and k is the constant (k=0.16).

Electron Microscopy

Ultrathin sectioning

The purified cells were embedded in the aqueous melamine-based resin Nanoplast (Agar Scientific, UK). The cells of *Glaucocystis* and *Oocystis* in water were centrifuged to collect as many cells as possible and deposited on pre-hardened resin in molds. After water had been almost evaporated, the mold was delicately filled with the resin and cured for 2 days at 40°C then for a further 2 days at 60°C. The hardened block was set on an Ultracut E (Reichert, Austria) equipped with a diamond knife (Diatome, U.S.A.) with a clearance angle of 4° to obtain ultrathin sections 70nm thick. Sections were then mounted on carbon-coated copper grids.

Diffraction contrast imaging in the bright field mode

A JEM-2000EX II operated at 100kV was used. The MDS was used for diffraction contrast imaging to eliminate specimen damage caused by electron irradiation. A 100μm objective aperture was inserted to eliminate all the diffracted beams from the crystalline areas, which enabled to visualize the objects as dark contrast in the positives. The images were recorded at 2,000-10,000x on Mitsubishi MEM films.

Electron diffraction

Two modes of electron diffraction were employed; namely, selected-area diffraction and microdiffraction. In the former, diffraction diagrams were recorded from an area 2 to 3μm in diameter, whereas in the latter they were obtained from an area with a diameter of 100nm. Microdiffraction was extensively used for the analysis of individual microcrystals. A cryoprotection technique using a liquid N_2 cold stage (Gatan Inc., USA) was also employed to extend the lifetime of crystals under irradiation. The microdiffraction procedure was described in detail in 1.2, Chapter 1.

4.3 Results and Discussion

There are several morphological similarities between the gray alga *Glaucocystis* and the green alga *Oocystis*: both have an ovoid mother cell of *ca.* 30-40μm, containing 4 to 8 daughter cells (autospores) (See Figure 4-1). Furthermore, both algae propagate in an identical way: a mother cell repeats several cell-divisions to make autospores with expansion of the wall, and finally, ruptures to release autospores and the cell cycle begins again. However, there are many differences in their structure and origin related to their chloroplasts as described by Hoek *et al.* [1995]. It is generally accepted that *Glaucocystis* has more primitive features and is ranked in Glaucophyta, between Cyanophyta and Chlorophyta.

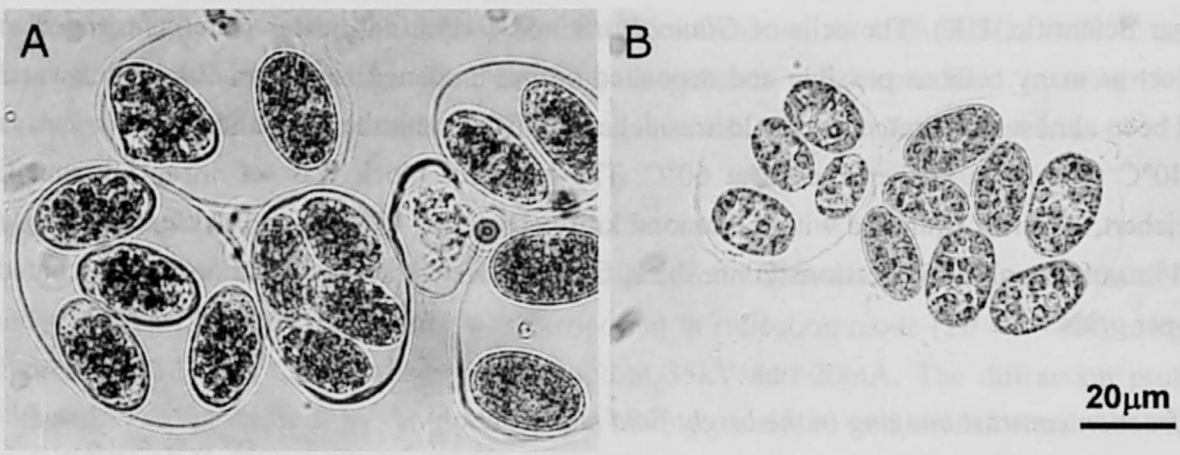

Figure 4-1. Micrographs of cells of *Glaucocystis* (A) and *Oocystis* (B). In both algae, 4~8 daughter cells are encapsulated within the mother cell wall.

High resolution CP/MAS ^{13}C-NMR spectra were obtained from fully hydrated cellulose crystallites from both specimens (Figure 4-2A). In general, the ^{13}C-NMR spectra of native cellulose, a composite of I_α and I_β allomorphs, displays triplets at C1, C4 and C6 signals depending on the ratio of each phase [Atalla & VanderHart 1984]. However, the I_α ratio was so high that the typical C1 triplet appeared almost as a single peak. To avoid confusion of surface and non-crystalline contributions to the spectrum, C4 signals were used for line shape analysis to measure the fractional ratio (f_α) of the I_α allomorph. Surprisingly, the f_α values for both algae were much larger than those reported, 0.88 for *Glaucocystis* and 0.83 for *Oocystis* (Figure 4-2B). They were much richer in I_α than typical I_α-rich specimens such as *Valonia* (0.64) [Yamamoto & Horii 1993], bacterial (0.65) [Atalla & VanderHart 1984] celluloses. In contrast to the almost pure I_β cellulose in nature, tunicate cellulose, *Glaucocystis* cellulose is regarded as an equivalently pure I_α cellulose. FT-IR spectra also supported the above findings (Figure 4-3). Values of f_α^{IR} estimated from the ratio between absorbances at 710 and 750cm^{-1} are listed in Table 4-1. *Glaucocystis* and *Oocystis* celluloses showed larger f_α^{IR} values than *Cladophora* that is even richer in I_α than *Valonia* [Chapter 1, Imai & Sugiyama 1998]. The values were less quantitative and thus gave lower estimates in comparison to the NMR results. The relative order, however, was reproducible.

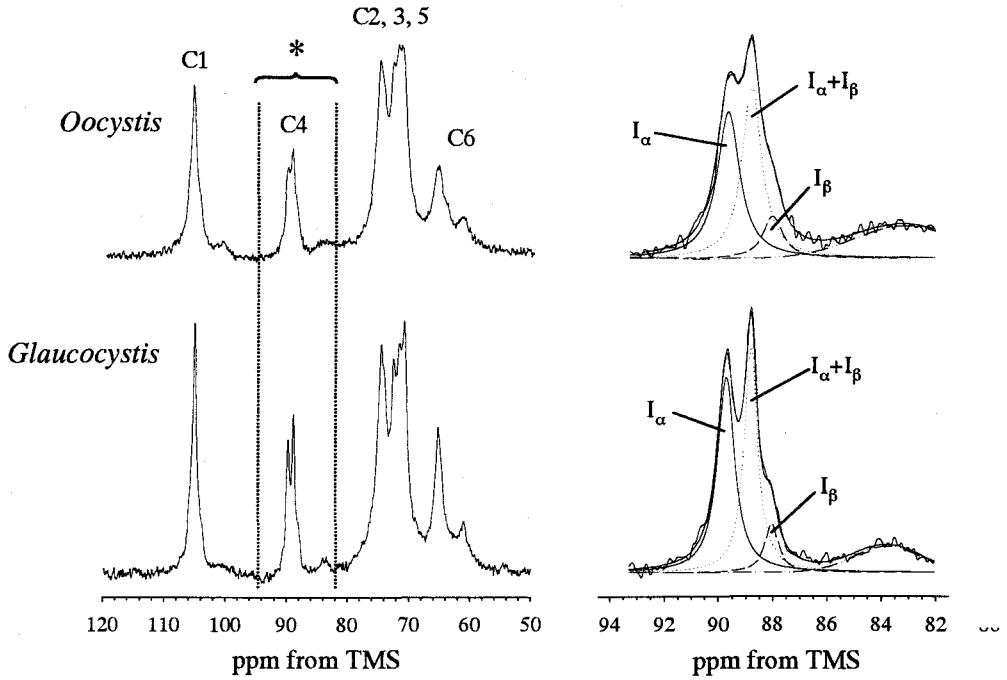

Figure 4-2. Whole spectra of ^{13}C-NMR of *Glaucocystis* and *Oocystis* cellulose (A). Enlargement of C4 region in the original spectra together with deconvoluted peaks after line-shape analysis using Lorentzian function (B). In both specimens, the peak from I_α was quite high, while that from I_β was only a trace.

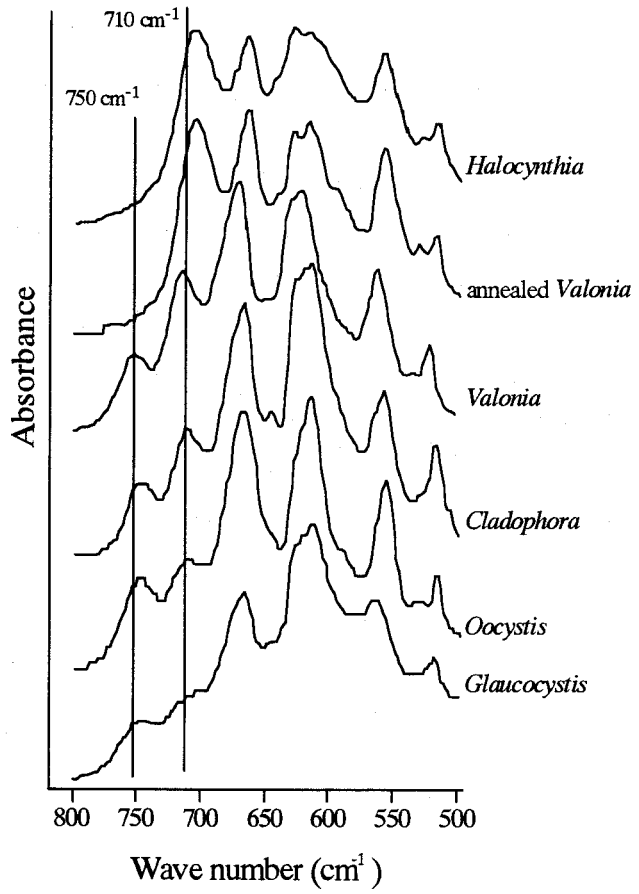

Figure 4-3.
IR spectra in the range of 800-500cm^{-1} from various specimens. Absorbance at 750cm^{-1} specific to the I_α allomorph was larger in *Glaucocystis* and *Oocystis* celluloses than in *Valonia*.

Table 4-1. I_α-fractions estimated from NMR and FT-IR measurements

Sample	I_α-fraction		
	^{13}C NMR	FT-IR*1	(SE*2)
Halocynthia	0*3-10*4	0	
Annealed *Valonia*	0.12*5	0.20	(0.04)
Valonia	0.64*5	0.64*1	(0.03)
Cladophora	0.65*6	0.76	(0.01)
Oocystis	0.83	0.80	(0.01)
Glaucocystis	0.88	0.81	(0.01)

*1: Normalized by NMR data obtained from *Valonia*[*5]. *2: Standard error ($n \geq 8$).
*3: Belton *et al.* [1989]. *4: Larrson *et al.* [1995]. *5: *V. macrophysa*, Yamamoto & Horii [1993].
*6: Horii *et al.* [1997].

Figure 4-4 shows X-ray diffractometry curves in reflection mode. The d-spacings measured from three equatorial reflections are listed in Table 4-2. I_α nature of *Glaucocystis*

and *Oocystis* celluloses was again supported by discriminant analysis [Wada *et al.* 1995] using these d-spacings.

Another important feature is the ratio of diffraction intensity, which indicates how the microfibrils are oriented with respect to the cell wall surface. More precisely, one can estimate the preferential orientation of the crystallographic plane within a microfibril with respect to the cell wall surface. For instance, the 0.61-nm lattice plane $(100)_t$ of *Valonia* cellulose (on the top) is known to lie parallel to the cell wall surface. Accordingly, these lattice planes are close to the Bragg condition when diffractometry is carried out on pressed cell walls in reflection mode. Such geometry is responsible for the strong $(100)_t$ diffraction peak.

In both *Oocystis* (in the middle) and *Glaucocystis* (in the bottom) specimens, the peak of 0.39-nm lattice planes $(110)_t$ with respect to the other two peaks was intense in comparison to *Valonia,* but this was probably due to the differences in cell size because smaller cell size would result in a higher ratio of folded edges to flat surfaces. Folded edges provide better geometrical condition for $(110)_t$ planes to satisfy the Bragg condition.

The other peaks of 0.61-nm $(100)_t$ and 0.53-nm $(010)_t$ lattice planes are quite different between *Oocystis* and *Glaucocystis.* It is clear that *Oocystis* has the same orientation-type as *Valonia,* but *Glaucocystis* seems to have a different type. Although it is difficult to conclude only from this profiles, the 0.53-nm lattice planes $(010)_t$ seem to lie more preferentially to the cell surface than 0.61-nm lattice planes $(100)_t$. Such unique orientation behavior in *Glaucocystis* becomes clear at the microscopic level as shown later.

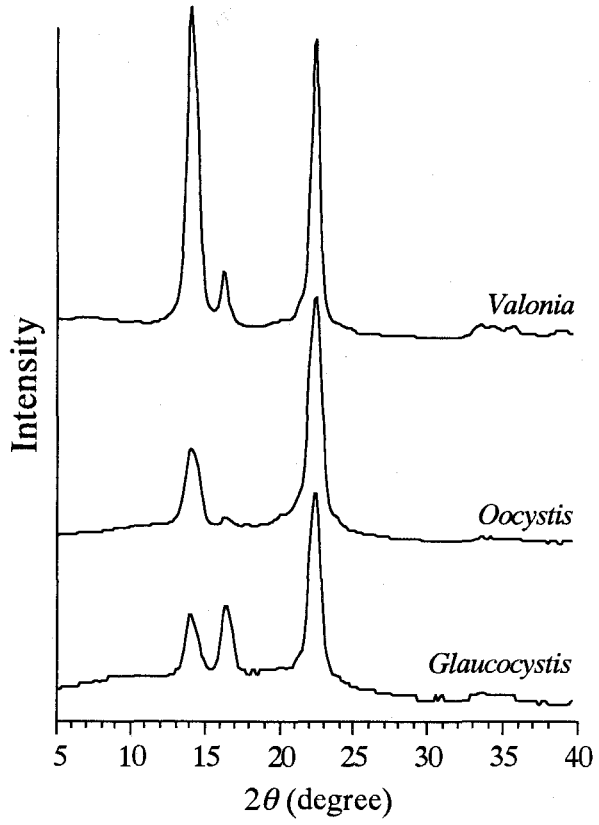

Figure 4-4.
X-ray diffractometry curves in 2θ range from 5° to 40°. Three main equatorial reflections were observed centered at 14.6°, 16.4° and 22.8°, indexed as $(100)_t$, $(010)_t$ and $(110)_t$ by the triclinic unit cell, respectively. See text for the relative changes in intensity.

Table 4-2. Calculated d-spacings from X-ray diffractometry

Sample	d_{100} (nm)	d_{010}(nm)	d_{110}(nm)
Valonia	0.615	0.534	0.393
Oocystis	0.620	0.533	0.394
Glaucocystis	0.618	0.530	0.393

Typical diffraction contrast images from ultrathin cross-sections of *Glaucocystis* and *Oocystis* cell walls are shown in Figure 4-5. A single lamella includes multiple arrays of microfibrils in the former but only one single row in the latter as previously reported [Brown & Montezinos 1976, Willison & Brown 1978a, Willison & Brown 1978b]. The cross-sectional shape was nearly square or rectangular in both samples, similar to *Valonia* cellulose although they were only half the size with an average of 10nm. The crystal edge seemed to be oriented rather randomly with respect to the lamella surface in *Glaucocystis,* while it seemed more regular in *Oocystis.*

Isolated thin cell wall fragments consisting of several lamellae were investigated to further verify the orientation of cellulose microfibrils by electron diffraction. A criss-crossing poly-lamellated structure [Robinson & Preston 1971, Brown & Montezinos 1976, Willison & Brown 1978a, Willison & Brown 1978b] was observed in both samples (Figure 4-5C). In the electron diffraction patterns from the corresponding poly-lamellated area, the difference between *Glaucocystis* and *Oocystis* celluloses was obvious: strongest reflection of $(100)_t$ in the former, nearly sole $(010)_t$ reflection in the latter (Figure 4-5D & 4-5E, respectively). In the case of electron diffraction, Bragg reflection occurs when the incident electron beam is nearly parallel to the lattice plane. Therefore, in theory the lattice planes parallel to the plane of observation (lamellae surface, Figure 4-5C) do not appear. Accordingly, it became clear that *Glaucocystis* cellulose is oriented with 0.53-nm $(010)_t$ planes parallel to the surface, while the 0.61-nm $(100)_t$ planes show this orientation in *Oocystis.* The degree of orientation was higher in *Oocystis,* but in general their microfibrils can be drawn schematically as in Figure 4-5F. To date only three algae have been reported to show the 0.53-nm type of orientation [Kreger 1957, Kim *et al.* 1996, Koyama *et al.* 1997a]. *Glaucocystis* is the first example from I_α type cellulose.

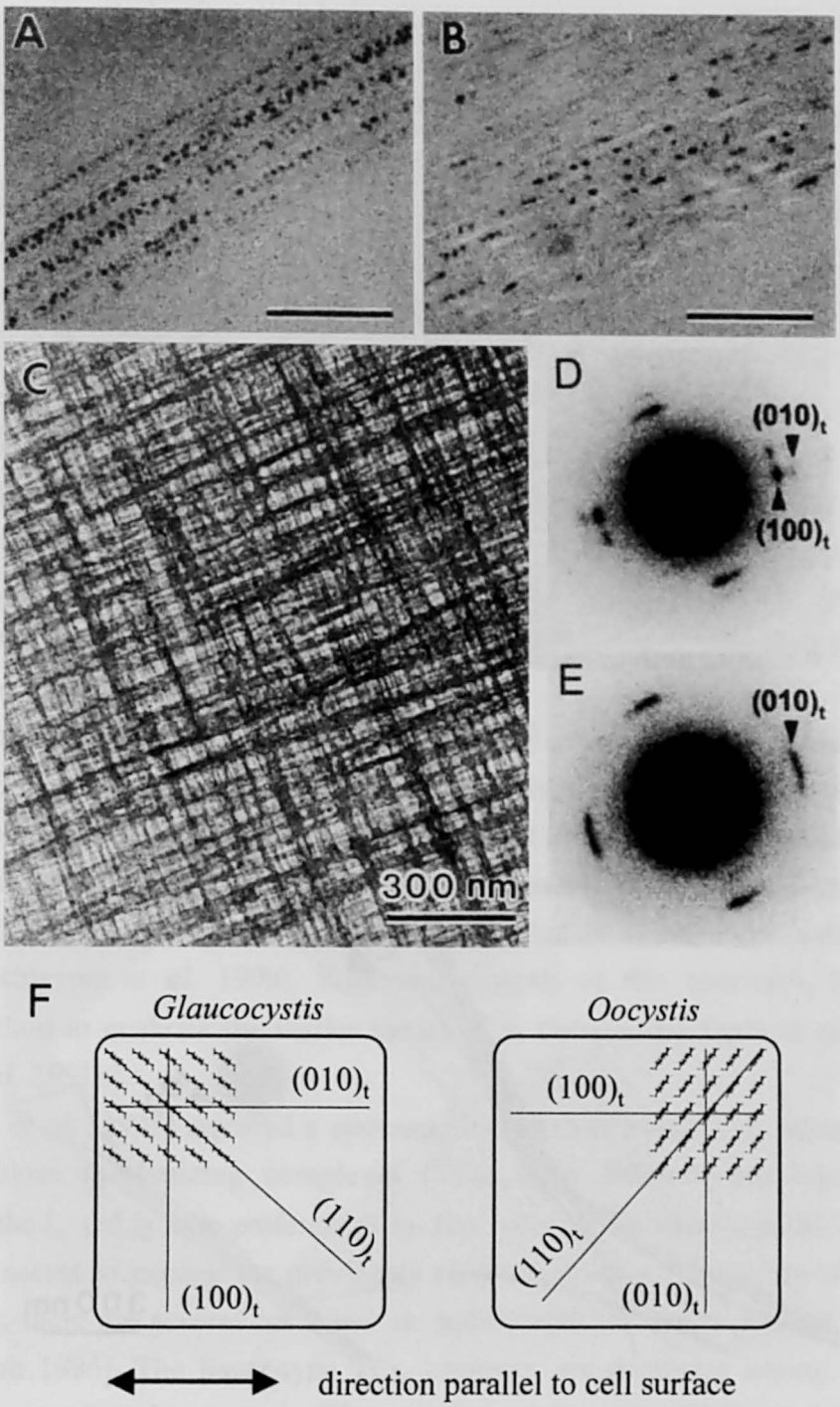

Figure 4-5 Diffraction contrast images from ultrathin cross-sections of purified cell walls from *Glaucocystis* (A) and *Oocystis* (B). Dark, square areas of contrast correspond to the cross-sectional views of cellulose microfibrils. Diffraction contrast images of purified cell wall lamellae from *Glaucocystis* (C) and the corresponding electron diffraction diagrams from lamellar-preparations of *Glaucocystis* (D) and *Oocystis* (E). The lattice plane parallel to the cell wall surface was clearly $(010)_t$ for *Glaucocystis* as opposed to $(100)_t$ for *Oocystis*. Microfibril orientation in each cell wall is schematically presented in (F).

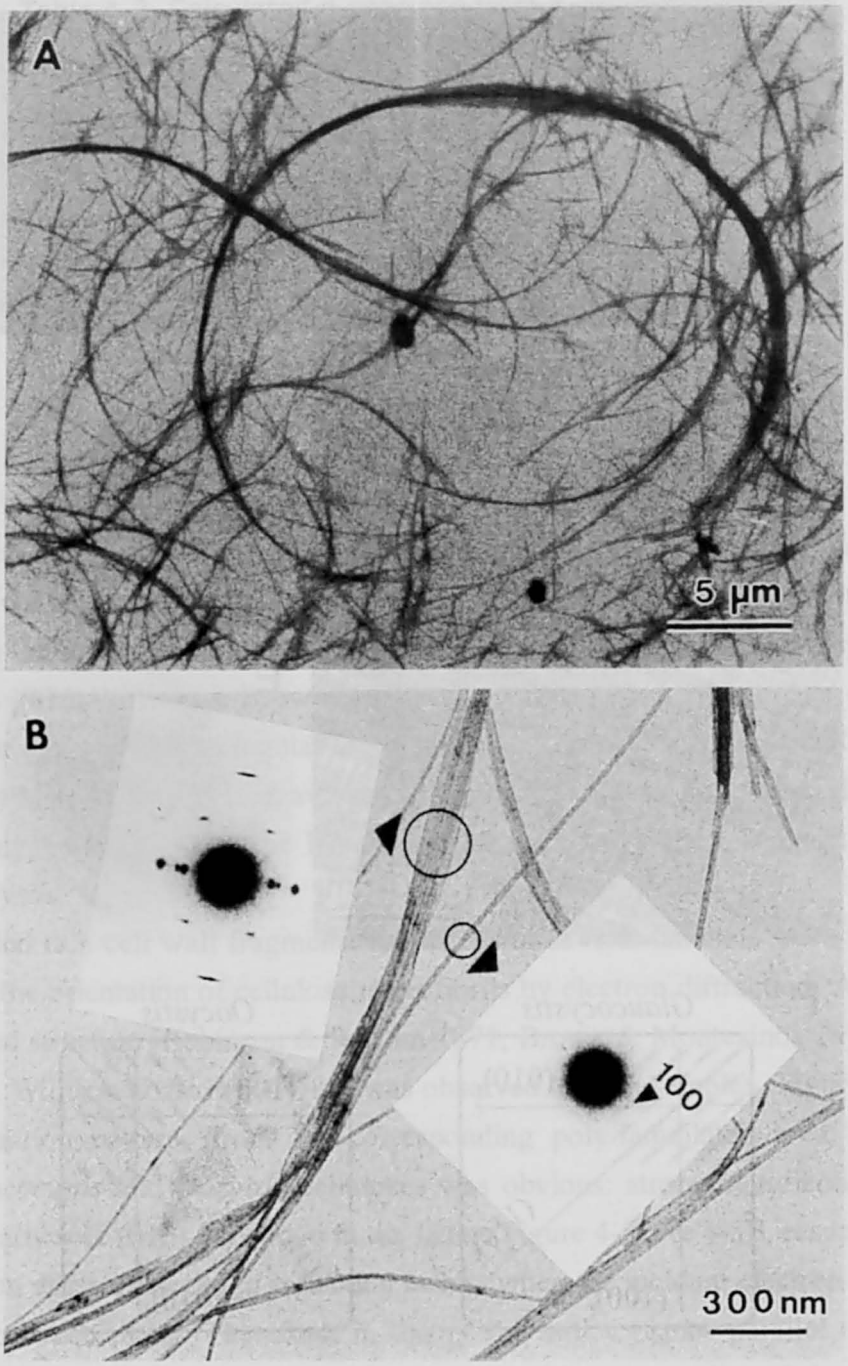

Figure 4-6 Micrographs of cellulose microcrystals disintegrated from *Glaucocystis* cell walls by acid-hydrolysis. **A**: General appearance of the hydrolysates. Arced bundles were frequently observed. **B**: Higher magnification. The width of each microcrystal was *ca.* 10 nm. Insert: typical electron diffraction diagrams taken from bundles of microcrystals (Left: fiber diagram) and one isolated microcrystal (Right: microdiffraction diagram). In the former, $(100)_t$ reflection was stronger than $(010)_t$ and a meridional spot on the 2nd layer line was completely missing. In the latter, 0.61-nm equatorial reflection clearly indicated that the microcrystal with their 0.53-nm lattice planes parallel to the supporting film.

Such preferential orientation behavior was maintained and rather emphasized after hydrolysis followed by mounting on carbon-coated microscope grids. Figure 4-6 shows the typical appearance of hydrolysates from *Glaucocystis* cellulose. Again, the diffraction diagram from the bundles seen in Figure 4-6B (insert: left) showed intense $(100)_t$ intensity, and that from isolated microcrystals (insert: right) corresponded to the typical $(100)_t$ net pattern: evidence of preferential orientation of $(010)_t$ lattice planes in this alga. In addition, a trace or a complete lack of meridional $(002)_m$ reflection (0.52nm), which is one of the characteristics of the two-chain monoclinic unit cell [Sugiyama *et al.* 1991b], agreed well with the highest I_α content in this specimen.

Finally, microfibril bundles from *Glaucocystis* often showed an arc matching the shape of daughter cell with a radius of curvature of about 15μm (Figure 4-6A). This structure remained unchanged even after mild hydrolysis sufficient to dissociate microcrystals from the cell walls of others algae including *Oocystis*. These bundles were fibrillated after ultrasonication. The radius of curvature appeared small at low magnification but in fact was too large to see at the microfibril level quantitatively.

In contrast to the almost pure I_β cellulose found in tunicates, an animal cellulose [Belton *et al.* 1989, Larsson *et al.* 1995], this study is the first demonstration of the existence of almost pure I_α cellulose. The fact that nearly 90% of the cellulose in *Glaucocystis* was the I_α allomorph as supported by ^{13}C-NMR measurement will facilitate crystallographic analysis and spectroscopy of I_α phase, which has not been studied to the same extent as I_β type celluloses [Nishiyama *et al.* 1999]. Structural analysis of this specimen, therefore, is a promising method to evaluate the earlier model of I_α deduced by electron microdiffraction [Sugiyama *et al.* 1991b].

Wada *et al.* [1995] reported a systematic study to correlate I_α/I_β allomorphism with types of cellulose synthesizing complexes (TCs) from different cellulose origins, and indicated that the I_α and I_β have preferences for linear-type and rosette-type TCs, respectively. Although this seems to explain the previously reported structural variations observed in the plant kingdom, there are several cases that do not fit with the above scheme, *e.g.* tunicates [Kimura & Itoh 1996]. The linear-type TCs, however, are dominant among those of algal origin, and they are found to exist in *Glaucocystis* and *Oocystis* [Willison & Brown 1978b, Brown & Montezinos 1976].

It is intriguing why these two cellulose crystallites contain higher amounts of I_α than other crystallites such as *Cladophora* and *Valonia* synthesized from a similar type of linear TCs. Unidirectional staggering of chains at the initial stage of crystallization is a prerequisite for the formation of I_α, and this is the most pronounced difference from I_β cellulose where the adjacent chains are staggered in a zigzag manner [Sugiyama *et al.* 1991b].

There remain many unknown factors that are involved in cellulose bio-crystallization, a proposed hypothetical working model for I_α crystallization is shown in Figure 4-7.

Assuming that cellulose microfibrils are synthesized by TCs, which move away along the surface of a spherical cell, the length of a given cellulose chain (Chain 1) or a given sheet of chains in the microfibril (arc SS') can be written as $R\theta$. The length of the chain or the sheet that runs one lattice spacing outside of Chain 1 is given by $(R+d)\theta$, where d is 0.53nm for *Glaucocystis* and 0.61nm for *Oocystis*. Accordingly the difference between two adjacent chains in a microfibril can be estimated by $d\theta$. The angle that requires the sliding of one glucose unit is then calculated by:

$$\theta = 0.52 / d \text{ (rad)}$$

where 0.52-nm is half of the fiber repeat (one glucose unit). This formula indicates that sliding of a glucose unit can occur every 50-60° independently of the cell size. However, in terms of chain length and degree of polymerization (DP), the angle corresponds to 8 to 10μm (DP=16K to 20K) for micro-algae with a radius of 10μm as observed in this chapter, while that of a *Valonia* cell with a radius of 1cm is 8.4mm (DP=17M). The smaller the cell is, the more frequently the slides of chains occur in a given length of the microfibril.

If the formation of such a curvature was the nature of cellulose microfibril, the spinning rate of each TC should not be the same. In another word, if the spinning rate of each TC was the same, only straight microfibril would result. Therefore, the shearing stress will be involved in a microfibril formation along the fibril axis as also predicted for bacterial cellulose formation in a different way [Yamamoto *et al.* 1996, Horii *et al.* 1997] or some defects or chain ends may exist in a microfibril.

Figure 4-7B shows a schematic drawing of the molecular packing, seen in a microfibril face perpendicular to the plasma membrane. Along the curvature of a microfibril, the triclinic packing arrangement in the right transforms to that in the middle with sliding of one glucose residue between adjacent molecules, and then to that in the left after another slide of the residue. Interestingly, all structures appeared as triclinic but with alternating directionality of slope of the triclinic *ab* plane. This is in good agreement with the existence of two types of triclinic unit cells rotated through 180° about the fiber axis in a *Cladophora* cellulose microfibril [Chapter1, Imai & Sugiyama 1998]. The reason why the richest I_α was found in the curved microfibril is still unknown, but the shearing stress during crystallization seems to be one of the possible factors to stimulate the I_α crystallization.

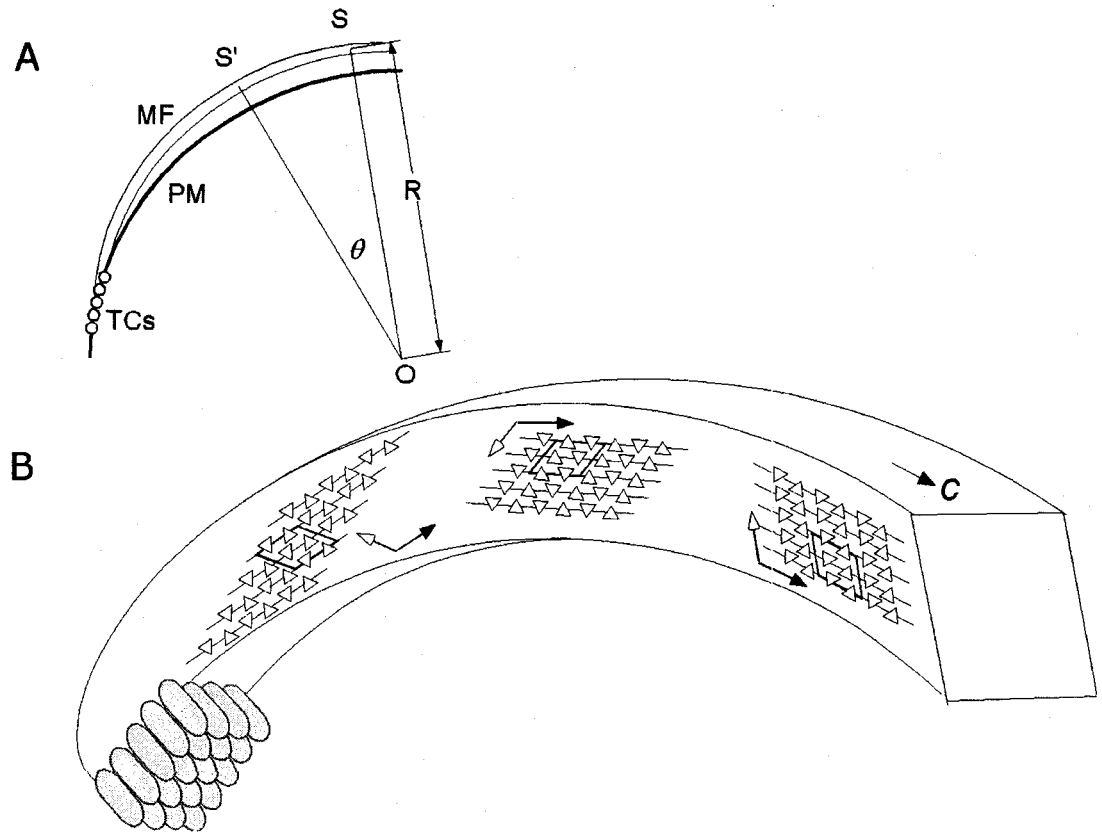

Figure 4-7. **A**: Diagrammatic representation of microfibril synthesis in a spherical cell, seen in transverse view. R indicates the radius of the curvature of the innermost microfibril. θ is the angle subtended by the arc SS' at the cell center O. MF: microfibril, TCs: terminal complexes, PM: plasma membrane. **B**: A working model of an I_α microfibril, lying with its *bc* (*Glaucocystis*) or *ac* (*Oocystis*) crystal face perpendicular to PM. Interplanar spacing between chains is 0.53nm for *Glaucocystis* and 0.61nm for *Oocystis*. ∇: glucose unit. Solid box: triclinic unit cell. Closed arrow: *c*-axis, Open arrow: directional vector of *a- or b-* axis.

In between two types of I_α domains, the chains staggering would be somehow off from the ideal triclinic packing. Apparently it is not possible to explain this structure by using a proposed monoclinic unit cell, because the staggering of adjacent chains are essentially unidirectional and similar to triclinic packing. However, somehow disordered packing can create a super-lattice, which may explain the appearance of monoclinic-type diffraction spots in the X-ray or electron diffraction diagrams. Such a model of I_β structure is different from the sheet deposition model as envisaged from high-resolution structural evidence for I_β-rich *Halocynthia* cellulose [Helbert *et al.* 1998]. The author considers that the above explanation can be only applied to partial or interfacial I_β formation in I_α-rich type cellulose.

Another interesting point is why *Glaucocystis* has a different preferential orientation. In fact, this orientation type occurs only in species such as *Spirogyra* [Kreger 1957], *Micrasterias* [Kim *et al.* 1996] and *Closterium* [Koyama *et al.* 1997a], all fresh water green algae in Zygnematales. These celluloses are I_{β}-rich [Koyama *et al.* 1997a] and are putatively synthesized by consolidated rosette-type TCs [Hogetsu 1983, Giddings *et al.* 1980, Herth 1983]. In the literatures, a number of interesting ultrastructural cytological observations have been reported for *Glaucocystis*; *i.e.* one-way movement and zoning of the TCs during cell wall formation, shield-shaped structure, transformation from flat to corrugated plasma membrane, and the behavior of microtubules [Willison & Brown 1978b], which have not been reported for other algae such as *Oocystis*. Although these lines of evidence are still too circumstantial to infer a direct relation with the structure of cellulose, they provide clues for understanding the specific formation of crystalline allomorphs as well as orientation in native algal cell walls.

4.4 Abstracts

Crystalline features of cellulose microfibrils in the cell walls of *Glaucocystis* (Glaucophyta) were studied by combined spectroscopy and diffraction techniques, and the results were compared with those of *Oocystis* (Chlorophyta). Although these algae are grouped into two different classes, by the composition of their chloroplasts for instance, their cell walls are quite similar in size and morphology. The most striking features of their cellulose crystallites are that they have the highest cellulose I_α contents reported to date. In particular, the I_α fraction of cellulose from *Glaucocystis* was found to be as high as 90% from 13 C NMR analysis. The mode of preferential orientation of cellulose crystallites in their cell walls is also interesting; equatorial 0.53-nm lattice planes were oriented parallel to the cell surface in the case of *Glaucocystis,* while the 0.62-nm planes were parallel to the *Oocystis* cell surface. Such a structural variation provides another link to the evolution of cellulose structure, biosynthesis, and its biocrystallization mechanism.

5. Molecular Directionality – A Link to Formation and Degradation of Polysaccharide Microfibrils

5.1 Introduction

Molecular directionality in a microfibril is one of the structural aspects of polysaccharide microfibril. In cellulose I, for example, all the molecular chains are packed parallel in a unit cell (parallel structure), and also in a microfibril [see General Introduction]. Such parallelism allows envisaging the mechanism of microfibril formation: polymer chains are extruded from the membrane-fixed synthases and simultaneously crystallized into a microfibril.

There are two possibilities for a parallel structure in the case of cellulose I, as explained in General Introduction (parallel-up and parallel-down). Recently, Koyama *et al.* [1997b] confirmed that cellulose I has a parallel-up structure by combining two methods – electron microdiffraction with tilting stage and selective labeling at reducing end of a microcrystal. Significantly, this structure evidenced that the polymerization of cellulose takes place at the non-reducing end of a growing chain in a bacterium, *Acetobacter aceti*. In this experiment, the selective labeling method by Kuga & Brown [1988] played a quite important role. In addition, this technique has visualized the degradation directionality of cellobiohydrolases Cel6A [Koyama *et al.* 1997b] and Cel7A in the degraded cellulose microcrystals [Chapter 3, Imai *et al.* 1998]: the unidirectional processive degradation of cellulose molecules by the cellobiohydrolases provided one-end eroded microcrystals as a result.

Thus, the selective labeling technique of molecular ends in a polysaccharide microfibril should be a very useful tool not only for structural analysis but also for analyzing biosynthesis and biodegradation, which had been studied extensively by biochemical and molecular biological approaches. In other polysaccharide microfibrils like β-chitin, the similar experiments should be available for elucidation of the corresponding issues to cellulose. Unfortunately, however, the labeling method of polysaccharide microcrystal has been reported only for cellulose I microcrystal. Therefore, the author aimed to construct the procedure for chain-end labeling of polysaccharide microfibrils. The crystalline polysaccharide specimen used here is β-chitin.

5.2 Materials and Methods

Materials

β-Chitin sample used here was isolated from *Lamellibrachia satsuma*, commonly called "tubeworm", which was harvested in the sea of Kagoshima, Japan. For purification, the tubes were boiled in 0.1N aq. NaOH for 4h and successively soaked in 0.05N HCl for 12h. The purified tubes were hydrolyzed by boiling in 2.5N HCl to prepare β-chitin microcrystals. After centrifugal washing and dialyzing against distilled water, they were brought to the labeling procedures, as described below.

Degradation of β-chitin microcrystals by chitinase A1

A part of the prepared microcrystals (1mg/ml) was incubated with 1mg/ml of chitinase A1 in phosphate buffer (pH6.0) at 37°C for a day. The enzyme was purified from a bacterium, *Bacilus circulans* WL-12 [Sugiyama *et al.* 1998]. The reaction solution was centrifuged and terminated by washing with 0.2% aq. NaOH to denature the enzyme. The degraded microcrystals were washed sequentially by several centrifugations with distilled water and subjected to the labeling procedures.

Labeling Procedure

Two procedures were considered here. One is that proposed for cellulose I microcrystal previously [Hieta *et al.* 1984, Kuga & Brown 1988], and the other was newly tried here. Both methods are based on the same strategy. The aldehyde group at reducing end is bound to a hydrazide compound with which another reagent carrying heavy metal particles subsequently interacts, allowing the reducing end to be visualized under an electron microscope. In the former procedure, the first reactant is thiosemicarbazide (TSC) and the second silver protein (SP) with subsequent enhancement by silver ammonium (SA), while in the latter, the first is biotinamidocaproyl hydrazide (biotin-X-hydrazide, BXH; Sigma Co., USA) and the second streptavidin conjugated with colloidal gold (SG). Here, the author refers the former labeling as "TSC-SP/SA" and the latter "BXH-SG". The chemical reactions carried out here are described in Scheme 5-1.

(A) TSC-SP/SA method

The recipe is fundamentally same as that reported previously for cellulose I microcrystals [Kuga & Brown 1988]. The detailed procedures are described in 3.2, Chapter 3.

(B) BXH-SG method

The interaction between biotin and streptavidin is very selective and strong, and biotin is commercially available in many forms to attach to a variety of functional groups. This is why the author expected this system for the labeling. Here, the author selected a hydrazide compound of biotin, BXH, to attach the compound to aldehyde at molecular reducing end.

Biotinylation of aldehyde at the reducing end, the first step in the BXH-SG method is carried out by "reductive amination" with cyanoborohydride [Borch *et al.* 1971, Lane 1975], by which the hydrazide part in BXH is attached to aldehyde by amide bonding (Scheme 5-1). Cyanoborohydride anion is a mild reducing agent, which reduces aldehyde or ketone very slowly at nearly neutral pH. In the range of pH, reduction of protonated imminium moiety is rapid enough, while imminium moiety formation is the optimum. Thus, aldehyde or ketone can be reductively aminated by simply reacting with an amine at pH4-10 in the presence of cyanoborohydride: the amine attacks the carbonyl α-carbon to produce imminium moiety, which is subsequently reduced into a stable amine by cyanoborohydride anion. By this reaction, biotin is fixed to the reducing end through the hydrazide in BXH.

This biotinylation step was considered more important than subsequent SG treatment. Thus, dedicated searches of biotinylation conditions were carried out for better labeling, while SG treatment was identical in all experiments. In fact, there were almost no obvious differences depending on the conditions in SG treatment.

At first, the actual procedure of the biotinylation was determined by following that in the previous study where a primary amine (2-aminopyridine) had been combined to sugars' reducing end by reductive amination [Hase *et al.* 1978]. The reaction was carried out in 1ml of absolute methanol in the presence of a little acetic acid (10-50μl), which enhances the first imminium formation, *i.e.* the reactivity of the α-carbon. β-Chitin microcrystals were suspended in the medium, and 2-4mg/ml of BXH and 0.25-1mg/ml of $NaBH_3CN$ were dissolved. The reaction was done in a sealed glass vial at variable temperatures (room temperature to 75°C) for 3-24h. The reactions with stirring and molecular sieves (3A 1/16) were also tried. Molecular sieves remove dehydrated water in the reaction system, and will suppress the reverse reaction of the imminium formation at the first step, as a result (Scheme 5-1). Thus, the biotinylation procedure was tried in variable conditions for better labeling. After thorough centrifugal washing by methanol and distilled water, blocking was carried out for 30min in tris buffered saline (TBS – 0.15M NaCl, 10mM tris, 0.02% Tween20 and 0.5% serum albumin, buffered at pH7.0) and the microcrystals were incubated for 1h at 37°C with 1ml of SG (Sigma Co., USA) solution, which was prepared by diluting the commercially available one by TBS 100-fold. The resultant microcrystals were washed twice with 50mM phosphate buffer (pH7.0) including 0.02% Tween20, and then twice with distilled water. All the reactions here were carried out in glass vials washed by nitric acid in advance.

Transmission electron microscopic observation

The labeled microcrystals were deposited on a carbon coated copper grid for TEM observation. A JEM-2000EX II operated at an accelerating voltage of 100kV was used. Bright-field images were recorded at 5,000x on Mitsubishi MEM films, which were developed by Copinal.

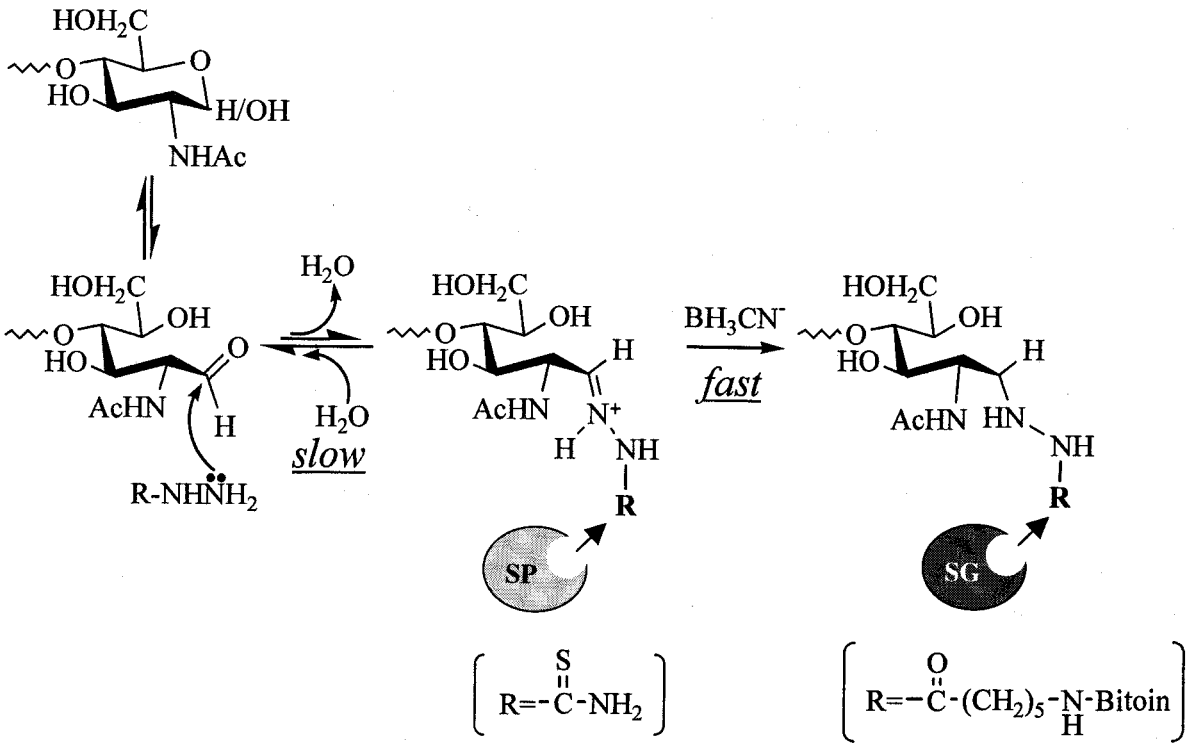

Scheme 5-1 Actions of TSC and BXH to the aldehyde at reducing end. Nucleophilic addition of hydrazide compounds to the aldehyde α-carbon occurs by attacking of the lone pair in the primary amine with dehydration to provide an imminium moiety. In the case of BXH-SG method, the imminium moiety is subsequently reduced in the presence of cyanoborohydride anion at a rapid rate (reductive amination). Generally in the reductive amination, the first step (the formation of the imminium moiety) is rate-determining. The introduced TSC and biotin at the reducing ends are visualized by SP and SG, respectively.

5.3 Results and Discussion

TSC-SP/SA labeling

The β-chitin microcrystals labeled by TSC-SP/SA method were shown in Figure 5-1. Although the labeled microcrystals were not frequently observed comparing with cellulose, this method certainly gave a label at one end (reducing end) of a β-chitin microcrystal (Figure 5-1A). The labeling seemed better without final SA enhancement (Figure 5-1B), although this was not true for cellulose. Thus, the parallel structure in β-chitin [Gardner & Blackwell 1975] seemed to be supported. Then this method was applied to the degraded microcrystals by chitinase A1. One end of the microcrystal was selectively eroded by the degradation, and the

end had been assigned to non-reducing end based on biochemical data in the previous report [Sugiyama *et al.* 1998]. Unexpectedly, however, the labels could be observed at both degraded and undegraded ends as shown in Figure 5-1C and D, implying that the labels might not be specific to reducing end. One of the possible causes might be that the acetyl amide group at C_2 position in a *N*-acetyl glucosamine residue might interact with TSC and/or SP; the labels that appeared to be fixed at an end might be actually on the side besides the end. Therefore, TSC-SP (either with or without SA enhancement) method seemed specific to the end of a β-chitin microcrystal, as far as the author has tried.

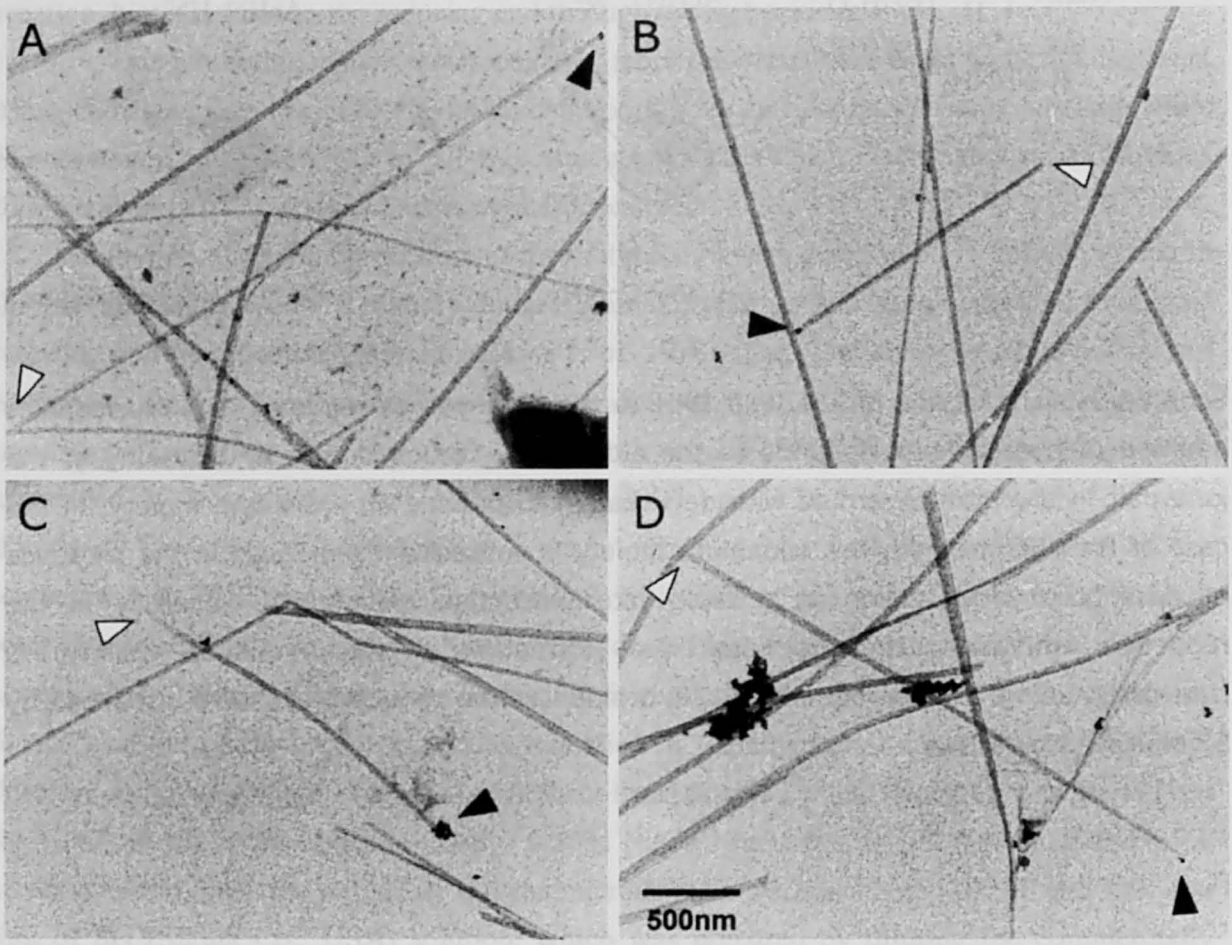

Figure 5-1. The β-chitin microcrystals labeled by TSC-SP/SA method. Black arrowheads indicate the labels at an end, and white arrowheads do the other end that is not labeled. **A**: Microcrystals labeled by the original procedure. **B**: Microcrystals labeled by TSC-SP method (without SA enhancement). In both A and B, the labels appear at one end of a microcrystal and the other end has no labels. **C, D**: The results of TSC-SP labeling of the microcrystals degraded by chitinase A1. In C, degraded end is labeled, whereas the label was seen at the eroded end in D.

BXH-SG labeling

One of the critical factors in reductive amination with BH_3CN^- is pH [Borch *et al.* 1971, Lane 1975], which is influenced by acetic acid in this case. In theory, lower pH condition is inappropriate for reductive amination, because reduction of aldehyde by BH_3CN^- becomes practically rapid at pH ~4, which spoils the aldehyde at reducing end of chitin as a consequence. On the contrary, neutral pH range may suppress reactivity of aldehyde. In addition, when molecular sieves are used for removing water in the system, it is necessary to pay an attention to that they are available in the range of pH5-11. Thus, the concentration of acetic acid was carefully controlled for finding an optimum condition. As a result, it was determined that the reaction is carried out in 1ml of absolute methanol and 50μl of acetic acid with 3A molecular sieves. This solution showed *ca.* pH4-5 (measured by pH test paper at room temperature).

The duration and temperature of biotinylation were also considered significant factors that affect the quality of labeling. A lower temperature than 75°C provided better labeling, while much lower temperature (*e.g.*, room temperature) seemed to suppress the labeling itself. Similarly, biotinylation for longer time (>24h) did not provide an improvement of labeling probability, whilst biotinylation for shorter time (<4h) did not give good labeling. When determining the duration, it is also worthy to note that reductive amination is complete for a relatively long duration, 18-36h, as described by Borch *et al.* [1971]. By trial and error, the author determined the duration and temperature as 12h and 50°C, respectively. Stirring will be one of the means to enhance a reaction. However, no effects were recognized, maybe because microcrystals swelled by stirring at higher temperature (>50°C), and the reaction rate was slow at lower temperature. As to the amount of BXH and $NaBH_3CN$, they did not influence the quality of the labeling.

In summary, the biotinylation of reducing ends in β-chitin microcrystals is preliminary established. The microcrystals are suspended in solution of 1.0ml of absolute methanol and 50μl of acetic acid, with 3mg of BXH and 0.3mg of $NaBH_3CN$ dissolved. The suspension is heated at 50°C for 12-16h in the presence of 3A molecular sieves (2 pieces). After centrifugal washing, it was brought to SG treatment as described in the experimental section. There was no case that both ends were labeled. Thus, the parallel structure in β-chitin was experimentally verified (Figure 5-2A).

The labels on the side of microcrystals were also frequently seen. Possibly, these labels indicate the molecular ends, *i.e.*, reducing ends, existing in the middle of a microcrystal, or are just a non-specific label. Otherwise, BXH might be introduced to the molecular side in chitin, *e.g.*, acetyl amide at C_2, although it will be impossible in theory. Then, as a negative control, BXH-SG labeling was applied to the microcrystals whose aldehyde at reducing end was deactivated by BH_4^- reduction. In the resultant microcrystals, almost no labels were seen (Figure 5-2B), which implies that the labels are almost specific to reducing ends. Thus, it is

concluded that the molecular ends exist also in the middle of a microcrystal.

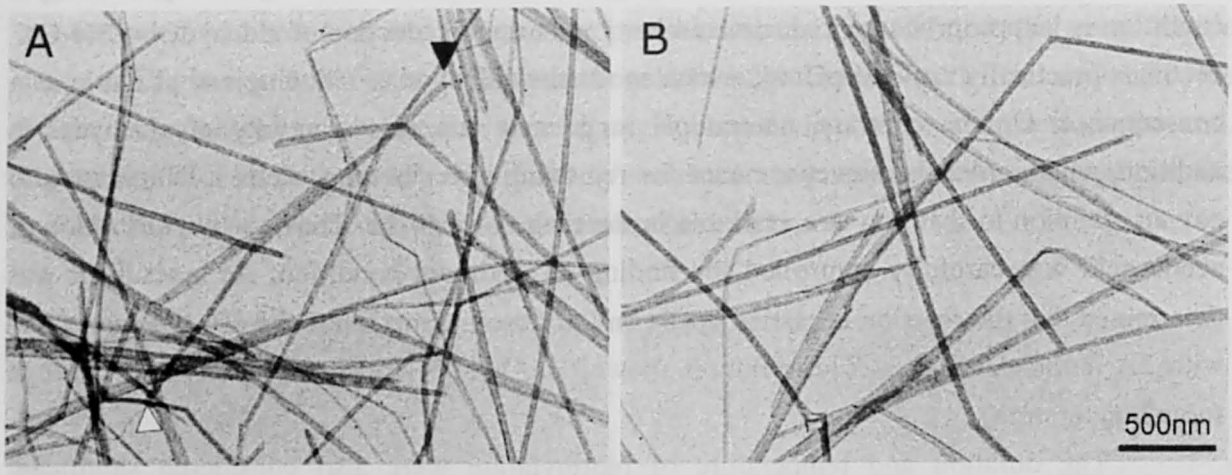

Figure 5-2. The β-chitin microcrystals labeled by BXH-SG method. (Black arrowheads: the labeled ends. White arrowheads: the other non-labeled heads) **A**: Microcrystals labeled by SG. Biotinylation was done at 50°C for 12h in 5% acetic acid in the presence of 3A molecular sieves. Some labels on the side are also observed. **B**: Labeled microcrystals by the identical conditions with A, but they were pre-reduced by BH_4^- to spoil the aldehyde at reducing end of chitin. Few labels were seen even on the side.

BXH-SG labeling of the microcrystals degraded by chitinase A1

As already visualized by Sugiyama *et al.* [1998], a β-chitin microcrystal degraded by chitinase A1 obtains one eroded end. When applying BXH-SG method to the degraded β-chitin microcrystals, labels appeared specifically at the eroded end (Figure 5-3). Since all the chains in a β-chitin microcrystal are packed parallel, it is demonstrated that chitinase A1 degrades a chitin molecule from its reducing end processively, which is contradictory to the previous biochemical study [Sugiyama *et al.* 1998]. This might be due to that the enzymatic action is altered depending on degree of polymerization of the substrate, oligomers or polymers. Furthermore, they assumed the eroded end to be non-reducing end side, and investigated electron microdiffraction diagrams in variable projections to conclude the chain polarity in the unit cell. As a result, it was demonstrated that β-chitin adopts a parallel-down structure and that polymerization of a chitin molecule in a diatom occurs at the non-reducing end of a growing chain. In the light of the novel reducing-end labeling technique described here, it has to be revised as such that β-chitin adopts a parallel-up structure proposed by Gardner & Blackwell [1975], and that a chitin molecule is polymerized at reducing end of a growing chain.

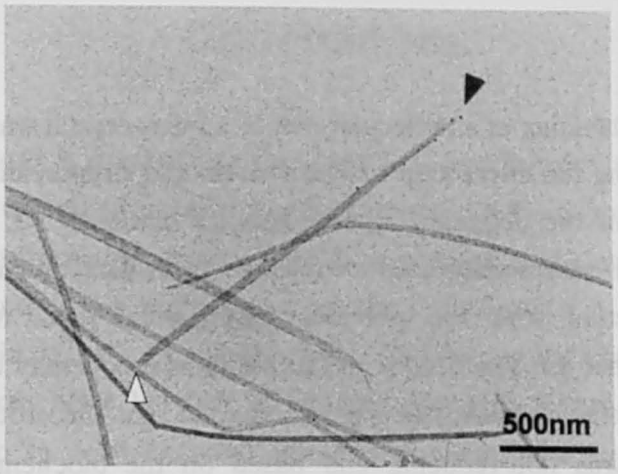

Figure 5-3. The β-chitin microcrystals degraded by chitinase A1, which is labeled subsequently by BXH-SG method (Black arrowheads: the labeled ends. White arrowheads: the other non-labeled heads). Labels are observed at the eroded end and no label at the other end, meaning that chitinase A1 degrades a chitin molecule from its reducing end to non-reducing end.

In native cellulose, the similar analysis has been already reported [Koyama *et al.* 1997b]. Using the nascent cellulose ribbon of a bacterium, *Acetobacter xylinum*, it was shown that the polymerization of cellulose takes place at the non-reducing end of a growing chain. Thus, there is a substantial difference as to the molecular directionality in biosynthesis of cellulose and chitin. As opposed to this microscopic evidence, a recent biochemical study showed that the polymerization in *A. xylinum* occurs at the reducing end of a growing chain [Han & Robyt 1998]. If this is the case, the molecular directionality in biosynthesis of both cellulose and chitin turns again to be same. In addition, based on a recent amino acid sequence analysis of glycosyltransferases [Campbell *et al.* 1997], both cellulose and chitin synthases are classified into the same family 2. This means that the catalytic machinery of these synthases is conserved (inverting type). However, there is no direct evidence that the directionality of synthesis is conserved in glycosyltransferases in the same family, as far as the author knows.

The labeling described here is specific to reducing end in theory, and should provide reliable data. Otherwise, there might be substantial experimental errors and/or misinterpretation of the crystallographic analysis in the previous papers [Koyama *et al.* 1997b, Sugiyama *et al.* 1998]. Combining all available biological and biochemical data, it should be scrutinized whether the polymerization mechanisms are different between cellulose and chitin biosynthesis, or not.

5.4 Abstracts

The selective labeling at a molecular end of a microcrystal was applied to β-chitin. A novel procedure utilizing the interaction between biotin and streptavidin has been preliminary established. Labeling of the degraded microcrystal by chitinase A1 provided labels at the degraded end in it: the enzyme degrades a molecule from its reducing end to non-reducing end. This is inconsistent with the previous biochemical data. More importantly, the disagreement implies that the conclusions in the previous report may be the reverse in terms of molecular directionality, because the report assumed that the eroded end in a degraded β-chitin microcrystal was non-reducing end based on the biochemical data. If the data obtained here is the case, β-chitin has a parallel-up structure, and polymerization of chitin occurs at the reducing end of a growing polymer chain.

Conclusions

Native cellulose is a heterogeneous crystal in the form of a submicron microfibril, which presents the structural diversity depending on the origin and comprises two allomorphs of I_α and I_β. The electron microdiffraction study revealed that the nanodomains of these two allomorphs are located in an algal cellulose microfibril with a variety of distributions depending on the origin. It is the first suggestion of lateral transition from I_α to I_β in a cellulose microfibril, which takes place between H-bonding sheets (0.39-nm lattice planes). In other words, the translation by $\pm c/4$ between the sheets is variable, resulting in the biological diversity in I_α/I_β distribution pattern. Consistently, image decomposition of HREM images revealed two domains separated by discontinuity of lattice fringes only in the $[1\bar{1}0]_t$ projection of algal I_α-rich cellulose (when seen along the 0.39-nm lattice planes), while such domains disappeared upon annealing, namely, in I_β-rich cellulose.

Morphological changes of a cellulose microfibril due to the degradation by a cellobiohydrolase Cel7A indicated that Cel7A action processively proceeds from reducing to non-reducing end, supporting the previously published biochemical data using soluble oligomers as substrates. Besides the chain polarity, cellulose microfibrils after the degradation exhibited the unidirectional erosion of the lateral side. This erosion was found to progress from the microfibril corner where pyranose ring planes of glucan chains are exposed, as if the H-bonding sheets were peeled off one by one from the microcrystal surface.

The biological origin of peculiar cellulose was found and characterized: a gray alga *Glaucocystis* obtains almost pure I_α cellulose whose 0.53-nm lattice planes lie parallel to the cell wall surface. Intriguingly, such a combination of structural features has never been reported in any sources. This provides another insight on how cellulose molecules are assembled to form a microfibril and how the mechanism of cellulose synthesis has been evolved.

A novel method that introduces biotin to reducing ends of polysaccharide molecules by reductive amination was preliminary established, by which a β-chitin microfibril with one end labeled was visualized for the first time: a parallel structure in β-chitin was experimentally verified. Labeling of the degraded microfibril by chitinase A1 demonstrated the degradation directionality by the enzyme, and also provided information on the formation of the microfibril based on the previously published crystallographic analysis. Comparing with the cellulose system, the formation and degradation behaviors of their microfibril structures were discussed.

References

Amano, Y., Shiroishi, M., Nishizawa, K., Hoshino, E. & Kanda, T. (1996) Fine substrates specificities of four exo-type cellulases produced by *Aspergillus niger*, *Trichoderma reesei*, and *Irpex lacteus* on (1→3), (1→4)-β-D-glucans and xyloglucans. *J. Biochem.* **120**, 1123-1129.

Armand, S., Drouillard, S., Schülein, S., Henrissat, B. & Driguez, H. (1997) A bifunctionalized fluorogenic tetrasaccharide as a substrate to study cellulases. *J. Biol. Chem.* **272**, 2709-2713.

Atalla, R. H. & VanderHart, D. L. (1984) Native cellulose: A composite of two distinct crystalline forms. *Science* **223**, 283-285.

Atalla, R. H., Hackney, J. M., Uhlin, I. & Thompson, N. S. (1993) Hemicelluloses as structure regulators in the aggregation of native cellulose. *Int. J. Biol. Macromol.* **15**, 109-112.

Baker, A. A., Helbert, W., Sugiyama, J. & Miles, M. J. (1997) High-resolution atomic force microscopy of native *Valonia* cellulose I microcrystals. *J. Structr. Biol.* **119**, 129-138.

Barr, B. K., Hsieh, Y.-L., Ganem, B. & Wilson, D. B. (1996) Identification of two functionally different classes of exocellulases. *Biochemistry* **35**, 586-592.

Belton, P. S., Tanner, S. F., Cartier, N. & Chanzy, H. (1989) High-resolution solid-state ^{13}C nuclear magnetic resonance spectroscopy of tunicin, an animal cellulose. *Macromolecules* **22**, 1615-1617.

Boisset, C., Armand, S., Drouillard, S., Chanzy, H., Driguez, H. & Henrissat, B. (1998) In: Carbohydrases from *Trichoderma reesei* and other microorganisms: Structure, Biochemistry, Genetics and Applications (M. Claeyssens ed.), pp. 124-132, The Royal Society of Chemistry, Cambridge.

Borch, R. F., Bernstein, M. D. & Durst, H. D. (1971) The cyanohydridoborate anion as a selective reducing agent. *J. Amer. Chem. Soc.* **93**, 2897-2904.

Bourret, A., Chanzy, H. & Lazaro R. (1972) Crystalline features of *Valonia* cellulose by electron diffraction and dark-field electron microscopy. *Biopolymers* **11**, 893-898.

Brown, R. M. Jr. & Montezinos, D. (1976) Cellulose microfibrils: Visualization of biosynthetic and orienting complexes in association with the plasma membrane. *Proc. Nat. Acad. Sci. USA* **73**, 143-147.

Campbell, J. A., Davies, G. J., Bulone, V. & Henrissat, B. (1997) A classification of nucleotide-diphospho-sugar glycosyltransferases based on amino acid sequence similarities. *Biochem. J.* **326**, 929-942.

Chanzy, H., Henrissat, B., Vuong, R. & Schulein, M. (1983) The action of 1,4-β-D-glucan cellobiohydrolase on *Valonia* cellulose microcrystals. An electron microscopic study. *FEBS Lett.* **153**, 113-117.

Chanzy, H. & Henrissat, B. (1985) Unidirectional degradation of *Valonia* cellulose microcrystals subjected to cellulase action. *FEBS Lett.* **184**, 285-288.

Claeyssens, M., van Tilbeurgh, H., Tomme, P. & Wood, T. M. (1989) Fungal cellulase systems. Comparison of the specificities of the cellobiohydrolases isolated from *Penicillium pinophilum* and *Trichoderma reesei*. *Biochem. J.* **261**, 819-825.

Cousins, S. K. & Brown, R. M. Jr. (1995) Cellulose I microfibril assembly: computational molecular mechanics energy analysis favors bonding by van der Waals forces as the initial step in crystallization. *Polymer* **36**, 3885-3888.

Davies, G. & Henrissat, B. (1995) Structures and mechanisms of glycosyl hydrolases. *Structure* **3**, 853-859.

Debzi, E. M., Chanzy, H., Sugiyama, J., Tekely, P. & Excoffier, G. (1991) The $I_\alpha \rightarrow I_\beta$ transformation of highly crystalline cellulose by annealing in various mediums. *Macromolecules* **24**, 6816-6822.

Divne, C., Ståhlberg, J., Reinikainen, T., Ruohonen, L., Pettersson, G., Knowles, J. K. C., Teeri, T. T. & Jones, T. A. (1994) The three-dimensional crystal structure of the catalytic core of cellobiohydrolase I from *Trichoderma reesei*. *Science* **265**, 524-528.

Divne, C., Ståhlberg, J., Teeri, T. T. & Jones, T. A. (1998) High-resolution crystal structures reveal hoe a cellulose chain is bound in the 50Å long tunnel of cellobiohydrolase I from *Trichoderma reesei*. *J. Mol. Biol.* **275**, 309-325.

Echlin, P. (1967) The biology of *Glaucocystis nostochinearum*. I. The morphology and fine structure. *Br. Phycol. Bull.* **3**, 225-239.

Ellis, K. C. & Warwicker, J. O. (1962) A study of the crystal structure of cellulose I. *J. Polym. Sci.* **56**, 339-357.

Fisher, D. G. & Mann, J. (1960) Crystalline modifications of cellulose. Part VI. Unit cell and molecular symmetry of cellulose I. *J. Polym. Sci.* **42**, 189-194.

French, A. D. (1978) The crystal structure of native ramie cellulose. *Carbohydr. Res.* **61**, 67-80.

Fukami, A. & Adachi, K. (1965) A new method of preparation of a self-perforated micro plastic grid and its application (I) *J. Electr. Microscopy* **14**, 112-118.

Fujiyoshi, Y., Mizusaki, T., Morikawa, K., Yamagishi, H., Aoki, Y., Kihara, H. & Harada, Y. (1991) Development of a super fluid helium stage for high-resolution microscopy. *Ultramicroscopy* **38**, 241-251.

Fujiyoshi, Y. (1998) The structural study of membrane proteins by electron crystallography. *Adv. Biophys.* **35**, 22-80.

Gaill, F., Persson, J., Sugiyama, J., Vuong, R. & Chanzy, H. (1992) The chitin system in the tubes of deep sea hydrothermal vent worms. *J. Struct. Biol.* **109**, 116-128.

Gardner, K. H. & Blackwell, J. (1974) The structure of native cellulose. *Biopolymers* **13**, 1975-2001.

Gardner, K. H. & Blackwell, J. (1975) Refinement of the structure of β-chitin. *Biopolymers* **14**, 1581-1595.

Giddings, T. H., Brower, D. L. & Staehelin, L. A. (1980) Visualization of particle complexes in the plasma membrane of *Micrasterias denticulata* associated with the formation of cellulose fibrils in primary and secondary cell wall. *J. Cell Biol.* **84**, 327-339.

Hackney, J. M., Atalla, R. H. & VanderHart, D. L. (1994) Modification of crystallinity and crystalline structure of *Acetobacter xylinum* cellulose in the presence of water-soluble β-1,4-linked polysaccharides: ^{13}C-NMR evidence. *Int. J. Biol. Macromol.* **16**, 215-218.

Han, N. S. & Robyt, J. F. (1998) The mechanism of *Acetobacter xylinum* cellulose biosynthesis: direction of chain elongation and the role of lipid pyrophosphate intermediated in the cell membrane. *Carbohydr. Res.* **313**, 125-133.

Hase, S., Ikenaka, T. & Matsushima, Y. (1978) Structure analysis of oligosaccharides by tagging of the reducing end sugars with a fluorescent compound. *Biochem. Biophys. Res. Comm.* **85**, 257-263.

Hayashi, N., Sugiyama, J., Okano, T. & Ishihara, M. (1997) Selective degradation of the cellulose I_α component in *Cladophora* cellulose with *Trichoderma viride* cellulase. *Carbohydr. Res.* **305**, 109-116.

Helbert, W. & Sugiyama, J. (1998) High-resolution electron microscopy on cellulose II and α-chitin single crystals. *Cellulose* **5**, 113-122.

Helbert, W., Nishiyama, Y., Okano, T. & Sugiyama, J. (1998) Molecular imaging of *Halocynthia papillosa* cellulose. *J. Struc. Biol.* **124**, 42-50.

Henrissat, B., Teeri, T. T. & Warren, R. A. J. (1998) A scheme for designating enzymes that hydrolyse the polysaccharides in the cell wall of plants. *FEBS Lett.* **425**, 352-354.

Herth, W. (1983) Arrays of plasma-membrane "rosette" involved in cellulose microfibril formation of *Spirogyra*. *Planta* **159**, 347-356.

Hieta, K., Kuga, S. & Usuda, M. (1984) Electron staining of reducing ends evidences a parallel-chain structure in *Valonia* cellulose. *Biopolymers* **23**, 1807-1810.

Hoek, C. Van Den, Manw, D. G. & Jahns, H. M. (1995) Algae. Cambridge University Press, Cambridge, 45-47 pp.

Hogetsu, T. (1983) Distribution and local activity of particle complexes synthesizing cellulose microfibrils in the plasma membrane of *Closterium acerosum* (Schrank) Ehrenberg. *Plant Cell Physiol.* **24**, 777-782.

Honjo, G. & Watanabe, M. (1958) Examination of cellulose fibre by the low-temperature specimen method of electron diffraction and electron microscopy. *Nature* **181**, 326-328.

Horii, F., Yamamoto, H., Kitamaru, R., Tanahashi, M. & Higuchi, T. (1987) Transformation of native cellulose crystals induced by saturated steam at high temperatures. *Macromolecules* **20**, 2946-2949.

Horii, F., Yamamoto, H. & Hirai, A. (1997) Microstructural analysis of microfibrils of bacterial cellulose. *Macromol. Symp.* **120**, 197-205.

Hÿtch, M. J. & Gandais, M. (1995) Quantitative criteria for the detection and characterization of nanocrystals from high-resolution electron microscopy images. *Phil. Mag. A* **72**, 619-634.

Hÿtch, M. J. (1997) Analysis of variations in structure from high resolution electron microscope images by combining real space and Fourier space information. *Microsc. Microanal. Microstruct.* **8**, 41-57.

Hÿtch, M. J. & Potez, L. (1997) Geometric phase analysis of high-resolution electron microscopy images of antiphase domains: example Cu_3Au. *Phil. Mag. A* **76**, 1119-1138.

Hÿtch, M. J., Snoeck, E. & Kilaas, R. (1998) Quantitative measurement of displacement and strain fields from HREM micrographs. *Ultramicroscopy* **74**, 131-146.

Imai, T., Boisset, C., Samejima, M., Igarashi, K. & Sugiyama, J. (1998) Unidirectional processive action of cellobiohydrolase Cel7A on *Valonia* cellulose microcrystals. *FEBS Lett.* **432**, 113-116.

Imai, T. & Sugiyama, J. (1998) Nanodomain of I_α and I_β cellulose in algal microfibril. *Macromolecules* **31**, 6275-6279.

Itoh, T. & Brown, R. M. Jr. (1984) The assembly of cellulose microfibrils in *Valonia macrophysa* Kutz. *Planta* **160**, 372-381.

Jakubowski, U., Baumeister, W., Glaeser, R. M. (1989) Evaporated carbon stabilizes thin, frozen-hydrated specimens. *Ultramicroscopy* **31**, 351-356.

Kantz, T. & Bold, H. C. (1969) Phycological studies. IX. Morphological and taxonomic investigations of *Nostoc* and *Anabaene* in culture. University of Texas Publication no. 6924. University of Texas Press, Austin, Texas. 67 pp.

Kim, N. H., Herth, W., Vuong, R. & Chanzy, H. (1996) The cellulose system in the cell wall of *Micrasterias*. *J. Struc. Biol.* **117**, 195-203.

Kimura, S. & Itoh, T. (1996) New Cellulose synthesizing complex (= terminal complexes) involved in animal cellulose biosynthesis in the tunicate, *Metandrocarpa uedai*. *Protoplasma* **194**, 151-163.

Koyama, M., Sugiyama, J. & Itoh, T. (1997a) Systematic survey on crystalline features of algal celluloses. *Cellulose* **4**, 1-14.

Koyama, M., Helbert, W., Imai, T., Sugiyama, J. & Henrissat, B. (1997b) Parallel-up structure evidences the molecular directionality during biosynthesis of bacterial cellulose. *Proc. Natl. Acad. Sci. USA* **94**, 9091-9095.

Kreger, D. R. (1957) New crystallite orientations of cellulose I in *Spirogyra* cell wall. *Nature* **180**, 914-915.

Kudlicka, K., Brown, R. M. Jr., Likun, L., Lee, J. H. & Kuga, S. (1995) β-Glucan synthesis in the cotton fiber. IV. In vitro assembly of the cellulose I allomorph. *Plant Physiol.* **107**, 111-123.

Kuga, S. & Brown, R. M. Jr. (1988) Silver labeling of the reducing ends of bacterial cellulose. *Carbohydr. Res.* **180**, 345-350.

Lane, C. F. (1975) Sodium Cyanoborohydride – A highly selective reducing agent for organic functional groups. *Synthesis* **1975**, 135-146.

Larsson, T., Westermark, U. & Iverson, T. (1995) Determination of the cellulose I_α allomorph in a tunicate cellulose by CP/MAS ^{13}C NMR spectroscopy. *Carbohydr. Res.* **278**, 339-343.

Lee, J. H., Brown, R. M. Jr., Kuga, S., Shoda, S. & Kobayashi, S. (1994) Assembly of synthetic cellulose I. *Proc. Natl. Acad. Sci. USA* **91**, 7425-7429.

Marrinan, H. J. & Mann, J. (1956) Infrared spectra of the crystalline modifications of cellulose. *J. Polym. Sci.* **21**, 301-311.

Mann, J. & Marrinan, H. J. (1956) Crystalline modifications of cellulose. Part II. A study with plane-polarized infrared radiation. *J. Polym. Sci.* **32**, 357-370.

Meyer, K. H. & Misch, L. (1937) Positions de atomes dans le nouveau modèle spatial de la cellulose. *Helv. Chim. Acta* **20**, 232-244.

Mori, N., Oikawa, T., Katoh, T., Miyahara, J. & Harada, Y. (1988) Application of imaging plate to TEM image recording. *Ultramicroscopy* **25**, 195-201.

Nishiyama, Y., Okano, T., Langan, P. & Chanzy, H. (1999) High resolution neutron fiber diffraction data on hydrogenated and deuterated cellulose, *Int. J. Biol. Macromol.* **26**, 279-283.

Provasoli, L., McLanghlin, J. J. A. & Droop, M. R. (1957) The development of artificial media for marine algae. *Arch. Mikrobiol.* **25**, 392-428.

Putaux, J.-L., Helbert, W., Hÿtch, M. J. & Chanzy, H. (1995) H.R.E.M. imaging with real-space averaging of V amylose crystals. Proceedings of the Trinocular Congress of Electron Microscopy, Lausanne, Switzerland, 51.

Revol, J.-F. (1982) On the cross-sectional shape of cellulose crystallites in *Valonia ventricosa*. *Carbohydr. Polym.* **2**, 123-134.

Revol, J.-F. & Goring, D. A. I. (1983) Directionality of the fiber c-axis of cellulose crystallites in microfibrils of *Valonia ventricosa*, *Polymer* **24**, 1547-1550.

Robinson D. G. & Preston R. D. (1971) Studies on the fine structure of *Glaucocystis nostochinearum* Itzigs. II. Membrane morphology and taxonomy. *Br. phycol. J.* **6**, 113-128.

Rouvinen, J., Bergfors, T., Teeri, T. T., Knowles, J. K. C. & Jones, T. A. (1990) Three-dimensional structure of cellobiohydrolase II from *Trichoderma reesei*. *Science* **249**, 380-386.

Saito, Y., Okano, T., Chanzy, H. & Sugiyama, J. (1995) Structural study of α chitin from the grasping spines of the arrow worm (*Sagitta* spp.) *J. Struct. Biol.* **114**, 218-228.

Samejima, M., Sugiyama, J., Igarashi, K. & Eriksson, K.-E. L. (1998) Enzymatic hydrolysis of bacterial cellulose. *Carbohydr. Res.* **305**, 281-288.

Sarko, A. & Muggli, R. (1974) Packing analysis of carbohydrates and polysaccharide. III. *Valonia* cellulose and cellulose II. *Macromolecules* **7**, 486-494.

Sassi, J.-F. (1995) Étude ultrastructurale de l'acétylation de la cellulose application à la préparation de nanocomposites. Ph.D. Thesis, Université Joseph Fourier Grenoble I, p.57-73.

Sassi, J.-F. & Chanzy, H. (1995) Ultrastructural aspects of the acetylation of cellulose. *Cellulose*, **2**, 111-127.

Saxton, W. O., Pitt, T. J. & Horner, M. (1979) Digital image processing: The Semper system. *Ultramicroscopy* **4**, 343.

Srisodsuk, M., Kleman-Leyer, K., Keränen, S., Kirk, T. K. & Teeri, T. T. (1998) Modes of action on cotton and bacterial cellulose of a homologous endoglucanase-exoglucanase pair from *Trichoderma reesei*. *Eur. J. Biochem.* **251**, 885-892.

Stewart, M. (1988) Introduction to the computer image processing of electron micrographs of two-dimensionally ordered biological structures. *J. Elec. Microscopy Tech.* **9**, 301-324.

Sugiyama, J., Harada, H., Fujiyoshi, Y. & Uyeda, N. (1984) High resolution observations of cellulose microfibrils. *Mokuzai Gakkaishi* **30**, 98-99.

Sugiyama, J., Harada, H., Fujiyoshi, Y. & Uyeda, N. (1985a) Observations of cellulose microfibrils in *Valonia macrophysa* by high resolution electron microscopy. *Mokuzai Gakkaishi* **31**, 61-67.

Sugiyama, J., Harada, H., Fujiyoshi, Y. & Uyeda, N. (1985b) Lattice images from ultrathin sections of cellulose microfibrils in the cell wall of *Valonia macrophysa* Kutz. *Planta* **166**, 161-168.

Sugiyama, J., Okano, T., Yamamoto, H. & Horii, F. (1990) Transformation of *Valonia* cellulose crystals by an alkaline hydrothermal treatment. *Macromolecules* **23**, 3196-3198.

Sugiyama, J., Persson, J. & Chanzy, H. (1991a) Combined infrared and electron diffraction study of the polymorphism of native celluloses. *Macromolecules* **24**, 2461-2466.

Sugiyama, J., Vuong, R. & Chanzy, H. (1991b) Electron diffraction study on the two crystalline phases occurring in native cellulose from an algal cell wall. *Macromolecules* **24**, 4168-4175.

Sugiyama, J., Boisset, C., Hashimoto, M. & Watanabe, T. (1998) Molecular directionality of β-chitin biosynthesis. *J. Mol. Biol.* **286**, 247-255.

Teeri, T. T. (1997) Crystalline cellulose degradation: new insight into the function of cellobiohydrolases. *Trends Biotechnol.* **15**, 160-167.

VanderHart, D. L. & Atalla, R. H. (1984) Studies of microstructure in native celluloses using the solid-state ^{13}C-NMR. *Macromolecules* **17**, 1465-1472.

Veršanská, M. & Biely, P. (1992) The cellobiohydrolase I from *Trichoderma reesei* QM9414: action on cello-oligosaccharides. *Carbohydr. Res.* **227**, 19-27.

Wada, M., Sugiyama, J. & Okano, T. (1995) The crystalline phase (I_α/I_β) system of native celluloses in relation to plant phylogenesis. *Mokuzai Gakkaishi* **41**, 186-192.

Willison, J. H. M. & Brown, R. M. Jr. (1978a) A model for the pattern of deposition of microfibrils in the cell wall of *Glaucocystis*. *Planta* **141**, 51-58.

Willison, J. H. M. & Brown, R. M. Jr. (1978b) Cell wall structure and deposition in *Glaucocystis*. *J. Cell Biol.* **77**, 103-119.

Woodcock, C. & Sarko, A. (1980) Packing analysis of carbohydrates and polysaccharide. 11. Molecular and crystal structure of native ramie cellulose. *Macromolecules* **13**, 1183-1187.

Yamamoto, H., Horii, F. & Odani, H. (1989) Structural changes of native cellulose crystals induced by annealing in aqueous alkaline and acidic solution at high temperature. *Macromolecules* **22**, 4130-4132.

Yamamoto, H. & Horii, F. (1993) CP/MAS ^{13}C NMR analysis of the crystal transformation induced for *Valonia* cellulose by annealing at the high temperatures. *Macromolecules* **26**, 1313-1317.

Yamamoto, H., Horii, F. & Hirai, A. (1996) *In situ* crystallization of bacterial cellulose. II. Influences of different polymeric additives on the formation of celluloses I_α and I_β at the early stage of incubation. *Cellulose* **3**, 229-242.

Acknowledgement

The author wishes to express sincere thanks to Prof. Takao Itoh in Wood Research Institute, Kyoto University for his kind guidance during the doctoral course. The author also thanks Profs. Jun-ichi Azuma and Minoru Fujita in Graduate School of Agriculture, Kyoto University for their critical reading of the manuscript and valuable suggestions. The author wishes to express special thanks to my supervisor, Dr. Junji Sugiyama for his extensive effort to organize my works and his encouragement for me.

The experiment with an analytical electron microscope JEM-2010 equipped with imaging plates is owing to Dr. Tetsuo Oikawa in JEOL Co., Japan. The author thank Prof. Takashi Kobayashi, Prof. Seiji Isobe and Dr. Tetsuo Ogawa in the Institute for Chemical Research, Kyoto University for allowing to use an electron microscope JEM-4000SFX equipped with a super fluid helium stage.

Regarding the geometric phase analysis, the author is indebted to Dr. Jean-Luc Putaux, a visiting scientist from CERMAV-CNRS (Centre de Recherches sur les Macromolécules Végétales – Centre National de la Recherche Scientifique, Grenoble, France), in the framework of the Joint Research Program between JSPS (Japan Society for the Promotion of Science)-CNRS (1997-1998, coordinated by Drs. Junji Sugiyama and Henri Chanzy). The author appreciates his enthusiasm and encouragement on this topic and kindest hospitality during my counter visit in his laboratory in 1997 for a month (July – August, 97). The author acknowledges the critical discussion with Dr. Henri Chanzy during the stay. The author is also grateful to Dr. Martin Hÿtch in Centre d'Etude de Chimie Métallurgique – CNRS, Vitry, France, for his practical advises about the analysis.

The experiment with regard to Cel7A is owing to many collaborators: Drs. Masahiro Samejima and Kiyohiko Igarashi in the Graduate School of Agricultural and Life Science, the University of Tokyo, for their gift of purified Cel7A enzyme and valuable discussion about the enzyme action; Dr. Claire Boisset who came from CERMAV-CNRS by the Joint Research Program between JSPS and CNRS and collaborated in W.R.I. with the author.

Solid-state CP/MAS ^{13}C-NMR measurement is owing to Prof. Fumitaka Horii in the Institute for Chemical Research, Kyoto University.

The author appreciates a gift of chitinase A1 from Prof. Takeshi Watanabe in Faculty of Agriculture, Niigata University. The author is grateful to Dr. Hiroshi Kamitakahara in Graduate School of Agriculture, Kyoto University for useful discussion about the reaction scheme. The author is indebted to the Research Fellowship of the JSPS for Young Scientists. Finally, the author acknowledges everyone in Cell Structure and Function Laboratory in W.R.I. for their helping me finish the thesis.